

**Van der Waals Heterostructures
based on Two-dimensional
Ferroelectric and Ferromagnetic Layers**

Shihong Xie

**Thesis submitted to the University of Nottingham
for the degree of Doctor of Philosophy
August 2023**

Abstract

Two-dimensional (2D) van der Waals (vdW) crystals provide a platform for studies of novel phenomena and promising applications beyond traditional systems. This PhD thesis focuses on vertical 2D vdW heterostructures, including ferroelectric semiconductor junctions (FSJs), *p-n* junction diodes, and magnetic tunnel junctions (MTJs). These have potential for non-volatile memories, ultraviolet (UV) photosensing and low-power electronics.

The ferroelectric polarization of the vdW semiconductor α -In₂Se₃ in graphene/ α -In₂Se₃/graphene FSJs was switched by the bias voltage, thus producing memristive effects in the transport characteristics. These can be modified by light due to screening of the polarization by photocreated carriers. The FSJs demonstrated a high photoresponsivity (up to $\sim 10^6$ A/W) and a relatively fast modulation (down to ~ 0.2 ms) of the photocurrent.

The graphene/*p*-GaSe/*n*-In₂Se₃/graphene heterostructures were used to investigate novel mechanisms for the detection of UV light. The *p*-GaSe/*n*-In₂Se₃ type-II band alignment and the electric field at the vdW interfaces were found to be beneficial to suppress carrier recombination and enhance the UV-photoresponse.

Finally, the Fe₃GaTe₂/WSe₂/Fe₃GaTe₂ MTJs exhibited an ideal tunnelling behaviour with a tunnel magnetoresistance (TMR) signal as large as 85 % at room temperature, breaking through the bottleneck of previous vdW MTJs that worked only at low temperatures ($T < 300$ K).

The findings of this work offer opportunities for further developments, including the optimization of device structures and their studies towards enhanced functionalities beyond the current state of the art.

Acknowledgements

First and foremost, I would like to express my sincerest gratitude to my supervisor, Prof. Amalia Patanè, for the continuous support and encouragement throughout the course of my PhD. The completion of this work is down to her constant assistance and motivation. Prof. Amalia Patanè is accountable, considerate and knowledgeable. She has a sharp intuition for physics, holds a rigorous attitude towards academia, works diligently, and carries herself humbly. I am incredibly grateful for the valuable time and enormous patience she has invested in me throughout the last four years. Under her comprehensive guidance, I have made progress both in my academic pursuits and personal growth, gradually maturing from a boy to a responsible adult. I will never forget my doctorate time and will always be proud that I was her student.

Secondly, I am deeply grateful to my co-supervisor, Prof. Kaiyou Wang, at the Institute of Semiconductors, Chinese Academy of Sciences. From experiments to academic writing, from discussing project ideas to sharing life experiences, Prof. Kaiyou Wang has guided me in many aspects with his wisdom and patience.

I am very grateful to Dr Oleg Makarovskiy for his instruction and assistance with the technical aspects of the experiments throughout my PhD. The module he taught, “Semiconductor Physics”, has also benefited me greatly. I would also like to acknowledge Prof. Laurence Eaves for our meaningful discussions of physics and culture during my annual interviews and daily life. I immensely thank Dr Zakhar R. Kudrynskiy for the thorough training and patient help with my experimental skills

early in my PhD career. And I am especially grateful to Dr Wenkai Zhu for his assistance with device fabrication and transport experiments.

I would like to thank all current and former members of the Wendy House, particularly Dr Lyudmila Turyanska, Dr Wenjing Yan, Dr Nilanthi Balakrishnan, Dr Jake Greener, Dr Debarati Mazumder, Dr Nathan Cottam, Dr James Felton, Anubhab Dey, Mujahid Shiffa, Mustaqeem Shiffa, Benjamin Dewes, Nada Alghofaili, and Ailish Gray. The precious memories spent with each one of you will always remain with me as I move forward.

I am grateful to all members of Prof. Kaiyou Wang's lab at the Chinese Academy of Sciences, both past and present, for their support and friendship. I give my thanks to Prof. Jing Zhang, Prof. Yuqing Huang, Dr Xionghua Liu, Dr Faguang Yan, Dr Zelalem Abebe Bekele, Dr Yi Cao, Dr Yuanhui Zheng, Dr Yu Sheng, Dr Pengfei Liu, Dr Yucai Li, Dr Yanru Li, Dr Chang Liu, Dr Quanshan Lv, Dr Ce Hu, Dr Yongcheng Deng, Dr Hailong Lin, Dr Tiangui Hu, Dr Ziao Wang, Dr Runze Li, Dr Xiukai Lan, Yishi Zhao, Enze Zhang, Xiaomin Zhang, Weiyang Wang, Weihao Li, Kun Lei, Jiahao Xu, Chicheng Ma, Yujing Wang, Shouguo Zhu, Xiangyu Liu, and Qian Hu. I wish you success in your work and a bright future.

I would like to express my gratitude to all the staff at the University of Nottingham, particularly, Dr Christopher Mellor, Jasbinder Chauhan, and Dr Richard Cousins for their help with sample fabrication. I would also like to acknowledge the support of our collaborators throughout the course of several research projects, Prof. Lixia Zhao (Tiangong University, China), Prof. Oleg Kolosov and Dr Eli G. Castanon

(Lancaster University), Prof. Zakhar D. Kovalyuk (National Academy of Sciences of Ukraine), Prof. Haixin Chang, Gaojie Zhang, and Hao Wu (Huazhong University of Science and Technology, China).

My deepest thanks go to my father Jinhua Xie and my mother Shengying Hu for their endless support and encouragement. Without their sacrifices, I would not be in the position I am today. Finally, I wholeheartedly thank my girlfriend Na Su. You are the strongest backing in my life.

List of publications

- 1 Xie, S., Dey, A., Yan, W., Kudrynskiy, Z. R., Balakrishnan, N., Makarovskiy, O., Kovalyuk, Z. D., Castanon, E. G., Kolosov, O., Wang, K., Patanè, A., Ferroelectric semiconductor junctions based on graphene/In₂Se₃/graphene van der Waals heterostructures. *2D Materials* **8**, 045020 (2021).
- 2 Dey, A., Yan, W., Balakrishnan, N., Xie, S., Kudrynskiy, Z. R., Makarovskiy, O., Yan, F., Wang, K., Patanè, A., Memristive effects due to charge transfer in graphene gated through ferroelectric CuInP₂S₆. *2D Materials* **9**, 035003 (2022).
- 3 Xie, S., Shiffa, M., Shiffa, M., Kudrynskiy, Z. R., Makarovskiy, O., Kovalyuk, Z. D., Zhu, W., Wang, K., Patanè, A., Van der Waals interfaces in multilayer junctions for ultraviolet photodetection. *npj 2D Materials and Applications* **6**, 61 (2022).
- 4 Zhu, W.,[†] Xie, S.,[†] Lin, H.,[†] Zhang, G., Wu, H., Hu, T., Wang, Z., Zhang, X., Xu, J., Wang, Y., Zheng, Y., Yan, F., Zhang, J., Zhao, L., Patanè, A., Zhang, J., Chang, H., Wang, K., Large room-temperature magnetoresistance in van der Waals ferromagnet/semiconductor junctions. *Chinese Physics Letters* **39**, 128501 (2022).
- 5 Hu, T., Zhao, L., Wang, Y., Lin, H., Xie, S., Hu, Y., Liu, C., Zhu, W., Wei, Z., Liu, J., Wang, K., High-sensitivity and fast-speed UV photodetectors based on asymmetric nanoporous-GaN/graphene vertical junction. *ACS Nano* **17**, 8411-8419 (2023).

List of conference abstracts

- 1 Xie, S., Dey, A., Yan, W., Kudrynskyi, Z. R., Balakrishnan, N., Makarovsky, O., Kovalyuk, Z. D., Castanon, E. G., Kolosov, O., Wang, K., Patanè, A., Graphene/ α -In₂Se₃/graphene ferroelectric semiconductor junctions. *Graphene Week 2021*, Virtual event, 20-24 September, 2021 (Poster presentation, Online).
- 2 Xie, S., Dey, A., Yan, W., Kudrynskyi, Z. R., Balakrishnan, N., Makarovsky, O., Kovalyuk, Z. D., Castanon, E. G., Kolosov, O., Wang, K., Patanè, A., Graphene/ α -In₂Se₃/graphene ferroelectric semiconductor junctions. *20th International Conference on Modulated Semiconductor Structures*, Toyama, Japan, 31 October-5 November, 2021 (Contributed talk, Online).
- 3 Xie, S., Shiffa, M., Shiffa, M., Kudrynskyi, Z. R., Makarovskiy, O., Kovalyuk, Z. D., Zhu, W., Wang, K., Patanè, A., Van der Waals interfaces in graphene/*p*-GaSe/*n*-In₂Se₃/graphene junctions for ultraviolet photodetection. *Chinese Physics Society Fall Meeting 2022*, Shenzhen, China, 17-20 November, 2022 (Poster presentation, Online).
- 4 Xie, S., Zhu, W., Lin, H., Zhang, G., Wu, H., Patanè, A., Chang, H., Wang, K., Large room-temperature magnetoresistance in all-van der Waals magnetic tunnel junctions. *Graphene 2023*, Manchester, United Kingdom, 27-30 June, 2023 (Poster presentation, In person).

Physical constants

Quantity	Symbol	Value	Unit
Boltzmann constant	k_B	1.38065×10^{-23}	$\text{J} \cdot \text{K}^{-1}$
Electron charge	e	1.60218×10^{-19}	C
Electron mass in vacuum	m_e	9.10938×10^{-31}	kg
Permittivity in vacuum	ϵ_0	8.85419×10^{-12}	$\text{F} \cdot \text{m}^{-1}$
Planck constant	h	6.62607×10^{-34}	$\text{J} \cdot \text{s}$
Reduced Planck constant ($h/2\pi$)	\hbar	1.05457×10^{-34}	$\text{J} \cdot \text{s}$
Speed of light in vacuum	c	2.99792×10^8	$\text{m} \cdot \text{s}^{-1}$

List of contents

Abstract	i
Acknowledgements	ii
List of publications	v
List of conference abstracts	vi
Physical constants	vii
List of contents	viii
1. Introduction	1
1.1 Thesis overview	3
2. Two-dimensional van der Waals crystals	6
2.1 Graphene	6
2.2 Hexagonal boron nitride.....	9
2.3 Van der Waals semiconductors.....	10
2.4 Van der Waals ferroelectrics.....	13
2.4.1 Ferroelectricity	13
2.4.2 Ferroelectricity in two-dimensional materials	14
2.4.3 Ferroelectricity in α -In ₂ Se ₃	16
2.5 Van der Waals ferromagnets.....	21
2.5.1 Magnetism.....	21
2.5.2 Magnetic tunnel junctions	22
2.5.3 Magnetism in two-dimensional materials.....	25
3. Sample fabrication	31

3.1 Photolithography	31
3.2 Electron beam lithography	34
3.3 Magnetron sputtering	36
3.4 Mechanical exfoliation of vdW crystals	37
3.5 Deterministic transfer of vdW flakes to make heterostructures.....	38
3.6 Needle-assisted transfer of graphene microsheets	39
4. Characterization techniques	42
4.1 Atomic force microscopy and piezoresponse force microscopy.....	42
4.2 Micro-photoluminescence and Raman spectroscopy.....	45
4.3 Electrical transport.....	47
4.4 Photocurrent studies.....	49
5. Van der Waals ferroelectric semiconductor junctions	51
5.1 Introduction.....	52
5.2 Characterization studies of α -In ₂ Se ₃	53
5.3 Ferroelectric semiconductor junctions in the dark.....	55
5.3.1 Transport characteristics	55
5.3.2 Transport mechanisms: thermionic injection and tunnelling.....	58
5.4 FSJs under light illumination	62
5.5 α -In ₂ Se ₃ -capped graphene field effect transistors.....	67
5.6 Summary	71
6. Van der Waals interfaces for photodetection.....	73
6.1 Introduction.....	74

6.2	Photodetectors based on graphene-contacted p -GaSe/ n -In ₂ Se ₃ junctions	75
6.3	Energy band alignment	85
6.4	Scanning photocurrent microscopy.....	89
6.5	Bias-dependent carrier recombination	94
6.6	Summary	98
7.	Room-temperature magnetoresistance in magnetic tunnel junctions.....	100
7.1	Introduction.....	101
7.2	Anomalous Hall effect in Fe ₃ GaTe ₂	102
7.3	Room-temperature magnetoresistance in Fe ₃ GaTe ₂ -based MTJs.....	105
7.4	Temperature-dependent magnetoresistance	109
7.5	Magnetoresistance in Fe ₃ GaTe ₂ /GaSe/Fe ₃ GaTe ₂ MTJs.....	112
7.6	Summary	114
8.	Conclusions and outlook.....	115
8.1	Graphene/In ₂ Se ₃ /graphene ferroelectric semiconductor junctions	115
8.2	Van der Waals interfaces for ultraviolet photodetection	116
8.3	Room-temperature magnetoresistance in magnetic tunnel junctions	117
8.4	Outlook	118
	Bibliography	122

Chapter 1

Introduction

In modern society, the processing, transmission, and storage of information rely on our ability to manipulate electrons and photons. Microelectronic devices serve as the physical basis that makes this possible. Since the 1960s, microelectronic chips have been evolving according to the empirical Moore's law, which states that the density of transistors on an integrated circuit will approximately double every two years.¹ However, up to the present day, traditional electronic devices have been scaled down to sizes of tens or even a few nanometers, leading to increasing device-failure issues, such as leakage currents and hot-carrier degradation.² Further progress with traditional electronic devices has slowed down and Moore's law is gradually losing its validity. On the other hand, two-dimensional (2D) van der Waals (vdW) semiconductors represent a promising material platform for future technologies beyond Moore's law.³

In 2004, Novoselov *et al.* successfully isolated a single atomic layer of graphene by mechanical exfoliation of highly oriented pyrolytic graphite.⁴ Graphene possesses remarkable physical properties, such as a zero bandgap, high carrier mobility, high thermal conductivity, mechanical flexibility, and quantum Hall effects.^{3,5-8} This groundbreaking discovery shattered the theory that 2D materials could not exist stably at ambient conditions due to thermal fluctuations, thus sparking widespread interest.⁹ Since then, hundreds of types of graphene-like 2D vdW layered materials have been studied, such as wide-bandgap insulator hexagonal boron nitride (hBN), metal

chalcogenides (MCs, *e.g.* InSe, In₂Se₃, GaSe), transition metal dichalcogenides (TMDCs, *e.g.* MoS₂, WSe₂) and metal oxides (*e.g.* TiO₂, TaO₃), *etc...*¹⁰ Unlike traditional three-dimensional covalent materials, 2D layered materials feature strong covalent bonds in the layer plane while there is a weak vdW interaction between the vdW layers.¹⁰ In monolayer and few-layer 2D materials, electrons move within the plane and are subject to quantum confinement. This leads to unique physical properties, including exceptional optical, electrical, and magnetic characteristics. Additionally, due to the absence of dangling bonds on the surface of a vdW crystal, it is possible to construct a wide variety of vdW heterostructures without the constraint of lattice matching that applies to traditional semiconductors. This offers opportunities for exploring novel optical, electrical, and magnetic devices based on 2D heterostructures.

The recent discovery of ferroelectricity and ferromagnetism in 2D vdW materials has broadened prospects for new discoveries, that could revolutionise next-generation nanoelectronics and spintronics.^{11,12} For example, 2D vdW ferroelectric materials can serve as ideal components in ferroelectric tunnel junctions (FTJs) due to their layered structures.^{13,14} Wu *et al.* used 4-nm-thick CuInP₂S₆ as the tunnelling barrier and achieved a tunnelling electroresistance (TER) exceeding 10⁷, which is attributed to a Fermi level shift as large as 1 eV by the polarization switching.¹⁵ Also, by enhancing the effective gate electric field in the device, vdW ferroelectric field-effect transistors (Fe-FET) can produce a negative capacitance effect, reducing the subthreshold swing down to or even lower than the Boltzmann's

limit (60 mV/dec). This can increase switching speeds of the device and improves energy efficiency.^{16,17} On the other hand, 2D vdW magnets provide new opportunities for control of magnetism at the nanometre scale via strain, voltage and the photovoltaic effect.^{11,18,19} For instance, Dąbrowski *et al.* demonstrated that the magnetism of CrI₃ layers can be manipulated with laser pulses,²⁰ and Tang *et al.* succeeded to control the magnetic anisotropy in vdW Fe₅GeTe₂ via electrolyte gating.²¹

Motivated by these burgeoning researches, my PhD research project aims to explore novel quantum systems based on 2D vdW crystals. Of particular interest is the recently discovered ferroelectric α -In₂Se₃ and the ferromagnetic Fe₃GaTe₂, which are used to build novel vdW heterostructures. These offer innovative ways of studying and harnessing charge- and spin-quanta in multi-layered structures, providing an exciting platform for future technologies, such as ferroelectric memristors and magnetic tunnel junctions for non-volatile memories and low-power electronics.

1.1 Thesis overview

The thesis is structured as follows:

Chapter 1 encompasses the introduction, motivation, and an overview of the content presented in the subsequent chapters of this thesis.

Chapter 2 introduces the research background, characteristics and applications of 2D vdW materials, including graphene, hexagonal boron nitride (hBN), and 2D semiconductors. In particular, the properties of ferroelectric and ferromagnetic

materials and their progress in the field of 2D systems are presented.

Chapter 3 describes the fabrication techniques used to construct the vdW heterostructures studied in the experiments, including traditional semiconductor fabrication processes and 2D material transfer technology.

Chapter 4 describes the advanced characterization techniques used to study the vdW materials and devices investigated in the thesis. The equipment for measuring electrical, magnetic and optoelectronic properties of devices based on 2D layered materials and their heterostructures are also presented.

Chapter 5 investigates the electronic and optoelectronic properties of graphene/ α -In₂Se₃/graphene ferroelectric semiconductor junctions. By modulating the ferroelectric polarization of the nanometre-thick α -In₂Se₃ layer in the devices, controllable memristive effects are achieved and the underlying mechanisms of conduction are examined.

Chapter 6 studies the photoresponse of graphene-contacted p -GaSe/ n -In₂Se₃ junctions. A large photoresponsivity (up to $\sim 10^2$ A/W) and a high detectivity (up to $\sim 10^{13}$ Jones) are observed in the devices. These are explained in terms of charge transport across multiple thin layers and light-current conversion at the vdW interfaces of the junction.

Chapter 7 explores room-temperature tunnel magnetoresistance in magnetic tunnel junctions based on vdW Fe₃GaTe₂/WSe₂/Fe₃GaTe₂ heterostructures. The changes of magnetoresistance with temperature in these devices are discussed and the intrinsic above-room-temperature ferromagnetism in Fe₃GaTe₂ is characterised by the

anomalous Hall effect.

Chapter 8 concludes the thesis, providing a summary of the key findings and a discussion of future research prospects.

Chapter 2

Two-dimensional van der Waals crystals

Research on two-dimensional (2D) van der Waals (vdW) materials can be traced back to the successful isolation of single-layer graphene sheets exfoliated from bulk graphite.⁴ This achievement has sparked significant interest in the investigation of additional 2D materials, with a diverse range of physical properties, enabling the discovery of various quantum phenomena and the fabrication of new functional devices.^{6,8,22,23} In this chapter, we present an overview of the characteristics and applications of 2D vdW materials, including graphene, hexagonal boron nitride (hBN), 2D semiconductors, ferroelectrics, and ferromagnets. These are the 2D materials that have been used in this thesis.

2.1 Graphene

Graphene is an allotrope of carbon in the form of a single layer of atoms arranged into a 2D hexagonal lattice with one C-atom at each vertex (Figure 2.1a). The unique structural properties of graphene are reflected in its electronic properties. The K and K' points in the reciprocal lattice (Figure 2.1b) establish a valley-based degree of freedom, combined with spin, resulting in a four-fold degeneracy of the energy bands. The Dirac points are at K and K' , representing the boundary between the conduction and valence bands (Figure 2.1c).^{6,7} Due to the cone-shaped energy-momentum relations, the quasi-particles with electron- and hole-like properties travel at a constant velocity, $v_F \approx 10^6$ m/s, dictated by the cone's gradient.²⁴

As a result, graphene shows many exceptional properties, including bipolar conduction with highly tunable carrier densities, high carrier mobility, *etc.*⁷ Because of its tuneable chemical potential, high conductivity, and optical transparency, graphene has been seen as a promising material for applications in sensor, photonic, and electronic devices.^{5,8,25} Also, graphene is an ideal candidate to serve as an electrode to a vdW material within a device structure because of its compatibility with other vdW crystals to create heterostructures.²⁶⁻²⁹

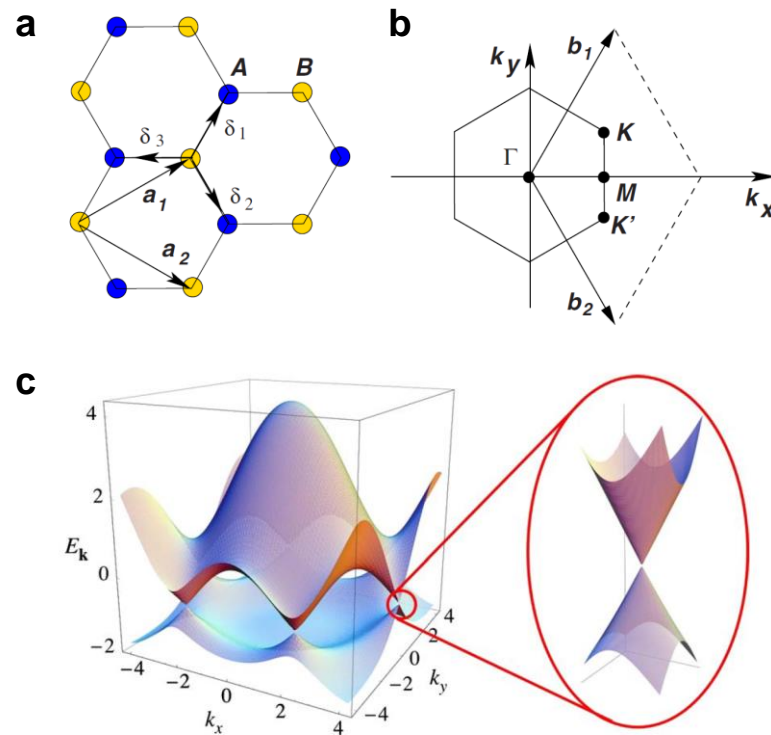


Figure 2.1 Structures of graphene. (a) The honeycomb lattice structure of graphene in real space. Two sublattice sites are labelled A and B . The unit cell is marked by the lattice vectors a_1 and a_2 . (b) The reciprocal lattice of graphene with the corresponding Brillouin zone. The Dirac cones are located at the K and K' points. (c) Energy (E_k) - momentum ($k_{x,y}$) dispersion of graphene and representation of the band structure around the Dirac point in the Brillouin zone. The figure is reproduced from Ref.⁷.

In 2018, Cao *et al.* discovered interaction-induced insulating states and superconductivity in twisted bilayer graphene (TBG) with a special magic twist angle.^{30,31} TBG is an exciting system where two layers of graphene are stacked on top of each other with a small twist angle between them. This twist angle introduces a moiré pattern, which is an interference effect that forms a large-scale superlattice. When the twist angle is close to a specific value, known as the "magic angle" (approximately 1.1°), the electronic properties of TBG change dramatically, giving rise to interaction-induced insulating states and superconductivity. At the magic angle, the interlayer hybridization induces nearly flat low-energy bands (as shown in Figure 2.2a). This quenching of the quantum kinetic energy leads to a correlated insulating phase at half-filling of these flat bands, which is indicative of a Mott-like insulator in the localized flat bands (Figure 2.2b).³⁰ In addition to the insulating states, superconductivity has also been observed in magic-angle TBG (Figure 2.2c). When the electron density is tuned through electrostatic gating, superconducting phases can emerge close to the interaction-induced insulating states. Figure 2.2d displays interaction-induced insulating states at integer moiré band fillings accompanied by nearby superconducting regions, which shows similarity with the behaviour of other high-temperature superconductors.³¹ The exact mechanism of superconductivity in magic-angle TBG is still under active investigation. Unveiling interaction-related insulating states and superconductivity in TBG with a magic twist angle has paved the way for investigating strongly correlated electronic systems and their potential applications in next-generation electronic devices.^{24,32}

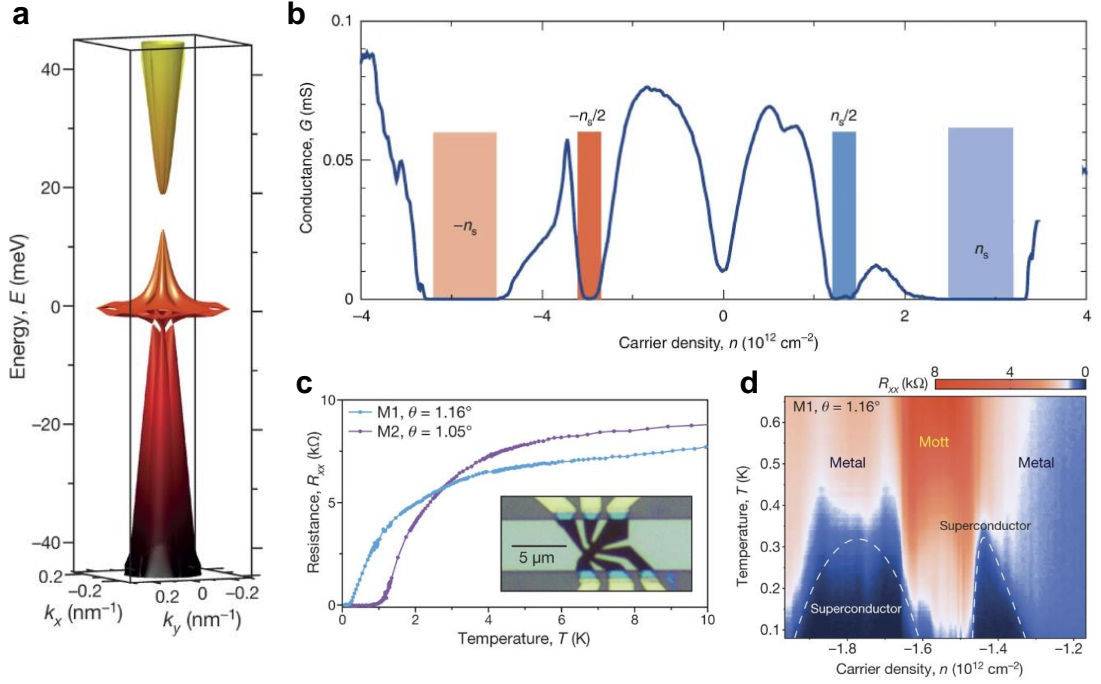


Figure 2.2 Insulating states and superconductivity in magic-angle TBG. (a) The band structure of TBG shows the formation of a narrow band near the charge neutrality when approaching the magic angle. (b) Conductance of a magic-angle TBG device with $\theta = 1.08^\circ$ and $T = 0.3$ K. The Dirac point is located at $n = 0$. The lighter-shaded regions are superlattice gaps at carrier density $\pm n_s$. The darker-shaded regions denote half-filling states at $\pm n_s/2$. (c) Four-probe resistance $R_{xx} = V_{xx}/I$ for two Hall bar devices shows the superconductivity in magic-angle TBG. The inset shows an optical image of a magic-angle TBG Hall bar device. (d) Phase diagram showing the dependence of the superconducting critical temperature on carrier density. The figure is reproduced from Ref.^{30,31}.

2.2 Hexagonal boron nitride

Hexagonal boron nitride (hBN) is a 2D material composed of boron (B) and nitrogen (N) atoms organized in a hexagonal lattice pattern. Often referred to as "white graphene", crystalline hBN is arranged in a graphene-like layered structure.³³ However, hBN has different electronic and optical properties compared to graphene,

which makes it a distinct material with a wide range of potential applications.³⁴

As a 2D vdW insulator (bandgap ~ 6 eV), hBN plays a pivotal role in a multitude of scientific and technological disciplines, for example, as a platform for gate dielectric, a passivation layer, Coulomb drag, and a tunnelling layer.³⁵⁻³⁹ hBN hosts defects that can be engineered to obtain room-temperature, single-photon emission and is well suited for deep UV emitters and detectors.^{40,41} Furthermore, the partially ionic structure of the BN layers in hBN reduces covalency and electrical conductivity, whereas the interlayer interaction increases resulting in higher hardness of hBN relative to graphite.³³ In this thesis, hBN layers were used to encapsulate the entire vdW devices and prevent other 2D materials from oxidation.

2.3 Van der Waals semiconductors

Semiconductors are the basis of many vital technologies such as computing, communications and sensing.^{42,43} Modern semiconductor technology can trace its origins to the invention of the point-contact transistor in 1947.⁴⁴ This ground-breaking achievement led to the creation of semiconductor devices and integrated circuits, which have become integral to our contemporary society. A key property that determines the semiconductor's electrical and optical properties is the bandgap. Beyond graphene and hBN, recently discovered vdW materials exhibit semiconducting bandgaps that span various ranges, from terahertz and mid-infrared in bilayer graphene and black phosphorus, to visible light in metal chalcogenides (MCs), and up to ultraviolet in Ga_2N_3 (Figure 2.3).⁴⁵

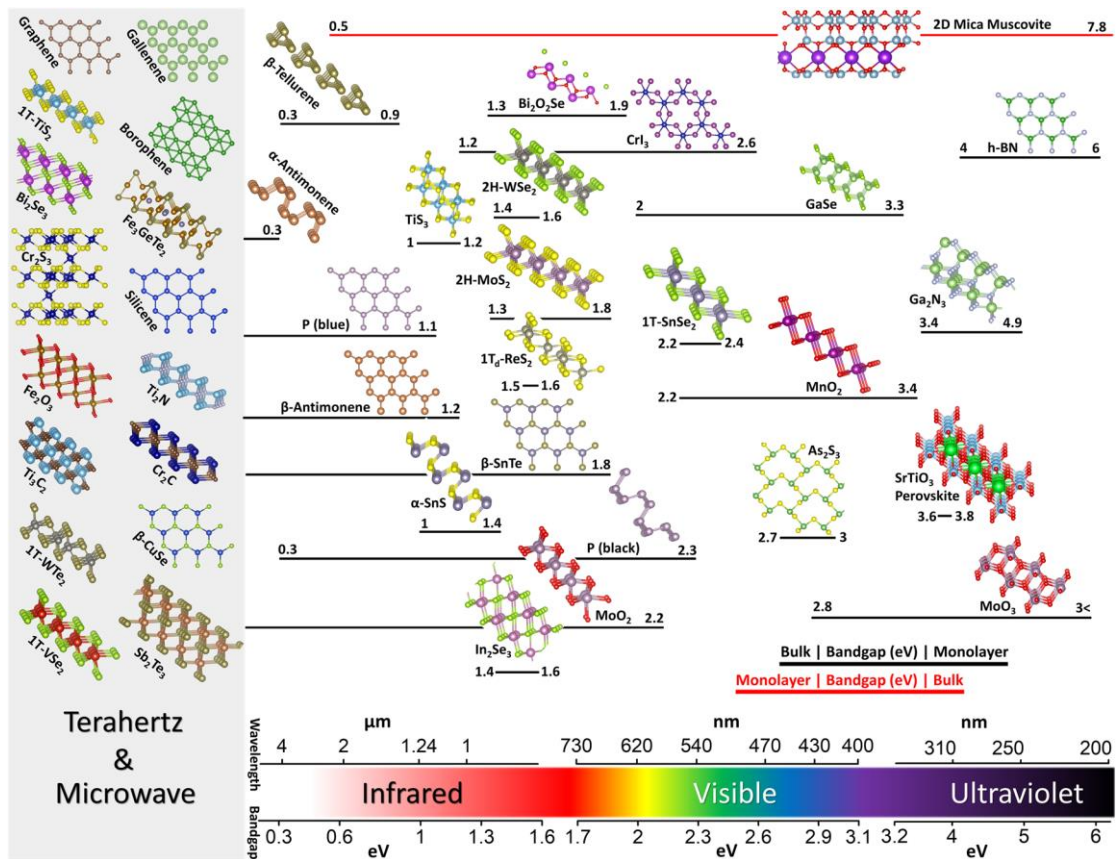


Figure 2.3 Bandgaps of 2D semiconductors. The bars beneath each structure indicate bandgap range from bulk to monolayer. Normally, the bulk bandgap is smaller than that of its monolayer (black bars), but there are exceptions (red bars). 2D materials on the far left are zero or near-zero bandgap, metallic, or semimetallic. The figure is reproduced from Ref.⁴⁵.

Among the wide catalogue of 2D semiconductors, the III–VI MC compounds have emerged as an ideal class of materials for electronics and optoelectronics.^{28,46-52} MCs are semiconducting crystals with the stoichiometry MX or M_aX_b , where M is a metal (*e.g.* Ga, In, *etc.*) and X is a chalcogen (*e.g.* S, Se, Te, *etc.*). Similar to graphene and hBN, these crystals possess strong in-plane covalent bonds in each layer and the layers interact through weak vdW forces. However, in contrast to graphene, MCs exhibit a wide variety of polytypes, for example, β , γ and ϵ for InSe⁵³, and β , ϵ , γ and δ

for GaSe^{53,54}, depending on the stacking sequence of the layers. Earlier studies of these bulk crystals focused on their anisotropic mechanical, optical and electronic properties, which made them good candidates for applications in photovoltaic, non-linear optics and THz generators.⁵⁵⁻⁵⁹

In this thesis, we have used the MC α -In₂Se₃ and the MC ϵ -GaSe. The ϵ -polytype phase of GaSe crystals was obtained by Bridgman growth.⁶⁰ Each ϵ -GaSe layer consists of four closely packed, covalently bonded, monoatomic sheets in the sequence Se-Ga-Ga-Se. The two vdW ϵ -GaSe layers have a weak vdW bonding, which helps this material to be cleaved into layers using mechanical exfoliation.⁶¹ The in-plane lattice parameters are $a = b = 3.755 \text{ \AA}$ and each unit cell consists of two layers with out-of-plane lattice parameters $c = 15.949 \text{ \AA}$. As a p -type semiconductor, GaSe crystals contain native acceptors and a low concentration of holes $p \sim 10^{13} \text{ cm}^{-3}$ at $T = 300 \text{ K}$.⁶⁰

ϵ -GaSe shows layer-dependent optoelectronic properties. GaSe is a direct bandgap material in the bulk form (with a bandgap $\sim 2 \text{ eV}$) and becomes indirect in the monolayer form (with a bandgap $\sim 4 \text{ eV}$).⁶² Because of the high resistivity of the GaSe-layered structure, the dark current in devices based on GaSe is very low, which is advantageous for photodetection.^{48,63}

We investigated graphene/ ϵ -GaSe/ α -In₂Se₃/graphene heterostructures with strong optical absorption in the ultraviolet range.⁶⁴ This work is presented in Chapter 6. The properties of the ferroelectric semiconductor α -In₂Se₃ are described in Section 2.4.3.

2.4 Van der Waals ferroelectrics

In this section, we explore the background and intriguing properties of ferroelectric materials, particularly focusing on the emergence of 2D vdW ferroelectrics. A detailed description of ferroelectricity in α -In₂Se₃, a semiconductor vdW crystal, is presented by highlighting its ferroelectric mechanisms and its applications in nanoelectronics, photodetectors, and memory devices.

2.4.1 Ferroelectricity

The investigation of ferroelectricity in solid-state systems represents an active area of research with many breakthroughs emerging from both experiments and theory.⁶⁵ In the development of modern electronics, ferroelectrics play an increasingly important role with novel applications, such as high energy density capacitors, resistive switches, electro-optic modulators, ferroelectric tunnel junctions (FTJs) and non-volatile ferroelectric random-access memories (FeRAMs).⁶⁶⁻⁶⁹

A ferroelectric is generally defined as a material that possesses a spontaneous electric polarization P , which can be reversed through the application of an external electric field E , greater than the coercive field E_C .^{70,71} The term "ferroelectricity" is derived from the word "ferromagnetism", as both phenomena exhibit hysteresis behaviour, though they involve different properties (electric polarization in ferroelectric materials and magnetization in ferromagnetic materials). The Curie temperature (T_C) of a ferroelectric material is the critical temperature at which the material undergoes a phase transition from a ferroelectric phase to a paraelectric

phase.⁷² Above the Curie temperature, the spontaneous polarization of the material vanishes, and the material loses its ferroelectric properties. All ferroelectrics are also pyroelectrics, which means that these materials can generate a temporary voltage when they are heated or cooled. Moreover, all ferroelectrics are also piezoelectric, which means that they can generate charges in response to an applied mechanical stress.⁷⁰

Since 1921, when Joseph Valasek first recognized ferroelectric properties in a crystal, namely in Rochelle salt, ferroelectric materials have been continuously discovered and studied over decades.⁷³ In the last century, studies of ferroelectric materials have mainly focused on hydrogen-bonded materials, such as Rochelle salt, or complex oxides, such as BaTiO₃ and PbTiO₃ perovskite compounds.^{74,75} Driven by the technological demand for device miniaturization, the exploration of the ferroelectric properties of perovskite thin films has attracted increasing attention.⁷⁶ At the same time, the recent emergence of vdW ferroelectrics with 2D structures introduced new opportunities in the field.¹²

2.4.2 Ferroelectricity in two-dimensional materials

The layered structure of 2D vdW materials allows for the fabrication of stable single- and few-layer samples, which provide an excellent platform for exploring the impact of reduced lattice dimensions on the long-range ferroelectric order.¹² The study of vdW ferroelectrics can be traced back to the work of Pawley *et al.* in the 1960s on group IV-VI metal chalcogenides (MC, where M = Ge/Sn; C = S/Se/Te).⁷⁷ Early

studies were mostly conducted on bulk samples. Later, with the development of thin-film growth techniques and the more recent introduction of mechanical exfoliation, the fabrication of atomic-thin samples of vdW ferroelectric materials became possible. In 2016, robust in-plane polarization in monolayer SnTe and out-of-plane polarization in 4-nm-thick (~ 5 layers) CuInP₂S₆ were discovered.^{78,79} Since then, ferroelectricity has been demonstrated in many 2D vdW systems, including In₂Se₃,^{80,81} WTe₂,^{82,83} ReS₂,⁸⁴ MoTe₂,⁸⁵ SnSe and SnS.⁸⁶

Table 2.1 Summary properties of 2D vdW ferroelectric materials. E_C represents the coercive field, T_C represents the Curie temperature, and L indicates the number of vdW layers. The table is reproduced from Ref.¹².

Material	E_C (V nm ⁻¹)	T_C (K)	Bandgap (eV)	References
CuInP ₂ S ₆	0.01 (bulk)	>320 (5L)	2.7 (bulk)	79
CuCrP ₂ S ₆	—	32 (bulk)	—	87
SnTe	—	270 (1L); 100 (bulk)	1.6 (1L); 0.3 (bulk)	88
SnSe	0.014 (1L)	>380 (1L)	2.1 (1L); 0.9 (bulk)	78,86
SnS	2.5×10^{-3} (9L); 1.1×10^{-3} (bulk)	>300 (1L)	1.6 (1L); 1.2 (bulk)	86
GeTe	0.2	570 (1L)	0.6 (bulk)	86
α -In ₂ Se ₃	0.02	700 (4L)	2.8 (1L); 1.4 (bulk)	80,89
MoTe ₂	—	330 (1L)	0	85
WTe ₂	0.05	350 (2-3L)	0	82
Bilayer WSe ₂ , MoSe ₂ , WS ₂ , MoS ₂ , MoTe ₂	0.2	>300 (2L)	—	90,91
Bilayer MoS ₂ /WS ₂	2.4	>300 (2L)	0 (2L)	92
Bilayer hBN	0.1	>300 (2L)	>5 (bulk)	93
Bilayer graphene	0.2	>300 (2L)	—	23

Due to the inversion symmetry break, unconventional ferroelectricity has also been seen in moiré superlattices, such as Bernal-stacked bilayer graphene, parallel-stacked bilayer hBN, rhombohedral-stacked bilayer WSe₂, MoSe₂, WS₂ and MoS₂.^{23,90,93} The properties of some 2D vdW ferroelectrics are summarized in Table 2.1. Beyond that, researchers have identified novel 2D vdW ferroelectric systems with unique mechanisms (such as sliding ferroelectrics^{83,94,95} and spin-texture-induced ferroelectrics⁹⁶), uncovered unprecedented properties (such as ferroelectric metallicity⁸²), and developed functional devices (such as negative capacitance transistors¹⁶) that capitalize on the distinctive ferroelectric characteristics.

2.4.3 Ferroelectricity in α -In₂Se₃

In₂Se₃ is a semiconductor vdW crystal with remarkable optical and electrical properties. It has been studied in the application of photodetectors and phase-change memories for a long time. In₂Se₃ can exist in several phases (*e.g.* α -In₂Se₃, β -In₂Se₃, γ -In₂Se₃, δ -In₂Se₃...) depending on material preparation conditions.^{53,81,97} Amongst these phases, the α -phase of In₂Se₃ is recognized as the most stable layered structure at room temperature. As shown in Figure 2.4a, its single layer is composed of alternating Se or In atomic layers via covalent bonds, constituting a Se–In–Se–In–Se quintuple layer (QL). The QLs are vertically stacked in the A-B-C sequence via weak vdW forces. The vdW nature of the inter-QL force is supported by earlier experimental observations that few-layer In₂Se₃ can be obtained by mechanical exfoliation, epitaxy, or chemical vapour deposition.^{56,97,98}

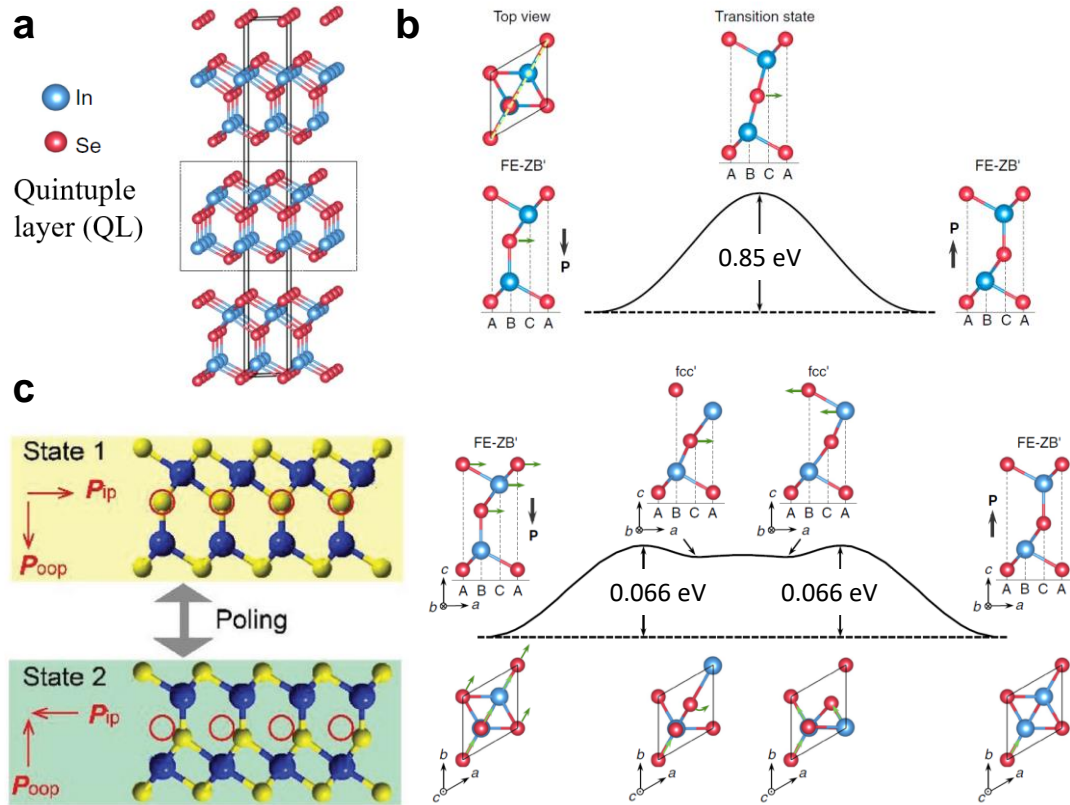


Figure 2.4 Crystal structure and ferroelectric properties of α - In_2Se_3 . (a) Crystal structure of layered α - In_2Se_3 . A quintuple layer (QL) is indicated by the black square. (b) Two kinetics pathways for the polarization reversal involving the motion of Se-atoms. Direct shift (top figure b): a Se-atom in the QL shifts laterally from the B to C sites, thus reversing the direction of the polarization. The activation energy barrier for this shift is 0.85 eV. Indirect shift (bottom figure b): After the movement of four atoms in the QL, the Se-atom originally located at point B moves to C. The activation energy barrier of this shift is 0.066 eV, which is the polarization inversion pathway with the least energy required. (c) The α - In_2Se_3 crystal structure depicting the interlocked polarization mechanism in the out-of-plane (OOP) and in plane (IP) orientations. The yellow and blue balls represent Se and In atoms, respectively. By applying a large bias that exceeds the coercive voltage, the central Se-atoms, which are the origin of the interlocked spontaneous polarization, move towards the bottom right direction, simultaneously reversing the OOP and IP dipoles (State 1 \rightarrow State 2). The figure is adapted from Ref.^{89,99}.

For bulk α -In₂Se₃, the nature of the bandgap, *i.e.*, direct or indirect, remains controversial. Some experimental works in the literature report that bulk α -In₂Se₃ has a direct gap,^{100,101} while other experimental¹⁰² and theoretical^{81,103,104} studies show that it has an indirect bandgap. The Brillouin zone of bulk α -In₂Se₃ is shown in Figure 2.5a. As shown in Figure 2.5c, first-principles calculations from a recent work indicate that bulk α -In₂Se₃ is an indirect bandgap semiconductor: the valence-band maximum (VBM) occurs along the Γ -L direction, while the conduction-band minimum (CBM) is located at Γ ; the energy of the indirect bandgap is $E_g = 1.27$ eV, while that of the direct bandgap at Γ is 1.32 eV.⁸¹ The experimental measured values of the bandgap for α -In₂Se₃ films in the literature range between 1.2 and 2.8 eV.^{56,105,106}

The Brillouin zone of single layer α -In₂Se₃ is shown in Figure 2.5b. The bandgap and its nature (direct/indirect) depend on the layer thickness: as the thickness of α -In₂Se₃ decreases, the optical bandgap energy increases and the nature of bandgap changes from indirect to direct.^{103,105,106} Figure 2.5e shows the Tauc plots for seven α -In₂Se₃ flakes with different thicknesses, from 3.1 to 28.6 nm, as well as their linear fit near the absorption edge, as reported in an experimental work.¹⁰⁶ The optical bandgap is strongly dependent on the flake thickness, increasing from its bulk value of 1.45 ± 0.05 eV to a value of 2.80 ± 0.05 eV for the thinnest measured flake (3.1 nm thick). The transition from an indirect to a direct bandgap with decreasing layer thickness is confirmed by a recent theory work in the literature,¹⁰³ showing that the bandgap of single layer α -In₂Se₃ is direct: the calculated band structure with

Perdew-Burke-Ernzerhof (PBE) without spin-orbit coupling (SOC) (see red lines in Figure 2.5d) show that α -In₂Se₃ monolayers are indirect bandgap semiconductors; however, when the SOC is included (see black lines in Figure 2.5d), the bandgap becomes direct.¹⁰³ This finding confirms the measurement of Jacobs-Gedrim *et al.*,⁵⁶ suggesting a direct bandgap for vdW α -In₂Se₃ with a thickness of ~ 3.9 nm.

In 2017, intrinsic out-of-plane (OOP) and in-plane (IP) ferroelectricity was predicted for α -In₂Se₃ by first-principles calculations.⁸⁹ In one QL In₂Se₃, each ground state structure hosts two equivalent states with opposite electric polarizations. As shown in Figure 2.4b, there are two kinetics pathways for the polarization reversal. Furthermore, the unique structural asymmetry of α -In₂Se₃ causes strict interlocking between OOP and IP dipoles (Figure 2.4c), which means polarization reversal in α -In₂Se₃ can be realized by bias poling along either the OOP or IP orientation.¹⁰⁷⁻¹⁰⁹ The dipole interlocking effect is a completely new mechanism to stabilize 2D ferroelectricity, providing a new degree of freedom to control structural and electronic ordering. In addition, the transition temperature T_C of α -In₂Se₃ is around 700 K, which means that α -In₂Se₃ is a stable ferroelectric material at room temperature.¹⁰⁸ Because of its extraordinary ferroelectric and optoelectronic properties, α -In₂Se₃ finds extensive applications in nanoelectronics, photodetectors, non-volatile memory devices, and strain sensors.^{57,99,109-123} In our study, we fabricated graphene/ α -In₂Se₃/graphene ferroelectric semiconductor junctions which shows memristive effects that can be controlled by applied voltages and/or by light.¹²⁴ This work is presented in Chapter 5.

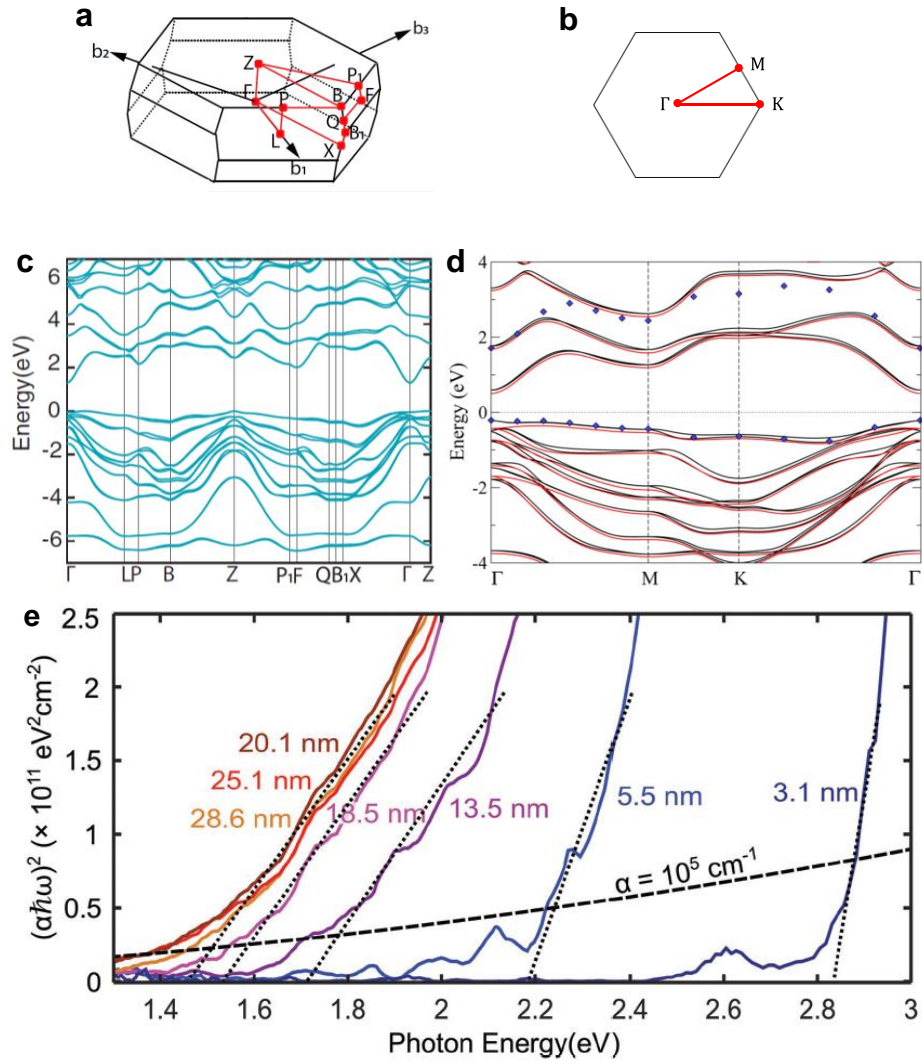


Figure 2.5 Band structures of α -In₂Se₃. (a) The Brillouin zone of bulk α -In₂Se₃. (b) The Brillouin zone of single layer α -In₂Se₃. (c) Calculated band structure of bulk α -In₂Se₃, including the effects of spin-orbit coupling (SOC). The valence-band maximum (VBM) is set to 0 eV. (d) Calculated band structure of a single α -In₂Se₃ layer with (black line) and without (red line) inclusion of SOC. The Fermi level is set to 0 eV. (e) Tauc plot of the optical absorption in α -In₂Se₃ flakes with seven different thicknesses, ranging from 28.6 to 3.1 nm. The dotted lines show the Tauc extrapolation of the absorption edge. The energy at which the absorption coefficient takes a value of 10^5 cm^{-1} (isoabsorption energy) is shown by the black dashed curve. The figure is reproduced from Ref.^{81,103,106}.

2.5 Van der Waals ferromagnets

In this section, we provide an overview of the various forms of magnetism, along with the mechanisms and examples of magnetic tunnel junctions (MTJs). Moreover, we delve into the recent appearance of 2D vdW magnetic materials, emphasizing their unique characteristics that have catalyzed progress in the field of spintronic devices.

2.5.1 Magnetism

Magnetism encompasses a set of physical properties mediated by a magnetic field, which has the ability to generate attractive and repulsive forces in other objects.¹²⁵ Diamagnetism, paramagnetism, ferromagnetism, ferrimagnetism, and antiferromagnetism are different types of magnetism. Diamagnetic materials possess no unpaired electrons and have a weak, negative response to external magnetic fields. They are repelled by magnetic fields but do not retain any magnetism when the field is removed. Paramagnetic materials possess unpaired electrons and have a weak, positive response to external magnetic fields. Their magnetic moments align with the field, but the magnetism disappears when the field is removed. Ferromagnetic materials possess unpaired electrons that align their magnetic moments when subjected to an external magnetic field. They exhibit strong attraction to magnetic fields and can be magnetized to become permanent magnets. The Curie temperature (T_C) is used to describe the temperature of the phase transition between paramagnetism and ferromagnetism. Ferrimagnetism occurs in materials with a mixed magnetic structure where the magnetic moments of different ions partially cancel each

other out, resulting in a net magnetization. Ferrimagnetic materials can be magnetized like ferromagnetic materials, but their magnetic properties are generally weaker. In antiferromagnetic materials, the magnetic moments of adjacent atoms or ions align in opposite directions, resulting in a net magnetization of zero. Antiferromagnetism vanishes at and above the Néel temperature.^{125,126} The schematic diagrams of the five types of magnetism are shown in Figure 2.6.

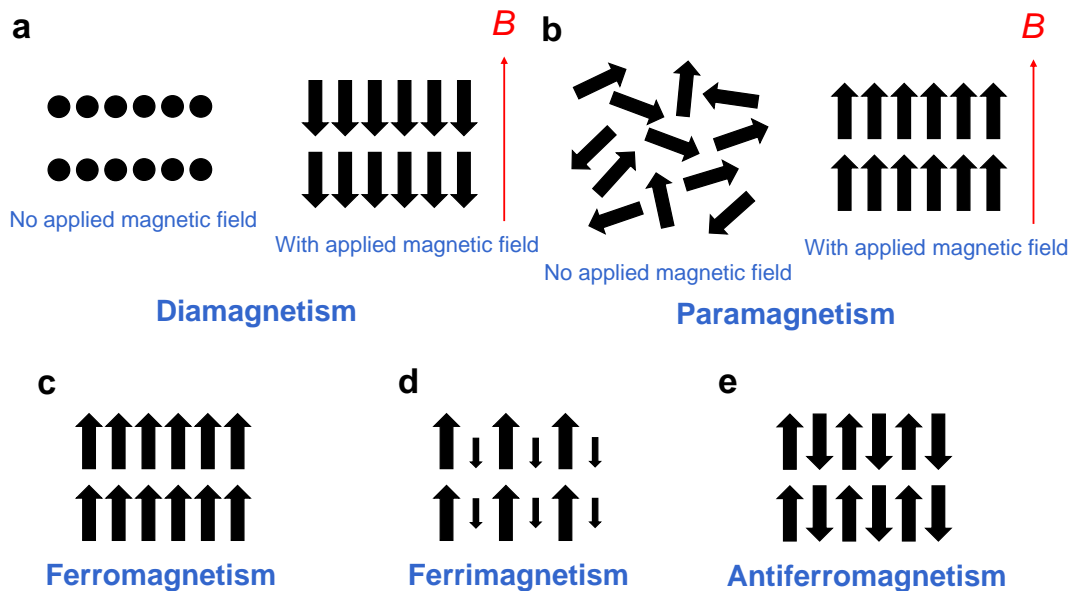


Figure 2.6 Different types of magnetism. Schematics of (a) diamagnetism, (b) paramagnetism, (c) ferromagnetism, (d) ferrimagnetism, and (e) antiferromagnetism.

2.5.2 Magnetic tunnel junctions

Magnetic tunnel junctions (MTJs) serve as essential components in hardware such as magnetic random-access memory (MRAM) and hard disk drives. They typically feature a ferromagnet/non-magnet/ferromagnet trilayer structure, which displays a low resistance state when the magnetization directions of the two

ferromagnetic layers align parallel and a high resistance state when they are antiparallel. These high and low resistance configurations correspond to logical "1" and "0" values.

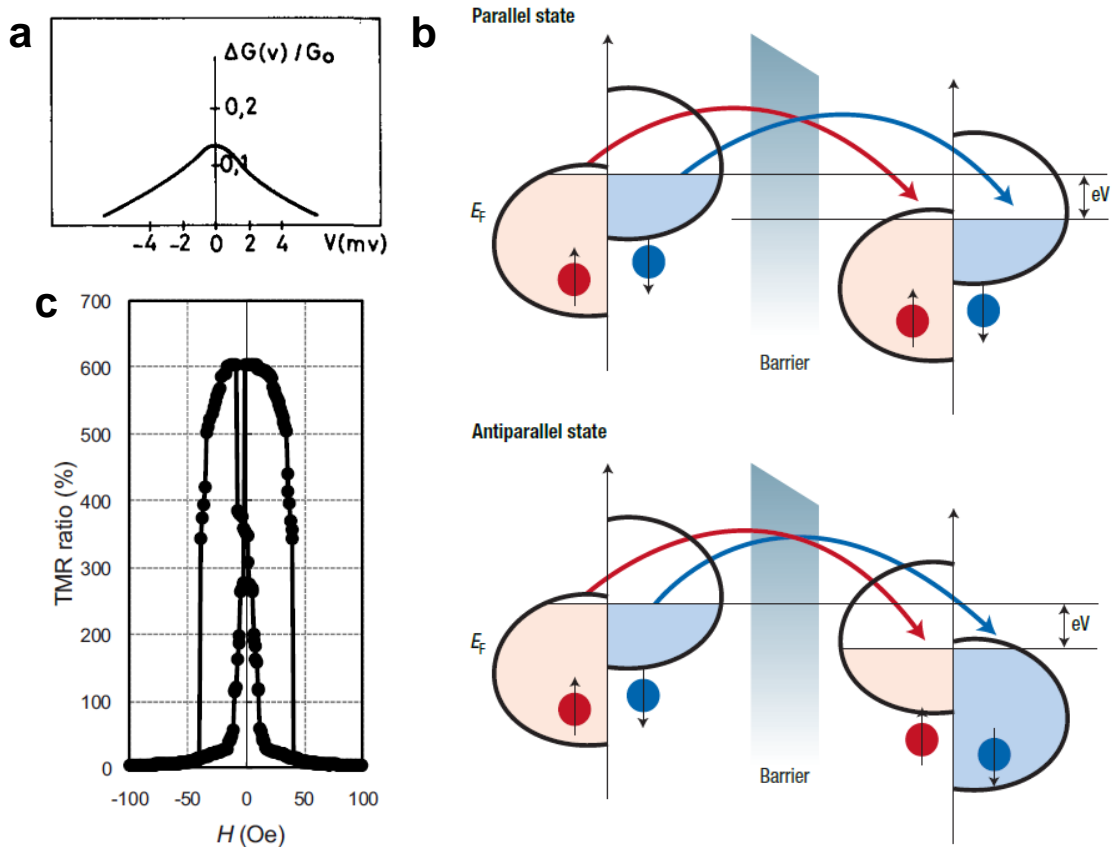


Figure 2.7 Tunnel magnetoresistance in magnetic tunnel junctions. (a) TMR versus bias voltage in the first MTJ, a Fe/Ge/Co junction, at $T = 4.2$ K. (b) Schematic representation of the tunnel magnetoresistance in the case of two identical ferromagnetic metal layers separated by a non-magnetic amorphous insulating barrier. The tunnelling process conserves the spin. When electron states on each side of the barrier are spin-polarized, then electrons will more easily find free states to tunnel to when the magnetizations are parallel (top) than when they are antiparallel (bottom). (c) The TMR ratio in a CoFeB/MgO/CoFeB MTJ at $T = 300$ K. The figure is reproduced from Ref.¹²⁷⁻¹²⁹.

In 1975, Julliere pioneered the fabrication of the first MTJ, an Fe/Ge/Co tunnel junction.¹²⁷ When applying a magnetic field to change the parallel and antiparallel magnetization states of the tunnel junction, the change in magnetoresistance was successfully observed.

The tunnel magnetoresistance (TMR) is defined as:

$$\text{TMR} = \frac{R_{AP} - R_P}{R_P} \times 100 \%, \quad (2.1)$$

where R_P and R_{AP} represent the resistance of the tunnel junction in parallel and antiparallel states, respectively. As shown in Figure 2.4a the TMR in the first Co/Ge/Fe structure reached a value of 14% at low temperature ($T = 4.2$ K) and zero bias voltage.

In order to explain the TMR effect, one can assume that the electron spin remains unchanged during tunnelling and that the tunnelling processes for spin-up and spin-down electrons are independent. Next, the conductance $G = 1/R$ of the two independent tunnelling channels is proportional to the product of the corresponding spin state densities of the two ferromagnetic electrodes, as illustrated in the energy band diagram of Figure 2.7b.¹³⁰ Based on these assumptions:

$$G_P \propto D_1^\uparrow D_2^\uparrow + D_1^\downarrow D_2^\downarrow, \quad (2.2)$$

$$G_{AP} \propto D_1^\uparrow D_2^\downarrow + D_1^\downarrow D_2^\uparrow. \quad (2.3)$$

Here, D^\uparrow and D^\downarrow represent the density of states of two different spin configurations, and subscripts “1” and “2” denote the two ferromagnetic layers. As the spin polarization P of the ferromagnet is defined as $P = \frac{D^\uparrow - D^\downarrow}{D^\uparrow + D^\downarrow}$, the famous Julliere formula can be derived:¹²⁷

$$TMR = \frac{R_{AP}-R_P}{R_P} = \frac{G_P-G_{AP}}{G_{AP}} = \frac{2P_1P_2}{1-P_1P_2} \times 100 \%. \quad (2.4)$$

Based on earlier measurements of Fe and Co spin polarization rates,^{131,132} the theoretical TMR value for the Fe/Ge/Co tunnel junction is 26%, higher than the experimental result (14%). The discrepancy could be due to spin-flip scattering at the interface, the leakage of the Ge spacer layer, and magnetic coupling between the ferromagnetic electrodes.¹²⁷

With the advancement of material growth techniques, MTJs have experienced widespread study. In 2007, Wei *et al.* fabricated a CoFeB/Al₂O₃/CoFeB structure using CoFeB as the ferromagnetic electrode, raising the room temperature TMR of the Al₂O₃-based MTJ structure to 81%.¹³³ Currently, the highest recorded TMR value at room temperature is 604%, measured by Ikeda *et al.* in a CoFeB/MgO/CoFeB junction in 2008 (Figure 2.7c), which benefits from the excellent spin filter effect of the spacer MgO.¹²⁹ On the other hand, the extensive research of 2D vdW materials, particularly the discovery of 2D vdW magnets, has provided new opportunities for the development of MTJs.

2.5.3 Magnetism in two-dimensional materials

The study of 2D magnetism can be traced back to a theoretical paper published by Onsager in 1944, which proved that a ferromagnet with a single-layer Ising model could possess long-range magnetic order.^{134,135} Due to the limitations of experimental equipment and technologies, 2D vdW magnetic materials were experimentally discovered late. Researchers tried to obtain 2D vdW magnetic materials by

introducing localized magnetic defects in graphene and TMDC.^{136,137} However, this approach is less appealing compared to the intrinsic magnetism in vdW materials. In 2017, Huang *et al.* and Gong *et al.* observed intrinsic ferromagnetism in vdW monolayer CrI₃ and vdW bilayer Cr₂Ge₂Te₆, respectively, triggering an upsurge in experimental research on 2D intrinsic magnetic materials (Figure 2.8).^{138,139}

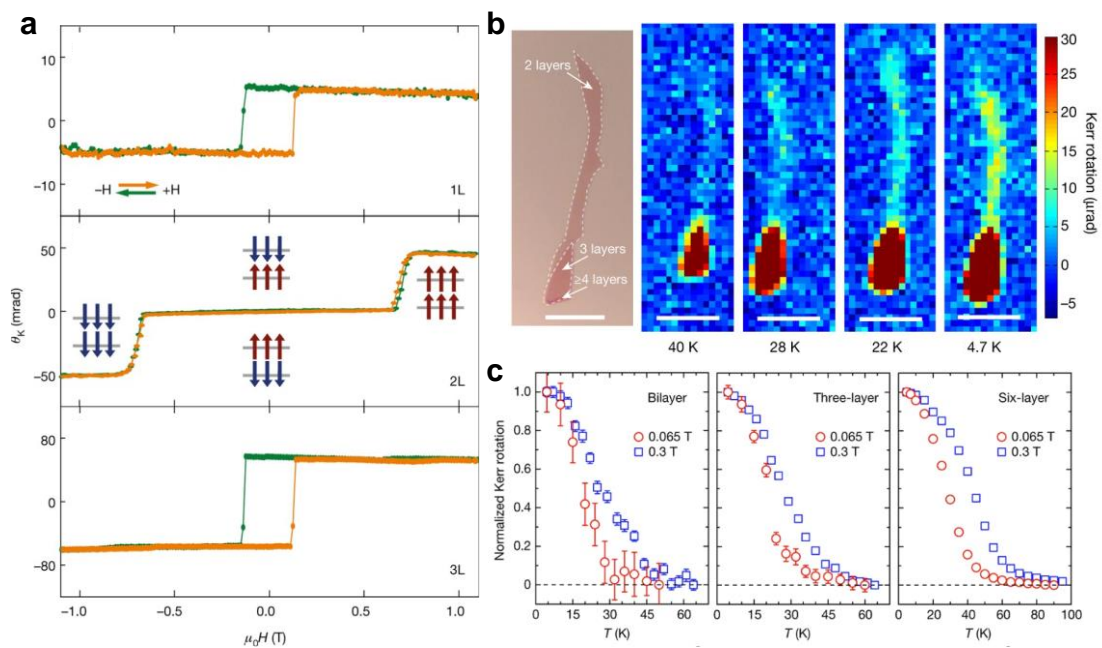
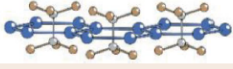
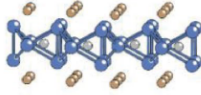
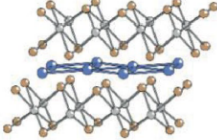
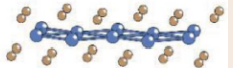
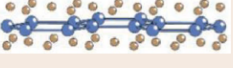


Figure 2.8 The discovery of 2D vdW magnetics CrI₃ and Cr₂Ge₂Te₆. (a) magneto-optic Kerr effect (MOKE) signal in monolayer (top), bilayer (middle), and trilayer (bottom) CrI₃ flakes, indicating ferromagnetic (1L), antiferromagnetic (2L), and ferromagnetic (3L) behaviours, respectively. (b) Optical image of exfoliated Cr₂Ge₂Te₆ atomic layers and Kerr rotation signals for the flakes at $B = 0.075$ T and different temperatures. Scale bar: 10 μm . (c) Normalized Kerr rotation angle as a function of temperature, at two different magnetic fields, 0.065 T (red circles) and 0.3 T (blue squares), for 2L (left), 3L (middle) and 6L (right) Cr₂Ge₂Te₆ flakes. The figure is reproduced from Ref.^{138,139}.

Different kinds of vdW magnetic materials have been discovered since then,
26

such as the out-of-plane ferromagnetic semiconductor CrBr_3 , the antiferromagnetic semiconductor CrCl_3 , the out-of-plane ferromagnetic metals Fe_3GeTe_2 and Fe_5GeTe_2 , the antiferromagnetic insulators XPS_3 ($X = \text{Fe}, \text{Ni}, \text{Mn}$), the antiferromagnetic topological insulator MnBi_2Te_4 .¹⁴⁰⁻¹⁴⁵ Also, room-temperature ferromagnetism was discovered in the metal VSe_2 grown on a MoS_2 substrate by molecular beam epitaxy (MBE).¹⁴⁶ Table 2.2 presents a selection of 2D vdW magnetic materials along with their physics properties.

Table 2.2 Magnetic properties and crystal structures of vdW magnets. The table is reproduced from Ref.¹⁴⁷.

Material	Magnetic Order	T_C/T_N (K)	Bandgap ^b (eV)	Additional notes	Crystal structure
FePS_3	AFM ⁺	118	1.6	Zigzag	
NiPS_3	AFM	148 ^a -166 ^b	1.7	Zigzag, slight tilt out-of-plane	
MnPS_3	AFM	78	3.0	Neél, isotropic	
CrGeTe_3	FM ⁺	<5 ^a -61 ^b	0.38		
Fe_3GeTe_2	FM ⁺	70 ^a -221 ^b	Metallic		
Fe_5GeTe_2	FM ⁺	270 ^a -310 ^b	Metallic		
MnBi_2Te_4	L-AFM ⁺	21	0.1	Intrinsic magnetic topological insulator L-AFM: intralayer FM, interlayer AFM	
VSe_2	FM ^{a,}	>300 ^a	Metallic	$T_{\text{CDW}} \sim 130$ K MBE-grown	
MnSe_x	FM ^{a,+}	>300 ^a	3.4	MBE-grown	
CrI_3	L-AFM ^{a,+} FM ^{b,+}	45 ^a -61 ^b	1.2		
CrBr_3	FM ⁺	20 ^a -37 ^b	2.2		
CrCl_3	L-AFM	17	3.0		

^aAtomically thin. ^bUnexfoliated bulk. ^{||}In-plane anisotropy. ⁺Out-of-plane anisotropy. FM, ferromagnet; AFM, antiferromagnet; L-AFM, layered antiferromagnet.

Unlike magnetic insulators and magnetic semiconductors, Fe_3GeTe_2 is one of the few vdW magnetic metals.¹⁴² Fe_3GeTe_2 has a space group $P6_3/mmc$ with lattice parameters $a = b = 3.991 \text{ \AA}$, $c = 16.33 \text{ \AA}$ (Figure 2.9a).¹⁴⁸ A single layer of Fe_3GeTe_2 consists of a Fe_3Ge sublattice with Te atoms on both sides of Fe_3Ge .¹⁴⁹ The Fe atoms

in the Fe_3Ge sublattice occupy two chemically distinct positions, which can be referred to as Fe^{I} and Fe^{II} . The $\text{Fe}^{\text{I}}\text{-Fe}^{\text{I}}$ dumbbells are located at the centre of every hexagonal plaquette in the honeycomb lattice, composed of covalently bonded Fe^{II} and Ge atoms.¹⁴⁹

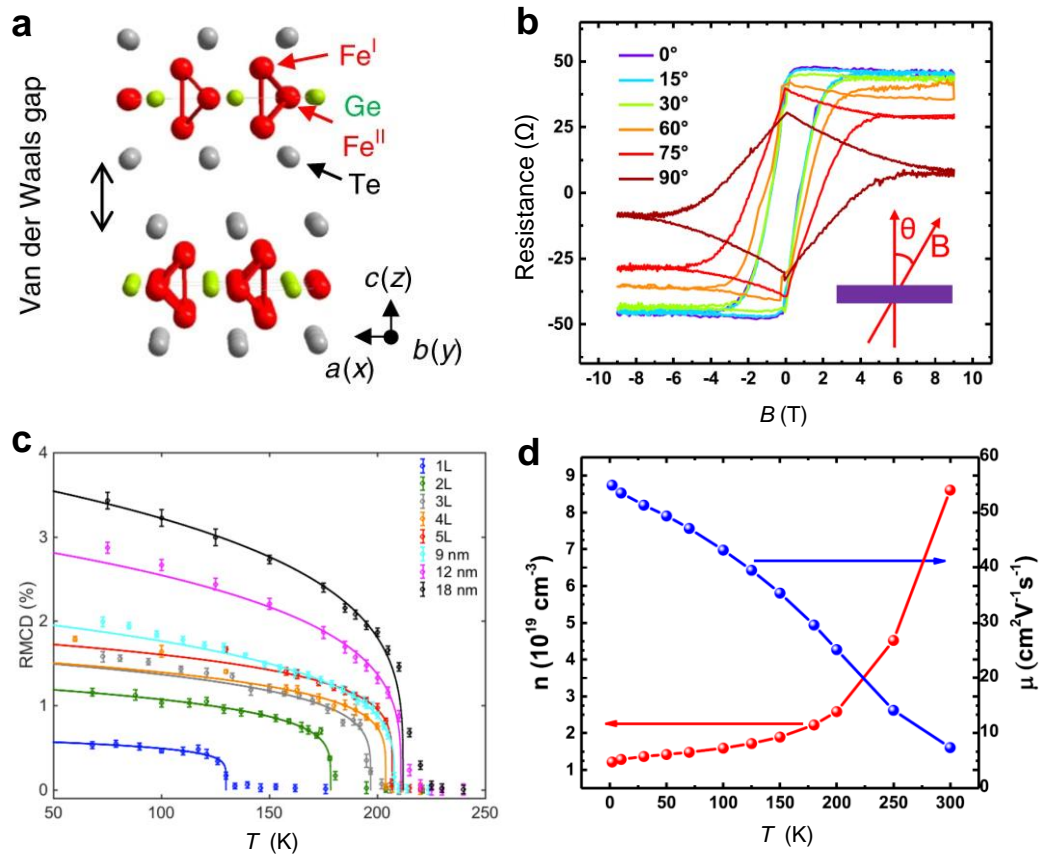


Figure 2.9 2D ferromagnet Fe_3GeTe_2 . (a) The crystal structure of the Fe_3GeTe_2 bilayer. (b) The angle-dependent anomalous Hall data of a Fe_3GeTe_2 Hall bar. The measurement geometry is displayed in the inset. (c) Reflective magnetic circular dichroism (RMCD) signal as a function of temperature for thin Fe_3GeTe_2 flakes. The error bars correspond to the standard deviation of the noise in the RMCD signal and the solid lines are least-squares criticality fits using the function $\alpha(1 - T/T_C)^\beta$. (d) Carrier density and mobility of Fe_3GeTe_2 at different temperatures. The figure is reproduced from Ref.^{142,149,150}.

In 2016, theoretical calculations suggested that Fe_3GeTe_2 has strong magnetic anisotropy and robust itinerant ferromagnetism.¹⁵¹ Later in 2018, Fei *et al.* and Deng *et al.* obtained few-layer Fe_3GeTe_2 flakes using a mechanical exfoliation method, independently.^{18,150} Fe_3GeTe_2 exhibits perpendicular magnetic anisotropy, which means that the easy axis of magnetization is along the c -axis (out-of-plane). As shown in Figure 2.9b, the coercive field increases simultaneously with the angle (θ) between the magnetic field (B) and the normal vector of the sample surface.¹⁴² The T_C of Fe_3GeTe_2 increases with the thickness of the material. For bulk crystalline, T_C is about 210 K, but drops to 130 K for the monolayer (Figure 2.9c).¹⁵⁰ Fe_3GeTe_2 can be grown by different methods, such as melting,¹⁵² chemical vapour transport (CVT),^{149,153,154} and molecular beam epitaxy (MBE).^{142,155} For bulk Fe_3GeTe_2 grown by MBE, the carrier concentration increases with increasing temperature and can achieve $9.0 \times 10^{19} \text{ cm}^{-3}$ at 300 K, while the mobility drops with increasing temperature ($7.3 \text{ cm}^2\text{V}^{-1}\text{s}^{-1}$ at room temperature, Figure 2.9d).¹⁴² Fe_3GeTe_2 is easily oxidized in air and the surface oxide layer forms antiferromagnetic coupling with Fe_3GeTe_2 and affects the magnetic hysteresis loop.¹⁵⁶

Fe_3GaTe_2 is another 2D vdW metallic ferromagnet, which was first grown by Zhang *et al.* via the self-flux method in 2022.¹³⁰ Similar to Fe_3GeTe_2 , Fe_3GaTe_2 also possesses a hexagonal $P6_3/mmc$ space group structure with lattice parameters $a = b = 3.9860 \text{ \AA}$ and $c = 16.2290 \text{ \AA}$. It is worth noting that Fe_3GaTe_2 is the first discovered 2D vdW intrinsic ferromagnets with a Curie temperature exceeding room temperature ($T_C > 350 \text{ K}$). At room temperature, Fe_3GaTe_2 exhibits a high saturation magnetic

moment (40.11 emu/g), large perpendicular magnetic anisotropy energy density ($\sim 4.79 \times 10^5 \text{ J/m}^3$), and large anomalous Hall angle (3%), which make Fe_3GaTe_2 a compelling candidate as a 2D ferromagnetic platform for advanced spintronic devices.¹³⁰ In our study, we employed few-layer Fe_3GaTe_2 as ferromagnetic electrodes to construct $\text{Fe}_3\text{GaTe}_2/\text{WSe}_2/\text{Fe}_3\text{GaTe}_2$ MTJs and demonstrated room-temperature magnetoresistance ($\sim 85\%$) in all-vdW systems for the first time.¹⁵⁷ This work is presented in Chapter 7.

Chapter 3

Sample fabrication

Two-dimensional (2D) layered materials can be combined into a virtually limitless number of van der Waals (vdW) heterostructures due to various degrees of freedom, such as the choice of materials, their stacking order and thickness, their lateral alignment, *etc.* This versatility makes them more adaptable than other conventional semiconductors. This chapter describes the fabrication techniques used to create the vdW heterostructures studied in the experiments.

To fabricate functional devices based on vdW heterostructures, we used different methods based on traditional fabrication processes and 2D material transfer technology. The fabrication of metal electrodes on SiO₂/Si substrates required the use of photolithography, electron beam lithography (EBL), and magnetron sputtering techniques. We also employed the polydimethylsiloxane-assisted (PDMS-assisted) deterministic transfer technique for the assembly of van der Waals layers. Also, a needle-assisted transfer method was utilized for the positioning of graphene microsheets.

3.1 Photolithography

Ultraviolet (UV) photolithography was used to fabricate metal electrodes on SiO₂/Si substrates. UV photolithography uses UV light to pattern the desired geometric structure on a photoresist in order to transfer the mask pattern onto the substrate through following steps, such as evaporation and etching. UV

photolithography finds wide applications in modern semiconductor technologies and has greatly promoted the development of the integrated circuit manufacturing industry.¹⁵⁸



Figure 3.1 G-25 precision mask aligner at the Institute of Semiconductors, Chinese Academy of Sciences.

UV photolithography involves three key elements: the mask aligner, the photoresist, and the mask. In the experiments conducted at the Institute of Semiconductors, Chinese Academy of Sciences, the G-25 precision mask aligner produced by Chengdu Xinnanguang Technology Co., Ltd. was used (Figure 3.1). The photoresist can be a positive or a negative resist. The positive resist becomes soluble in the developer solution after exposure, while the negative resist becomes insoluble. The positive resists used in our experiments include AZ6130 and S9200, while the negative resists include L-300 and 5200. The mask can be designed according to the corresponding pattern needed, with the patterns of positive and negative resists being complementary.

The main steps used in UV photolithography are as follows:

1. Substrate cleaning: Sequentially clean the substrate with acetone, anhydrous ethanol, and deionized water, followed by heating and drying to remove water on the substrate surface.

2. Spin-coating: Place the cleaned substrate on the spin coater's turntable, set the rotation speed and time, drop the photoresist on the substrate, and turn on the rotation switch.

3. Pre-baking: Place the substrate on the hot plate for baking. The baking temperature and time depend on the type of photoresist used. The purpose of pre-baking is to evaporate the solvent in the photoresist while improving the adhesion of the photoresist onto the substrate.

4. Exposure: Use a mercury lamp as the light source, and selectively expose the spin-coated substrate using UV light passing through the photomask. Under UV light, the photosensitive agent in the photoresist undergoes a photochemical reaction, and the positive resist undergoes a decomposition reaction that is soluble in the developer, while the negative resist undergoes a cross-linking reaction that is insoluble in the developer.

5. Developing: After exposure, place the substrate in the corresponding developer for developing. At this time, only the exposed part of the positive resist is dissolved, while the exposed part of the negative resist does not dissolve, so that the pattern corresponding to the photomask can be obtained.

6. Fixing: Place the developed substrate in the fixing solution to stop the

developing process and prevent over-developing from affecting the pattern accuracy.

After developing and fixing, the substrate can undergo subsequent processing steps, such as etching and metal evaporation. Finally, the remaining photoresist on the substrate is dissolved to obtain the desired structure.

3.2 Electron beam lithography

Electron beam lithography (EBL) is a micro-nano processing technology that uses an electron beam onto a sample coated with electron resist to expose the desired pattern. Similar to the photoresist used in photolithography, EBL also requires the use of the corresponding electron beam resist, which can be positive or negative. The positive resist undergoes a decomposition reaction when irradiated by the electron beam, making it soluble in the developer solution; while the negative resist undergoes crosslinking and curing reaction when irradiated by the electron beam, making it difficult to dissolve in the developer solution and thus retained.

EBL uses electron beams for lithography. According to de Broglie's matter wave theory, high-energy electrons correspond to waves of extremely short wavelengths, much smaller than the wavelengths of UV light used in photolithography. Therefore, compared with the UV photolithography process, EBL can achieve nanometer-scale exposure precision. Another significant advantage of electron-beam lithography is that it can directly write custom patterns. When using EBL, there is no need to prepare a specific mask, and any exposure pattern can be designed through a DesignCAD/KLayout software.

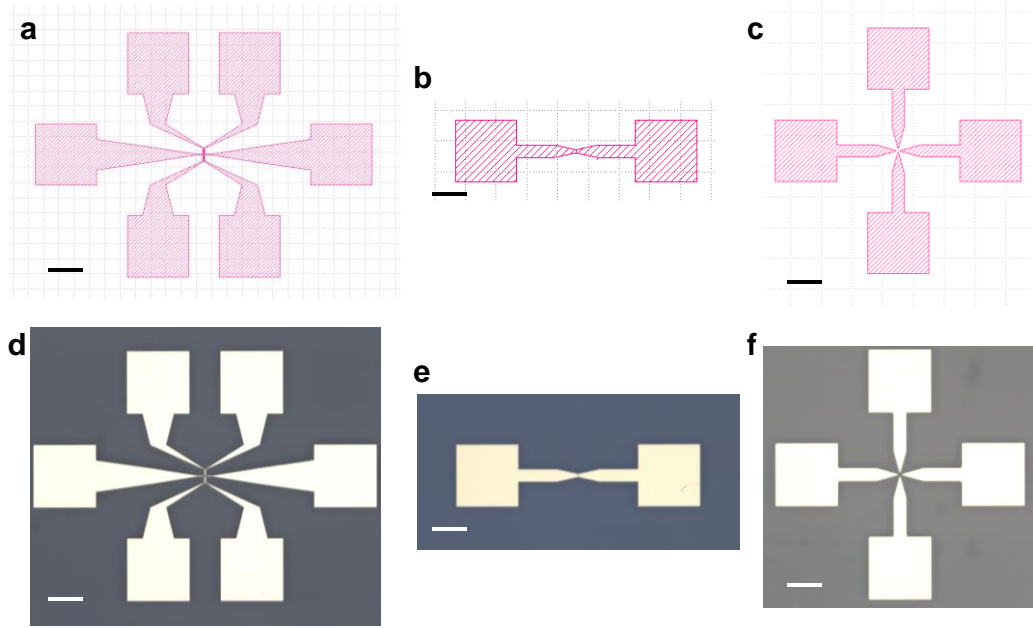


Figure 3.2 Examples of EBL devices fabricated at the University of Nottingham.

(a-c) Design of (a) Hall bar, (b) two-terminal, and (c) van der Pauw patterns using the KLayout software. Scale bar: 200 μm . (d-f) Optical images of the fabricated (d) Hall bar, (e) two-terminal, and (f) van der Pauw metal electrodes on SiO_2/Si substrates. Scale bar: 200 μm .

Although the precision of EBL is high and the exposure pattern is not limited, the EBL process is time-consuming, which reduces efficiency and is not conducive to the fabrication of large-scale or high-volume devices.

We used the Nanobeam nB5 EBL instrument at the Nanoscale and Microscale Research Centre (nmRC) in Nottingham to pattern metal contacts (Figure 3.2) and CVD-grown graphene samples. At the Institute of Semiconductors, Chinese Academy of Sciences, the EBL system consists of a scanning electron microscope (SEM) and a nanometer pattern generation system (Figure 3.3). The SEM is the JSM-6510 electron microscope manufactured by Japan Electron Optics Laboratory Company (JEOL). To fabricate the four-terminal electrodes in Fe_3GaTe_2 Hall devices, we used the EBL

system shown in Figure 3.3 and utilized the electron beam positive resist polymethyl methacrylate (PMMA).

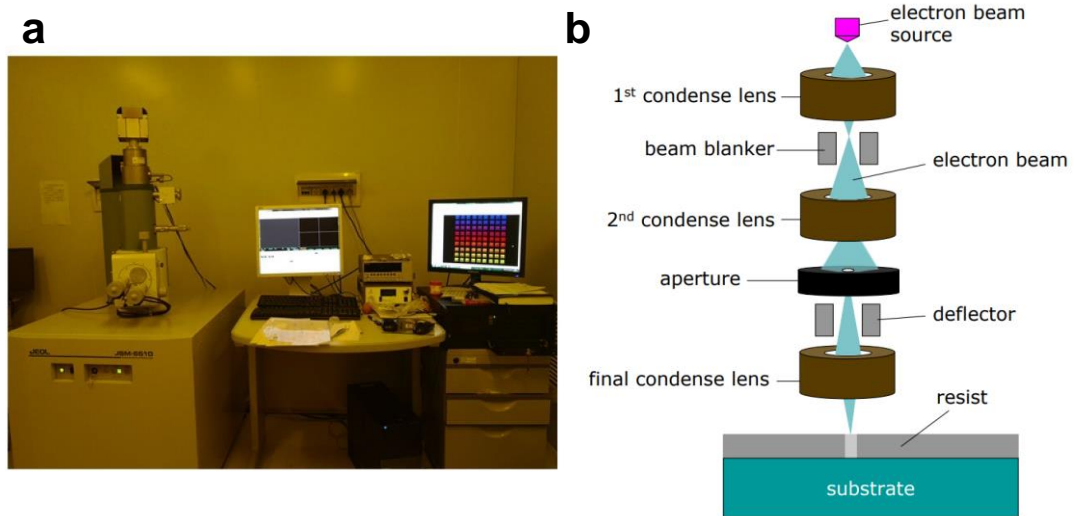


Figure 3.3 EBL system at the Institute of Semiconductors, Chinese Academy of Sciences. (a) The EBL system used in our experiments, including the SEM module and the nanometer pattern generation system module. (b) Schematic diagram of the EBL system. The figure is reproduced from Ref.¹⁵⁹.

3.3 Magnetron sputtering

Magnetron sputtering is a physical vapour deposition (PVD) technique that we used to deposit metal thin films, such as Au/Ti (thickness 50 nm/5 nm) electrodes on SiO₂/Si substrates. Under the electric field, electrons collide with argon atoms and ionize them, producing Ar⁺ ions and “secondary” electrons. The Ar⁺ ions are accelerated by the electric field towards the cathode target and bombard the target surface with high energy, causing the target material particles to sputter. Neutral target atoms or molecules then deposit on the substrate to form a thin film. Figure 3.4 shows the magnetron sputtering equipment manufactured by Syskey Technology Co., Ltd.. This was used at the Institute of Semiconductors, Chinese Academy of Sciences.



Figure 3.4 Magnetron sputtering equipment.

3.4 Mechanical exfoliation of vdW crystals

We use the mechanical exfoliation technique to isolate thin flakes of 2D vdW crystals from their bulk counterparts. In this process, a bulk vdW crystal is placed on adhesive tape, which is then folded and unfolded. The process is repeated multiple times until thin flakes with only a few atomic layers are obtained (Figure 3.5a). The tape is then pressed against a piece of PDMS film, smoothed, and peeled off rapidly. As a result, a thin flake is then transferred to the PDMS film (Figure 3.5b).

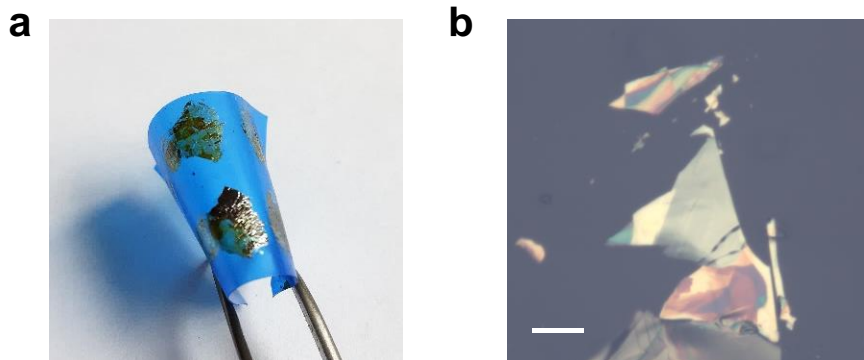


Figure 3.5 Mechanical exfoliation of vdW α -In₂Se₃. (a) α -In₂Se₃ stamped on adhesive tape. (b) Optical image of α -In₂Se₃ flakes on PDMS film. Scale bar: 10 μ m.

Mechanical exfoliation is a relatively simple and inexpensive technique that enables the production of high-quality, atomically thin flakes of vdW crystals. These thin flakes can be used to fabricate devices for electrical and optical studies. For this PhD thesis, a few-layer α -In₂Se₃, ϵ -GaSe, WSe₂, hBN, and Fe₃GaTe₂ nanosheets were mechanically exfoliated from their bulk counterparts. The high-quality bulk α -In₂Se₃ and ϵ -GaSe crystals were grown by the Bridgman method at the Institute for Problems of Materials Science, National Academy of Sciences of Ukraine by Professor Z. D. Kovalyuk and Dr Z. R. Kudrynskyi.^{60,160} The bulk single-crystal WSe₂ and hBN were purchased from HQ Graphene, and the bulk Fe₃GaTe₂ material was grown by the self-flux methods at Huazhong University of Science and Technology, China by Prof. Haixin Chang.¹³⁰

3.5 Deterministic transfer of vdW flakes to make heterostructures

We used a PDMS-assisted transfer method to assemble vdW heterostructures. A deterministic all-dry transfer set-up based on the technique detailed by Castellanos-Gomez *et al.*¹⁶¹ was used to control the position and alignment of the exfoliated vdW nanosheets. Figure 3.6a illustrates the core part of the deterministic transfer setup, the glass slide with the PDMS/In₂Se₃ film loaded onto a micromanipulator and a pre-patterned Si-substrate fixed on top of a copper plate by a double-sided tape. After the Si-substrate and the In₂Se₃ flake on the glass slide are aligned in the xy-plane, the In₂Se₃ flake is brought into contact with the substrate very slowly by adjusting the z-micrometer. The copper block on the stage can also be

rotated to aid the alignment. While monitoring the optical microscopic image on the computer screen continuously, the z-micrometer is then adjusted to peel off the PDMS from the substrate, which completes the transfer of the In_2Se_3 flake from the PDMS onto the SiO_2/Si substrate. Figure 3.6b shows In_2Se_3 flakes on top of PDMS, and Figures 3.6c-d show the same In_2Se_3 flakes on top of a pre-patterned SiO_2/Si -substrate after the dry transfer procedure described above.

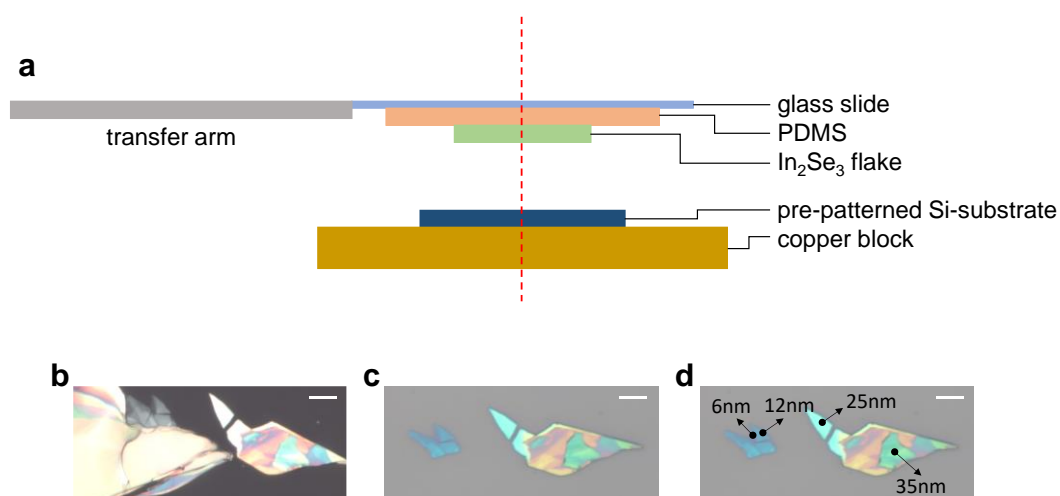


Figure 3.6 Deterministic transfer of In_2Se_3 flakes. (a) Diagram of the deterministic transfer setup. The target substrate is placed on a copper plate mounted on a motor-driven xy-stage, which can be controlled through a software. The exfoliated flakes on PDMS are attached on a microscope glass slide fixed with a transfer arm, which can be manually controlled to move in the x, y, z direction. (b) Image of In_2Se_3 flakes on PDMS. (c) Image of the same In_2Se_3 flakes after transfer onto a Si substrate with a 285 nm-thick SiO_2 layer. (d) Image of the same In_2Se_3 flakes with indicators of thickness, as derived from atomic force microscopy (AFM) studies. Scale bar: 10 μm .

3.6 Needle-assisted transfer of graphene microsheets

Adapted from Bie *et al.*,¹⁶² we have developed a site-specific transfer technique for individual graphene microsheets onto arbitrary substrates. The steps of the

needle-assisted transfer of graphene microsheets are briefly illustrated in Figure 3.7.

In this method, thousands of graphene microsheets with a lateral dimension of $10\ \mu\text{m} \times 40\ \mu\text{m}$ are fabricated by EBL using CVD-grown graphene on a 300 nm thick SiO_2 on Si substrate. After the EBL processing, the PMMA/graphene stack on SiO_2/Si undergoes etching in a solution composed of Buffered Oxide Etch (BOE) and Hydrofluoric acid (HF) at a 5:2 ratio. Within a few minutes, the PMMA/graphene film starts floating on the surface of the etching solution, while the Si substrate sinks to the bottom. We then use a plastic boat to pick up the PMMA/graphene film and transfer it into DI water. The film is washed several times with DI water, following which a copper grid is used to carefully pick it up. After drying in an inert atmosphere overnight, the PMMA/graphene film is ready to use.

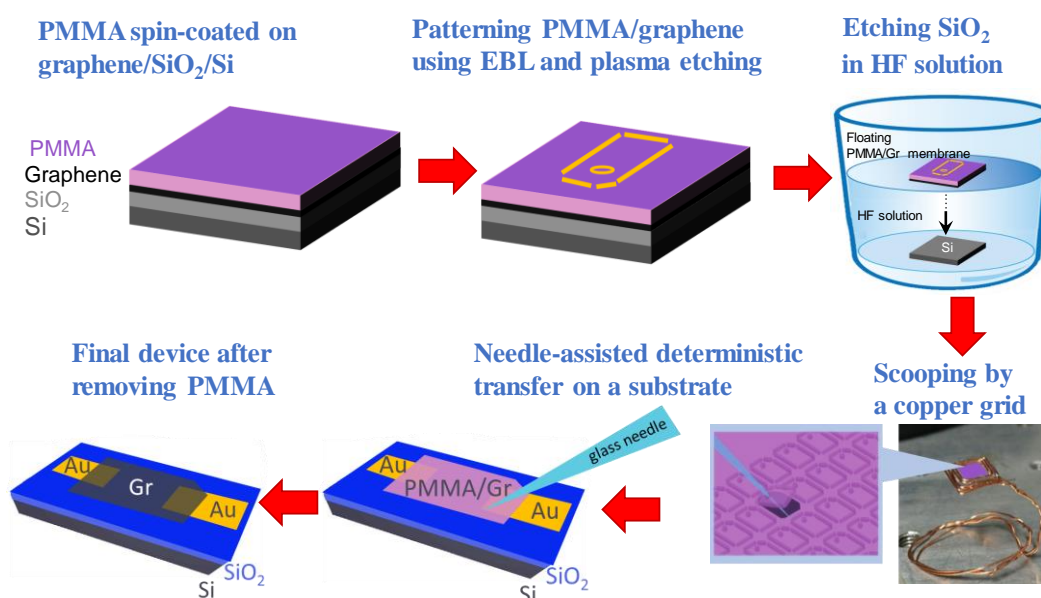


Figure 3.7 Needle-assisted transfer of graphene. Schematic illustration of the needle-assisted transfer process of patterned graphene microsheets. The figure is reproduced from Ref.¹⁶³.

We can transfer individual graphene microsheets onto a target substrate deterministically from the PMMA/graphene film. The copper grid containing the PMMA/graphene microsheets is fixed to the copper block in the transfer set-up, as described in Section 3.5. A glass fibre with a tip diameter of ~ 500 nm is attached to the transfer arm of the set-up. With the help of three-axis micromanipulators (x, y, z), the needle tip is carefully placed on one corner of the microsheet, which is then separated from the base membrane and attached to the needle for transfer onto a pre-patterned substrate. Following a successful transfer, the substrate with the graphene microsheet is heated at 120 °C for 30 minutes on a hot plate, and then immersed in acetone for 30 minutes to remove the PMMA.

Chapter 4

Characterization techniques

This chapter describes the advanced characterization techniques used to study the vdW materials and devices investigated in the thesis. Atomic force microscopy (AFM) and piezoresponse force microscopy (PFM) were used to examine the surface topography, layer thickness, and ferroelectric properties. To examine optical and vibrational properties, micro-photoluminescence (μ -PL) and micro-Raman (μ -Raman) were used. The equipment for measuring electrical, magnetic and optoelectronic transports of devices based on 2D layered materials and their heterostructures are also presented.

4.1 Atomic force microscopy and piezoresponse force microscopy

Atomic force microscopy (AFM) can operate in vacuum, atmosphere, or even liquid, and can detect the surfaces of conductors, semiconductors, and insulators, making it an important tool for studying the surface morphology of nanomaterials.

Figure 4.1a shows the AFM system used at the Institute of Semiconductors, Chinese Academy of Sciences, which is manufactured by Bruker Co., Ltd. The AFM system includes a vibration isolation platform, scanning tube, sample stage, microscope, controller, and computer. A graphical representation of the operating mechanism of the AFM can be seen in Figure 4.1b. The AFM detects the extremely weak interatomic forces between the sample and the probe to study the surface topography. For example, in order to obtain the topography, the scanning tube controls

the probe tip to move within a range close enough to the sample surface, detecting the interaction between the tip and the sample, which is called the detector signal. In order to relate the detector signal to the actual distance, a setpoint needs to be set in advance. When the scanning tube moves the probe into the imaging area, the system detects the detector signal and compares it with the setpoint. When they are equal, the scanning process begins. The scanning tube controls the probe to move accurately along the pre-set trajectory on the sample surface. When the probe encounters a change in the surface morphology, the interaction between the probe and the sample changes, resulting in a change in the detector signal. This difference between the detector signal and the setpoint is called the error signal. The z-axis feedback continuously compares the detector signal with the setpoint. If they are not equal, the height of the probe support is then adjusted so that the deflection is restored to the setpoint. At the same time, the software system uses the feedback signal to generate the scanning image, which equals the sample surface topography.

AFM can be carried out via several scanning methods, such as the contact mode and tapping mode. The contact mode maintains a constant setpoint while the tip and sample interact with each other. This can generate a significant lateral force on the sample, which may cause damage or displacement of loosely bound materials. On the other hand, in the tapping mode, the tip oscillates at a resonance frequency close to the sample surface. The feedback electronics control the amplitude or phase of the oscillating cantilever to regulate the tip-sample distance.

In this thesis, AFM was used to measure the thickness and surface morphology

of the exfoliated In_2Se_3 , GaSe, Fe_3GeTe_2 , and hBN layers. Different AFM set-ups were used, including MultiMode 8-HR AFM system (manufactured by Bruker) at the Institute of Semiconductors, Chinese Academy of Sciences and MFP-3D AFM system (manufactured by Oxford Instruments) at the University of Nottingham.

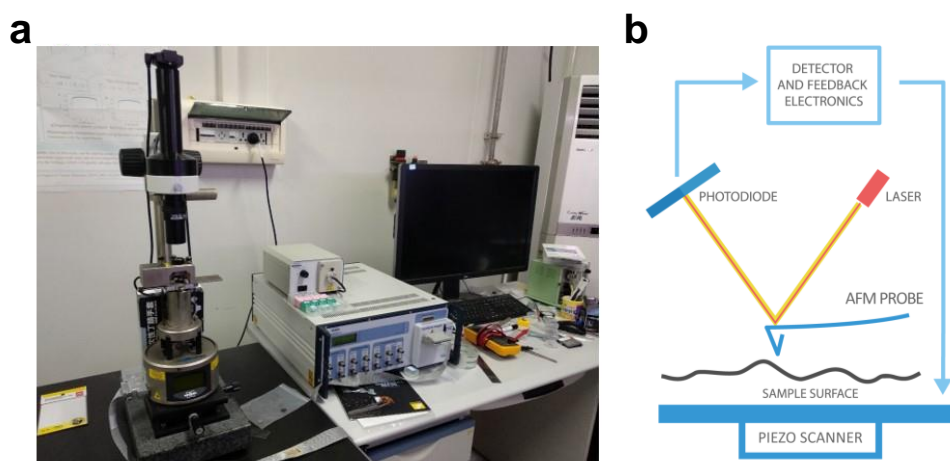


Figure 4.1 AFM. (a) Bruker MultiMode 8-HR AFM system at the Institute of Semiconductors, Chinese Academy of Sciences. (b) A schematic diagram of AFM.

Piezoresponse force microscopy (PFM) is a variant of AFM that allows the imaging and manipulation of piezoelectric/ferroelectric domains. This is achieved by bringing a sharp conductive probe into contact with a ferroelectric surface and applying an AC bias to the probe tip in order to excite a deformation of the sample through the converse piezoelectric effect. The resulting deflection of the probe cantilever is detected through a standard split photodiode detector method and then demodulated by the use of a lock-in amplifier. The experimental setup for PFM is shown in Figure 4.2. The left side of the scheme depicts a standard AFM setup. On the right side, the additional components for PFM operation are shown. In this way,

topography and ferroelectric domains can be imaged simultaneously with high spatial resolution.^{164,165}

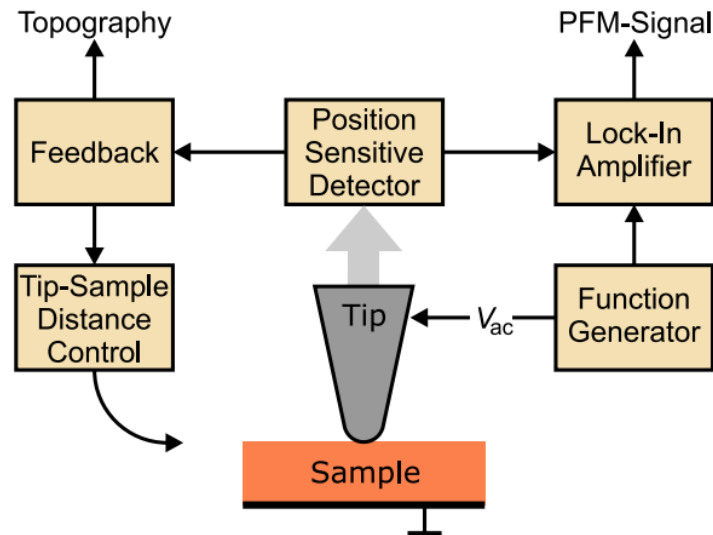


Figure 4.2 PFM. The left part illustrates a typical AFM configuration, while the right part exhibits the supplementary elements required for PFM functionality. The figure is reproduced from Ref.¹⁶⁶.

In the experiments, PFM was used to probe the intrinsic ferroelectric polarization of α -In₂Se₃, which was conducted by Dr Wenjing Yan (Nottingham Research Fellow) at the laboratory of Professor Oleg Kolosov at Lancaster University.

4.2 Micro-photoluminescence and Raman spectroscopy

Micro-photoluminescence (μ -PL) is an essential measurement technique to investigate optical transitions in semiconductors. Electron-hole pairs are generated when the sample is excited by a light source with photon energy greater than the bandgap. These electron-hole pairs can recombine via various available paths. For intrinsic semiconductors, which have no energy levels inside the forbidden bandgap,

electrons and holes recombine from the bottom edge of the conduction band and the top of the valence band, respectively.¹⁶⁷ This transition can generate photons with an energy $h\nu$ equal to the bandgap of the material E_g . Due to defects and impurities, new energy states appear in the forbidden gap, resulting in additional optical transitions at an energy $h\nu$ smaller than E_g (as shown in Figure 4.3). The intensity of each transition versus energy $h\nu$ represents the PL spectrum.¹⁶⁸ This simple picture does not include other important phenomena, such as electron-hole Coulomb interactions leading to excitonic emissions.

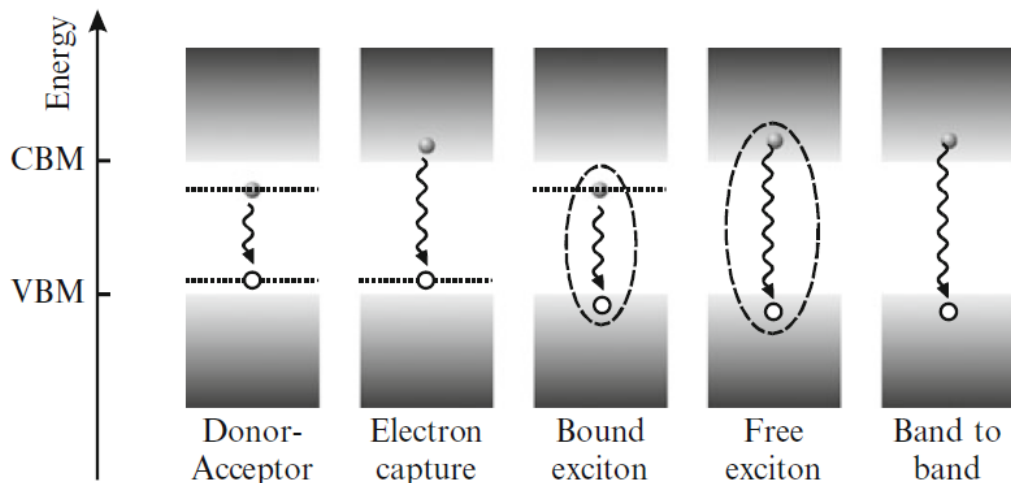


Figure 4.3 PL recombination processes. Schematics of the carrier recombination processes in PL for donor-acceptor, electron capture onto an acceptor, bound exciton, free exciton and band to band transitions. The shaded areas indicate the valence band and the conduction band, while the horizontal dotted lines mark the energy position of impurity states. Electrons (holes) are indicated by dark-shaded (hollow) dots. Undulated arrows indicate radiative recombination. Dashed curves highlight the Coulomb interaction. The figure is reproduced from Ref.¹⁶⁸.

Raman spectroscopy relies upon the inelastic scattering of photons, namely

Raman scattering. The laser light interacts with molecular vibrations, phonons or other excitations in the system, resulting in a change in the energy of the scattered photons. The shift in energy gives information about the vibrational modes in the system.¹⁶⁸

μ -PL and Raman spectroscopy measurements were conducted at the University of Nottingham using a LabRAM HR-UV spectrometer equipped with a confocal microscope, excitation laser optics and a XYZ motorized stage. The samples were mounted on the XYZ motorized stage and excited either by a He-Ne ($\lambda = 633$ nm) or frequency doubled Nd:YVO4 ($\lambda = 532$ nm) laser. The laser beam was focused by an objective of a focal length of 1.8 mm and numerical aperture of 0.9 with 100 \times optical magnification. The μ -PL and Raman signals were dispersed by a grating of either 150 g/mm or 1200 g/mm depending on the required wavelength range and spectral resolution, and were detected by a Si charge coupled device (CCD) (detection range from $\lambda = 350$ nm to 1100 nm).

4.3 Electrical transport

For the transport studies conducted at the Institute of Semiconductors, Chinese Academy of Sciences, we used the Model CRX-VF cryogenic probe station system manufactured by Lake Shore Cryotronics Co., Ltd (Figure 4.4). This system enables electrical transport studies with a magnetic field up to ± 2.5 T over the temperature range from 8 K to 500 K.

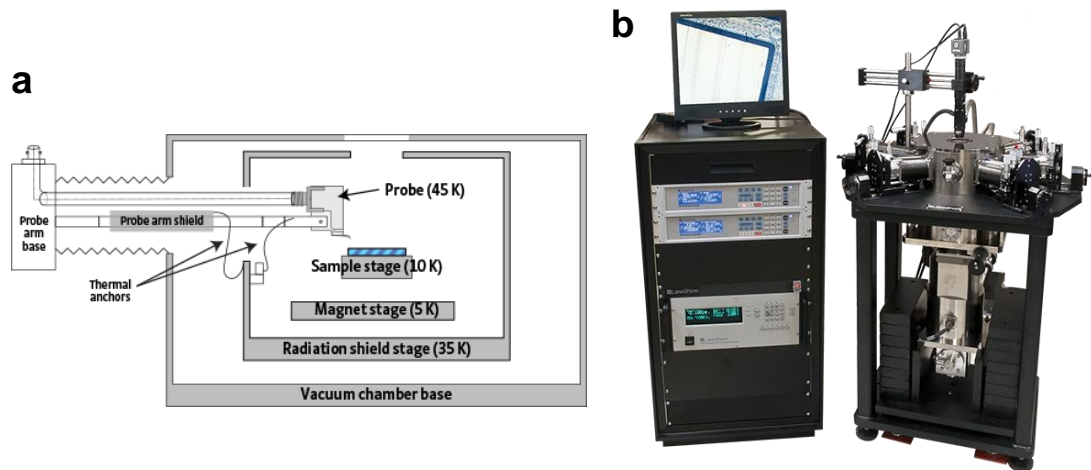


Figure 4.4 The cryogenic probe station system. (a) Schematics of the core part of the cryogenic probe station system at the Institute of Semiconductors, Chinese Academy of Sciences. (b) Image of the cryogenic probe station system.

The cryogenic probe station system includes a probe station, a cryogenic system, a superconducting magnet, a vacuum system, an imaging system, and external measurement instruments. The probe station contains six probe arms that can move in three directions, including four ordinary metal probe arms and two microwave probe arms. The cryogenic system consists of a liquid helium circulation compressor and two Lake Shore Model 336 temperature controllers, which can be adjusted within a temperature range of 8 K to 500 K. The superconducting magnet generates a magnetic field perpendicular to the sample surface, with a maximum value of ± 2.5 T. The vacuum system consists of a mechanical pump and a molecular pump, which can achieve a high vacuum of 1×10^{-6} mbar. The sample stage can be observed by an imaging system, which comprises a CCD camera with adjustable magnification and focus, providing a spatial in plane resolution of about 5 μm . With the help of the imaging system, the probe can be easily moved and lowered until it contacts the

electrodes on the substrate. The external measurement instruments consist of a Keithley 2602B source meter and a Keithley 2182A voltmeter. The Agilent Technology B1500A Semiconductor Analyzer can also be used for current–voltage I – V measurements with high precision and low noise. By combining the above components and using LabView software, the electrical transport properties of samples can be conveniently tested under different temperatures, magnetic fields, and voltages/currents.

In Nottingham, a Keithley 2400 source meter was used to measure the current–voltage characteristics of two terminal devices. For the source-drain current I_{SD} –gate voltage V_G measurements, the V_G was applied by an additional Keithley 2400 DC voltage source, which was also used to measure the gate leakage current (I_G) of the devices. The LabView software was used to control source meters and record experimental data. For low-temperature measurements, the sample was positioned in a cryostat linked to a liquid N₂ container while a temperature controller from Lake Shore Cryotronics Co., Ltd was used to control and probe the temperature (range from 100 K to 400 K). All transport measurements were conducted in a vacuum environment ($\sim 10^{-6}$ mbar).

4.4 Photocurrent studies

At the Institute of Semiconductors, Chinese Academy of Sciences, photocurrent measurements were acquired using an Agilent Technology B1500A Semiconductor Analyzer and a lock-in amplifier (SR830) with a light chopper. The continuous

spectrum from near-infrared to visible and UV range monochromatic illumination was provided by a Fianium WhiteLase Supercontinuum Laser Source and a Xe lamp, respectively. The output laser wavelength was tuned by an Omni- λ 300 monochromator.

In Nottingham, unfocused laser beams of wavelength $\lambda = 405$ nm and $\lambda = 633$ nm were used for the photocurrent measurements. The temporal dynamics of the photocurrent was investigated under constant bias voltage and illumination by a mechanically modulated He-Ne laser with wavelength $\lambda = 633$ nm and frequency $f < 200$ Hz. The photocurrent signal was measured using a Tektronix DPO 4032 digital oscilloscope and a Keithley 2400 was used as a DC voltage source. The device was connected in series with a $1 \text{ M}\Omega$ resistor and the voltage on the $1 \text{ M}\Omega$ resistor was recorded using the oscilloscope with high time resolution (analog bandwidth ~ 350 MHz). To generate photocurrent maps, the device was mounted inside a vacuum cryostat ($\sim 10^{-6}$ mbar) and positioned on a motorized stage with micrometre spatial precision. A confocal microscope system with a focal point diameter of around $1 \text{ }\mu\text{m}$ was employed to focus the laser beam ($\lambda = 405$ nm and power up to 1 mW) onto the sample. The Keithley 2400 voltage source was connected to the device. The motorized stage moves the laser beam over the device's surface so that the resulting spatial maps of photocurrent are captured, highlighting the areas sensitive to light.

Chapter 5

Van der Waals ferroelectric semiconductor junctions

This chapter reports the electronic and optoelectronic properties of ferroelectric semiconductor junctions (FSJs) in which the ferroelectric van der Waals semiconductor α -In₂Se₃ is embedded between two single-layer graphene electrodes. In these two-terminal devices, the ferroelectric polarization of the nanometre-thick α -In₂Se₃ layer modulates the transmission of electrons across the graphene/In₂Se₃ interface, leading to memristive effects that are controlled by applied voltages and/or by light. The underlying mechanisms of conduction are examined over a range of temperatures and under light excitation revealing thermionic injection, tunnelling and trap-assisted transport.

The α -In₂Se₃ bulk crystals were grown by Dr Zakhar Kudrynskyi and Prof. Zakhar Kovalyuk at The National Academy of Sciences of Ukraine. The exfoliated layers and devices were fabricated by myself, Dr Zakhar Kudrynskyi and Dr Nilanthi Balakrishnan. Transport measurements, optical studies and optoelectronics experiments were conducted by myself. Dr Eli Castanon, Prof. Oleg Kolosov and Dr Wenjing Yan conducted piezoresponse force microscopy (PFM) studies at Lancaster University. The results presented in this chapter were published in *2D Materials* **8**, 045020 (2021).

5.1 Introduction

Amongst 2D ferroelectrics, the vdW semiconductor α -In₂Se₃ has emerged as a promising material due to its room temperature in-plane (IP) and out-of-plane (OOP) ferroelectricity^{80,89,108,113} and low coercive electric field^{12,113} ($\sim 10^7$ V m⁻¹). Its use in 2D ferroelectric devices has been reported and includes ferroelectric field effect transistors (FeFETs) with the ferroelectric semiconductor serving as conducting channel^{97,99,120,122,169,170} or dielectric gate^{109,119,171}, and ferroelectric semiconductor junctions (FSJs) based on a thin α -In₂Se₃ layer embedded between single-layer graphene and few layer graphene electrodes.¹¹³ The geometry of the FSJ is well suited to miniaturization and low-power applications. Furthermore, the conductivity properties of a ferroelectric semiconductor can be modified by temperature and light, providing broad prospects for applications of ferroelectric devices.

Here, we report on FSJs based on the ferroelectric vdW semiconductor α -In₂Se₃ embedded between two single-layer graphene electrodes. In the FSJ, the polarization of the nanometer-thick In₂Se₃ layer is controlled by a voltage applied between two graphene electrodes, thus modifying the Schottky-like barrier at the graphene/In₂Se₃ interface: the change in the height of the barrier modulates the transmission of electrons across the interface, leading to memristive effects.¹¹³ We show that this is a robust process over a wide range of temperatures, below and above room temperature. Also, it can be modified by a relatively small applied voltage (~ 1 V) and by light: The free carriers generated by light and/or thermionic injection can neutralize the

polarization charges at the graphene/ α -In₂Se₃ interface and influence the hysteretic behaviour in the electrical transport, offering opportunities for future developments.

5.2 Characterization studies of α -In₂Se₃

For our studies we focus on the α -phase of In₂Se₃, which is ferroelectric at room temperature with a Curie temperature T_C above 500 K.^{13,108} Amongst the different crystalline phases of In₂Se₃, the α -phase exhibits either a rhombohedral (3R) or a hexagonal (2H) crystal structure.^{107,172} For both structures, the single vdW In₂Se₃ layer consists of five atomic layers stacked in the sequence Se–In–Se–In–Se (1 quintuplet layer, QL) that exhibits reversible spontaneous electric polarization in both OOP and IP orientations.^{14,108,113} The asymmetric position of the Se-atoms inside each QL breaks the centro-symmetry of the crystal, providing two degenerate energy states with opposite OOP polarization and in-plane asymmetry. To reverse the OOP polarization, the middle Se-atom must move along the c -axis and in the ab -plane, leading to a break up and reconfiguration of the In-Se covalent bond.^{89,99,108}

Figure 5.1a shows the room temperature ($T = 300$ K) micro-Raman spectra of an α -In₂Se₃ film ($t = 200$ nm) embedded between two graphene electrodes. The positions of the Raman lines do not change with the applied voltage and coincide with those reported in the literature for 2H α -In₂Se₃.^{107,172,173} In the Raman spectra, the A_1 and A'_1 modes correspond to the vibration in the OOP direction, and the E_g mode corresponds to the IP vibration (Figure 5.1b).¹⁷⁴ The photoluminescence (PL) emission ($T = 300$ K) for bulk α -In₂Se₃ ($t = 200$ nm) is shown in Figure 5.1c.

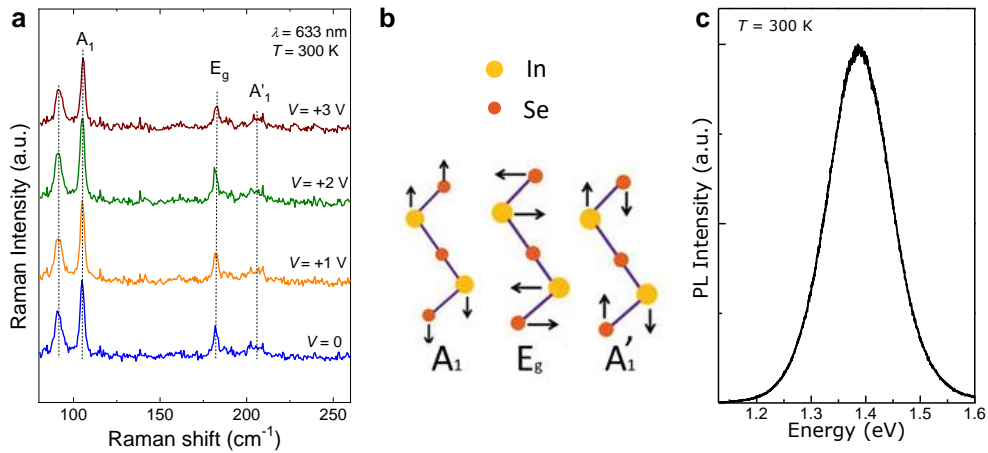


Figure 5.1 Raman and PL characterizations of α -In₂Se₃. (a) Room temperature ($T = 300$ K) micro-Raman spectra for α -In₂Se₃ ($t = 200$ nm) embedded between two graphene electrodes at different biases. The spectra are acquired with laser light of wavelength $\lambda = 633$ nm and power $P_i \sim 10^{-6}$ W. (b) Atomic displacements of In₂Se₃ vibrational modes. The figure is reproduced from Ref.¹⁷⁴. (c) Representative PL spectrum for bulk α -In₂Se₃ ($T = 300$ K).

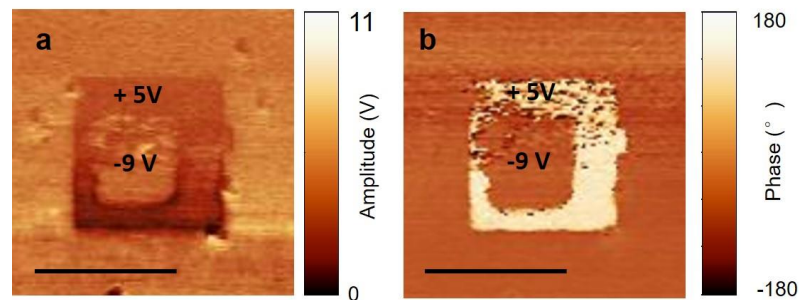


Figure 5.2 PFM measurements of α -In₂Se₃. PFM amplitude (a) and phase (b) images of a 36 nm thick α -In₂Se₃ flake on a Si-substrate. The large square shows the PFM amplitude and phase contrast of an area of the flake after a +5 V electric poling. The signals for the small square show that the polarization can be switched back using an applied voltage with opposite polarity (-9 V). Scale bar: 1 μ m.

PFM measurements of α -In₂Se₃ films were conducted using a commercial scanning probe microscope in ambient atmosphere. Figure 5.2 shows the PFM images of a 36 nm thick α -In₂Se₃ flake on a Si-substrate. DC bias voltages between the tip

and the sample surface were applied to switch the polarization of ferroelectric domains. The large square shows the PFM amplitude and phase contrast of an area of the flake after a +5 V electric poling. The amplitude and phase signal within the small square show that the polarization can be switched back using a voltage with opposite polarity (-9 V), suggesting an OOP ferroelectric polarization.

5.3 Ferroelectric semiconductor junctions in the dark

5.3.1 Transport characteristics

The OOP polarization of α -In₂Se₃ is important for the miniaturization of electrical components that require vertical device architectures, such as the FSJ. Our graphene/In₂Se₃/graphene vdW heterostructures are assembled by exfoliation and mechanical stamping of nanometer-thick vdW layers (see Chapter 3 Sample fabrication). The optical image and schematics of the band alignments for a FSJ with a 30-nm-thick α -In₂Se₃ layer are illustrated in Figures 5.3a and 5.3b. Under a voltage applied between the two graphene electrodes of the FSJ, electrons are injected from the negatively biased graphene electrode onto the α -In₂Se₃ layer and collected at the second graphene electrode (Figure 5.3a). For an electric field larger than the coercive field, the ferroelectric layer becomes polarized and the polarized charges at the graphene/ α -In₂Se₃ interface shift the Dirac cone of graphene relative to the conduction band (CB) of α -In₂Se₃, thus lowering (Figure 5.3bi) or increasing (Figure 5.3bii) the potential barrier seen by electrons. The polarization charges decrease the potential barrier at one interface, while they increase it at the other interface. Also, the applied

voltage creates an asymmetry in the junction so that the interface between the negatively biased graphene electrode and the α -In₂Se₃ barrier dominates: once electrons are injected across the first interface, they travel throughout the ferroelectric layer reaching the second interface with graphene where there are available empty states (Figure 5.3a). For an electric field larger than the coercive field, the potential barrier seen by the electrons at the first interface decreases. This leads to increased transmission of electrons throughout the device, causing resistance switching and memristive behaviours.

The current–voltage $|I|$ – V curves of the FSJ reveal counter-clockwise loops at $T = 100$ K (Figure 5.3c) and $T = 300$ K (Figure 5.3d): the amplitude of the current is larger when sweeping the voltage from high to low positive V (or from high to low negative V). The applied voltage is critical to the observation of the hysteretic behaviour in I – V . As shown in Figure 5.3e, the counter-clockwise loop becomes more pronounced at larger V . Weaker clockwise loops are instead observed at low V . For the device of Figure 5.3, a voltage $|V| = 1$ V corresponds to an electric field $E = |V|/t > 0.3 \times 10^8$ V/m, where $t \approx 30$ nm is the thickness of the α -In₂Se₃ layer.

The transport properties of the FSJ are further probed by monitoring the temporal dependence of the current under different applied voltages and electric poling conditions of the FSJ. The current measured at a low bias ($V = +0.5$ V) takes different values following a poling of the FSJ at a larger positive or negative voltage (see Figure 5.3f for poling at $V = +1.5$ V). The initial resistive state can be resumed by applying a negative (or positive) bias after poling at $V > 0$ (or $V < 0$) (Figure 5.3f).

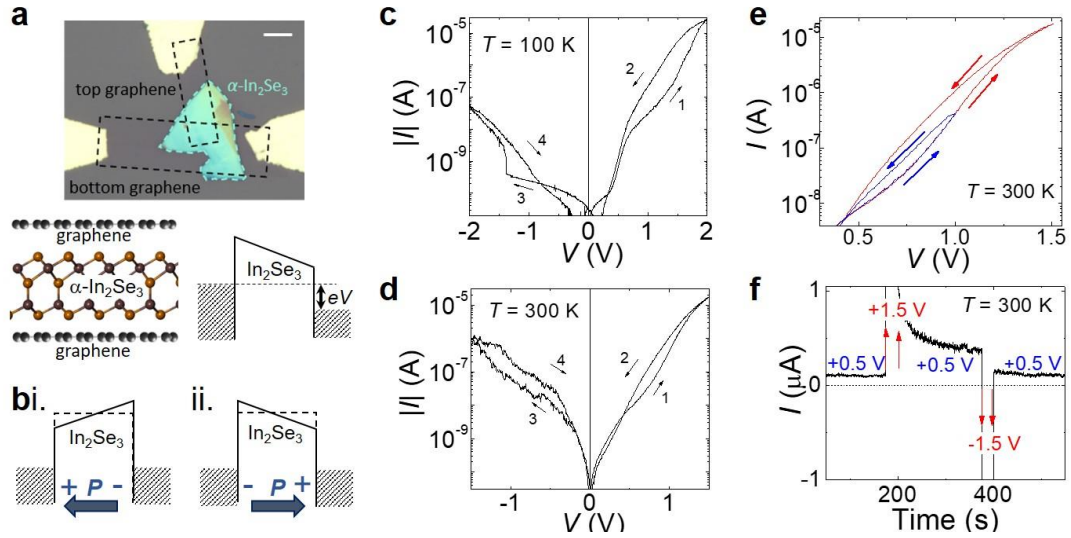


Figure 5.3 Ferroelectric semiconductor junction, FSJ. (a) Optical image (top) and schematics (bottom) of the graphene/In₂Se₃/graphene junction and its band diagram. Scale bar: 5 μ m. The thickness of the α -In₂Se₃ layer is $t = 30$ nm. The crystal structure of the single layer is reproduced from ref.¹⁷². (b) Schematic of the FSJ at equilibrium for opposite ferroelectric polarizations P . The dashed line sketches the potential profile for $P = 0$. (c-d) Current-voltage $|I|$ - V curves at low ($T = 100$ K) and room ($T = 300$ K) temperature showing counter-clockwise loops. The bottom layer graphene is grounded and a positive/negative voltage is applied to the top-graphene electrode. The $|I|$ - V s are asymmetric with respect to the polarity of V , suggesting two non-equivalent interfaces and larger electron transmission from the bottom to the top graphene electrode. (e) I - V s for different V -ranges ($T = 300$ K). (f) Temporal dependence of I at different V . After poling at $V = +1.5$ V, the FSJ switches to a lower resistive state. This can be erased by a negative voltage $V = -1.5$ V ($T = 300$ K).

A large electric field is required to induce a ferroelectric polarization in α -In₂Se₃ by displacements of the In- and Se-atoms within each vdW layer. The calculated amplitude of the electric dipoles is 0.11 and 0.03 $e\text{\AA}$ per α -In₂Se₃ unit cell for the two oppositely polarized configurations, influencing the atomic orbitals and energy band alignments at the graphene/ α -In₂Se₃ interface: the chemical potential in graphene

moves upward or downward according to the sign of the polarization charges so that more or fewer electrons can transverse the junction.⁸⁹ At low T (Figure 5.3c), the steeper increase of the current at $|V| > 1$ V suggests a switchable polarization of the ferroelectric layer, thus increasing the current throughout the junction; this behaviour is also observed at room temperature, but it is less pronounced (Figure 5.3d).

5.3.2 Transport mechanisms: thermionic injection and tunnelling

We probe the mechanisms of conduction in the FSJ and the robustness of the memristive behaviour against a rising temperature by considering the I - V s over a range of temperatures from $T = 100$ K to $T = 380$ K. As shown in Figure 5.4a, the counter-clockwise loop in I - V persists above $T = 300$ K, although is significantly reduced at $T = 340$ K. For $T < 150$ K, the current and hysteretic behaviours are weakly dependent on T ; in contrast, at higher temperatures, the current tends to increase exponentially with T , following a dependence described by $I \sim \exp(-E_a/k_B T)$, where k_B is the Boltzmann constant and E_a is an activation energy (Figure 5.4b). From the Arrhenius plots of Figure 5.4b, we extract the value of E_a and its dependence on V (Figure 5.4c): with increasing V , E_a first decreases, reaches a constant value between $V \sim 0.5$ V and $V \sim 1$ V, and then it decreases for $V > 1$ V.

The temperature dependence of the current suggests a contribution to the transport from the thermionic injection of electrons from the graphene electrode onto the CB of α -In₂Se₃ (Figure 5.4ci). For thermionic injection, the emission current density can be described as $J = J_s [\exp(qV/k_B T) - 1]$,¹⁷⁵ where $J_s = A^* T^2 \exp(-q\phi_B/k_B T)$, A^*

is the effective Richardson constant, $q = e$ is the elementary electron charge, and $q\phi_B$ is the Schottky barrier height at the graphene/semiconductor interface. The current is thermally activated with an activation energy E_a that increases with decreasing V extrapolating to $q\phi_B$ at $V = 0$. As shown in Figure 5.4c, our FSJs reveal this dependence at low V with $E_a = q\phi_B = (0.38 \pm 0.01)$ eV at $V = 0$.

The Schottky barrier model is in agreement with that expected from density functional theory for a graphene/ α -In₂Se₃ interface.⁸⁹ However, the graphene/ α -In₂Se₃ interface does not behave as a simple Schottky contact. The constant value of E_a with increasing V from $V \sim +0.5$ V to $V = +1$ V followed by a steep decrease for $V > +1$ V (Figure 5.4c) cannot be explained by thermionic injection. On the other hand, under a large applied electrical field, electrons can tunnel from the electrode onto the CB of α -In₂Se₃ through a triangular potential barrier (Fowler-Nordheim tunnelling, Figure 5.4cii), causing a weaker dependence of the current on temperature than for thermionic injection. Furthermore, as the voltage increases beyond the coercive field, the polarization charges at the graphene/ α -In₂Se₃ interface induce an effective lowering of the Schottky barrier (Figure 5.4ciii). This can account for the decrease of E_a at high V and the corresponding increase of conduction in the low-resistive ferroelectric state of the FSJ. In summary, the modulation of the graphene/ α -In₂Se₃ interface by polarization switching can be modelled as a tuneable Schottky barrier: a change in the height of the barrier modulates the transmission of electrons across the FSJ. At low T (< 150 K) charge injection is dominated by tunnelling, whereas thermal injection becomes more prominent as the temperature increases above $T = 150$ K. The

reduced memristive effects with increasing T arise from the increased current in the FSJ acting to diminish the polarization of α - In_2Se_3 .

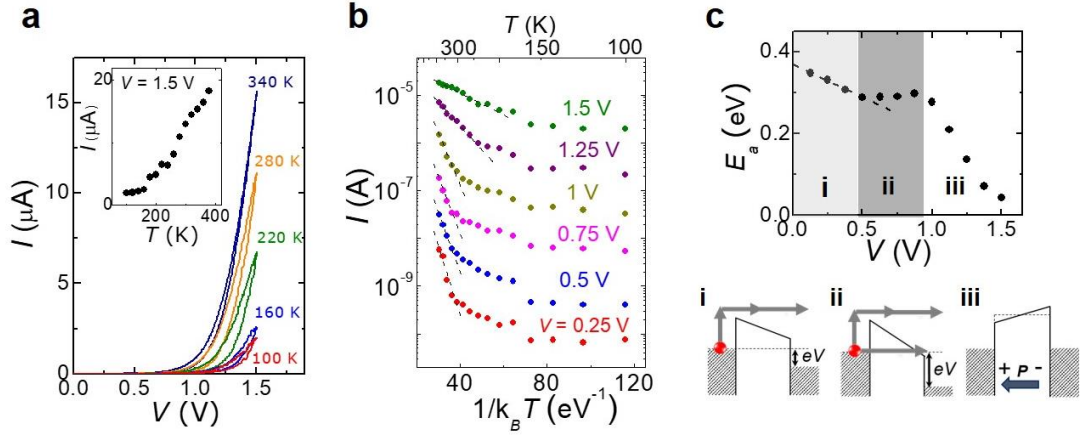


Figure 5.4 Conduction mechanisms in FSJs. (a) Current–voltage I – V curves at different temperatures T for a FSJ with an α - In_2Se_3 layer of thickness $t = 30$ nm. Inset: T -dependence of I at $V = +1.5$ V. (b) Arrhenius plot of I versus $1/k_B T$ at different V . The values of the current are obtained from part (a) along the I – V trace from 0 to $+1.5$ V. (c) Activation energy E_a versus V . The dashed line is a guide to the eye showing the extrapolation of E_a to the Schottky barrier height $e\phi_B$ at $V = 0$. The shaded areas identify regimes of voltages for (i) thermionic injection, (ii) tunnelling and (iii) ferroelectric polarization switching.

We have examined FSJs with different layer thickness (Figure 5.5). All devices show similar hysteretic behaviours in the electrical transport (Figures 5.4a and 5.5a). Although the transmission of electrons by direct tunnelling is reduced in thicker layers, trap-assisted tunnelling can dominate at high applied voltages. Under a large applied electrical field, the conduction electrons in the α - In_2Se_3 layer can acquire sufficient energy to ionize charge trap sites, generating additional electrons by inelastic collisions. Electron emission from traps is also influenced by the electric field due to

Poole-Frenkel emission.¹⁷⁵ Carrier traps can arise from In-vacancies and/or residual n -type dopants that reside in the interlayer gaps of α -In₂Se₃. Their existence is supported by Hall effect measurements of bulk α -In₂Se₃, giving a Hall electron density of up to $n = 4.9 \times 10^{17} \text{ cm}^{-3}$ at $T = 300 \text{ K}$.

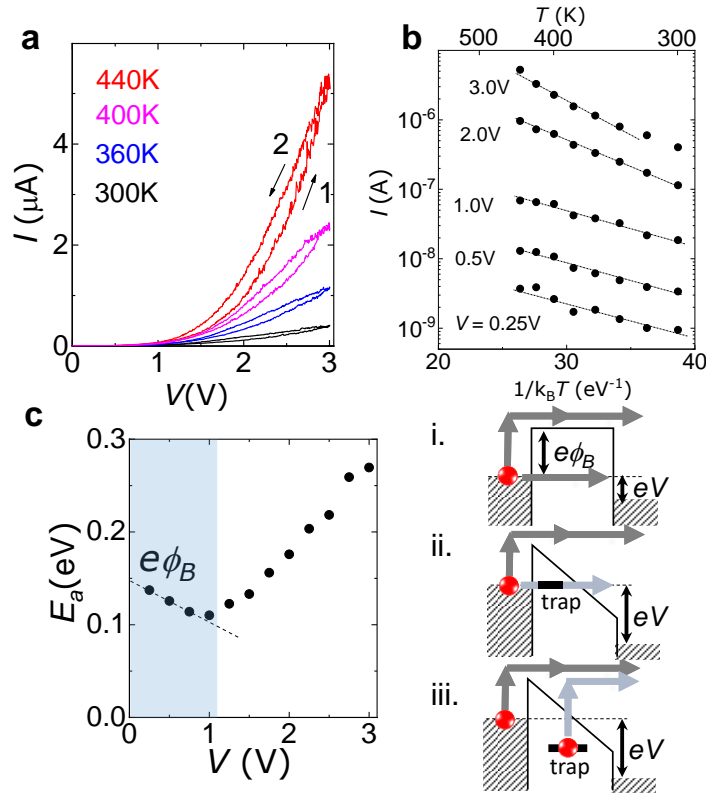


Figure 5.5 Conduction mechanisms in thick FSJs. (a) Current–voltage I – V curves at different temperatures T for a FSJ with an α -In₂Se₃ layer of thickness $t = 200 \text{ nm}$. (b) Arrhenius plot of the current versus $1/k_B T$ at different V . (c) Activation energy E_a versus V . The dashed line is a guide to the eye showing the extrapolation of E_a to the Schottky barrier height $e\phi_B$ at $V = 0$. The shaded and non-shaded areas identify regimes of voltages described by (i) thermionic injection of electrons from graphene onto the conduction band of α -In₂Se₃; (ii) trap-assisted tunnelling and (iii) impact ionization of traps at large electric fields.

Trap states can exist over a continuous energy range, thus accounting for almost

a continuous change in the activation energy from ~ 0.1 eV to 0.3 eV with increasing V from +1 V to +3 V (Figure 5.5c): as V increases, electrons from the deeper energy states are ionized and transmitted throughout the junction, thus increasing the current. The additional conduction electrons generated at high electric fields can neutralize the polarization charges at the graphene/ α -In₂Se₃ interface. The ionization of impurities and/or defects at high electric fields and/or temperature is pivotal to the operation of FSJs, requiring optimization of the doping properties of the ferroelectric semiconductor. We note that the thermal excitation of electrons from the valence band to the conduction band of α -In₂Se₃ creates free carriers whose density depends on the bandgap energy (E_g) and temperature ($E_g = 1.4$ eV at 300 K). The thermal activation energy for this process is significantly larger than that derived from the thermally activated behaviour of the current in the FSJs (Figures 5.4c and 5.5c). Thus, we infer that the intrinsic thermal excitation of carriers can be neglected.

5.4 FSJs under light illumination

Light provides a non-invasive method for switching ferroelectric properties and probing ferroelectrics^{120,176-180}: The built-in electric field due to the ferroelectric polarization can induce photovoltaic effects^{176,178} and modify the ferroelectric polarization by screening of polarization charges¹⁷⁹. Here, we examine light-polarization interactions in our FSJs using laser light of energy $h\nu = 1.96$ eV ($\lambda = 633$ nm) above the bandgap of α -In₂Se₃ ($E_g = 1.4$ eV at 300 K). In these experiments the FSJ is illuminated through the transparent top graphene electrode.

As shown in Figure 5.6, an increasing laser power P_i induces a positive photocurrent ΔI and reduces the hysteretic loops in I - V . We examine the photoresponse of the FSJ by considering the dependence of the photoresponsivity, $R = \Delta I/P_i$, on V and P_i for two FSJs with different layer thicknesses ($t = 30$ and 200 nm in Figures 5.7a, 5.7c and 5.7b, 5.7d, respectively). As can be seen in Figure 5.7, for both FSJs R increases by several orders of magnitude with increasing V and is larger at low powers.

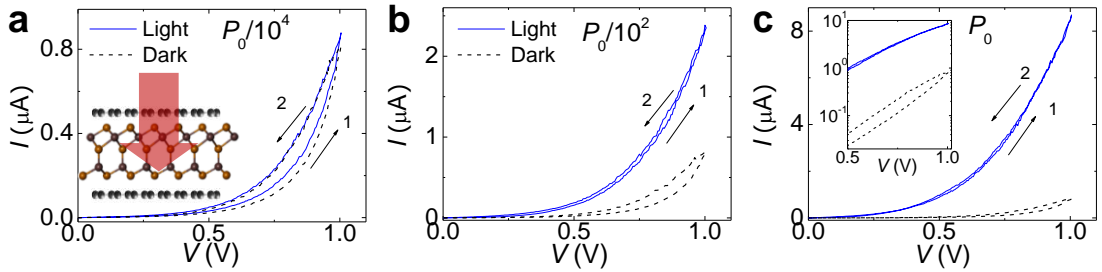


Figure 5.6 FSJs under light. Current–voltage I - V in the dark (black) and under laser light (blue) of energy $h\nu = 1.96$ eV ($\lambda = 633$ nm) and power (a) $P_0/10^4$, (b) $P_0/10^2$, and (c) P_0 for a FSJ with $t = 30$ nm ($T = 300$ K, $P_0 = 10^{-8}$ W). Inset, (a) panel: illumination of the FSJ from the top graphene electrode. Inset, (c) panel: I - V s with and without light.

At first glance, the photoresponse of the FSJ can be understood by considering the dynamics of photocreated carriers (Figure 5.7e). Under an applied voltage V , electrons and holes that are photoexcited in the α - In_2Se_3 layer are swept by the electric field in opposite directions and extracted at the graphene electrodes (Figure 5.7ei) to generate a photocurrent $\Delta I = [\eta \alpha P_i / h\nu] \tau_l / \tau_t$, where α is the absorption coefficient of α - In_2Se_3 at the photon energy $h\nu$, t is the thickness of the α - In_2Se_3 layer, and τ_l / τ_t is the ratio of the minority carrier lifetime (τ_l) and transit time (τ_t) of majority carriers in α - In_2Se_3 . In these FSJs, the majority carriers are electrons due to residual

n -type doping of α - In_2Se_3 ($n = 4.9 \times 10^{17} \text{ cm}^{-3}$ at $T = 300 \text{ K}$). Thus, we express R as $R = \Delta I / P_i = [e\tau\alpha/h\nu] \tau_l / \tau_e$ and the external and internal quantum efficiencies as $EQE = R(h\nu/e) = [\tau\alpha] \tau_l / \tau_e$ and $IQE = \tau_l / \tau_e$, respectively. These relations indicate that large values of R , EQE and IQE are achieved if the lifetime of holes is longer than the transit time of electrons.

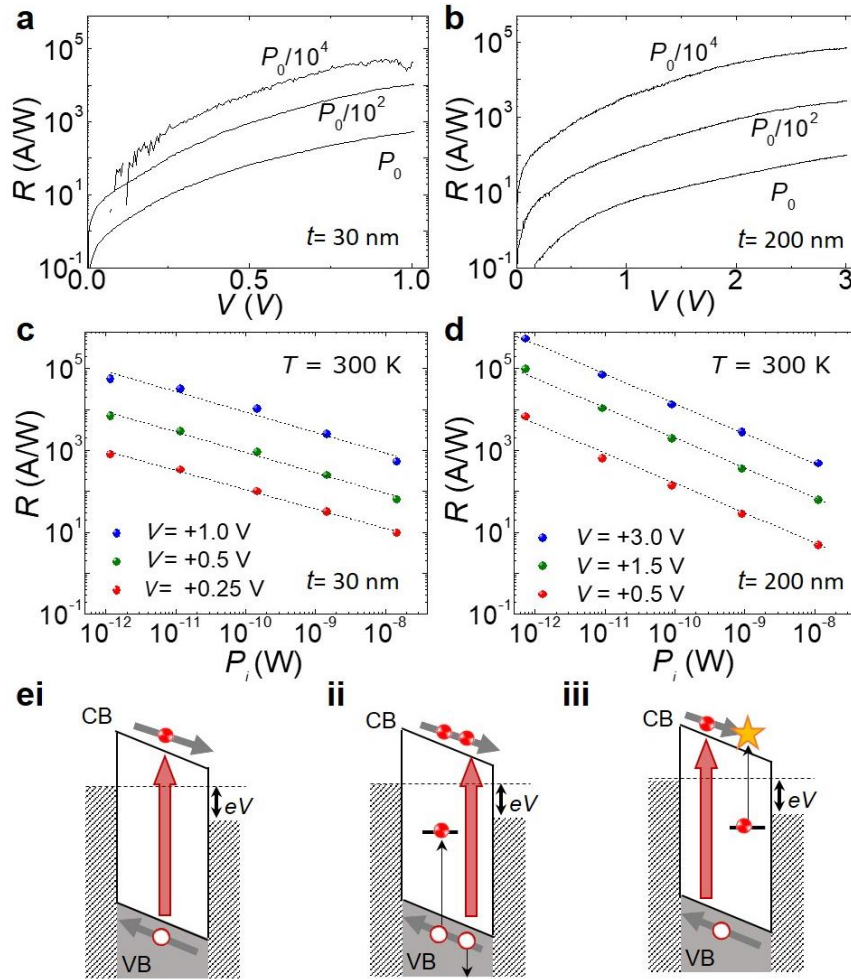


Figure 5.7 Photoresponsivity of FSJs. (a,b) Photoresponsivity (R) versus voltage (V) at different powers P_i for laser light of energy $h\nu = 1.96 \text{ eV}$ ($\lambda = 633 \text{ nm}$) and FSJs with $t = 30 \text{ nm}$ (a) and 200 nm (b) ($T = 300 \text{ K}$). (c,d) R versus P_i for different V and FSJs with $t = 30 \text{ nm}$ (c) and 200 nm (d) ($T = 300 \text{ K}$). Lines are fits to the data by a power dependence. (e) (i) Photogenerated electrons and holes and their separation by the electric field of the FSJ; (ii) capture of minority carriers (holes) by traps; (iii) impact ionization of traps.

As shown in Figures 5.7c and 5.7d, R follows a power dependence described by P_i^β with $\beta = -0.48 \pm 0.02$ for $t = 30$ nm and $\beta = -0.71 \pm 0.03$ for $t = 200$ nm. The largest values of R (up to $R = 10^6$ A/W) are reached for low $P_i = 10^{-12}$ W. For $t = 30$ nm, $V = +1$ V and $\alpha = 10^6$ m⁻¹ at $h\nu = 1.96$ eV, we estimate that τ_l/τ_t decreases from $\sim 2 \times 10^6$ to $\sim 2 \times 10^4$ with P_i going from 10^{-12} W to $\sim 10^{-8}$ W. A value of $\tau_l/\tau_t = 2 \times 10^6$ corresponds to a large internal gain with $IQE = 2 \times 10^6$, $EQE = R[h\nu/e] = 7 \times 10^4$ and $D^* = R(A/2eI)^{1/2} \sim 5 \times 10^{11}$ m/Ws^{-1/2}, where $A = 20$ μm^2 is the area of the device and $I = 0.8$ μA is the dark current at $V = +1$ V.

The decrease of R , EQE and D^* with increasing P_i is similar to that reported for other 2D materials^{47,49,55,181} and can be accounted for by the decrease of τ_l/τ_t with increasing P_i due to either a decrease of τ_l and/or an increase of τ_t with increasing P_i . The transit time of majority electrons can increase with P_i due to enhanced carrier scattering. The lifetime of minority holes is limited by Shockley–Read and surface recombination and is reduced at high carrier densities (or high P_i) due to Auger recombination.¹⁷⁵ The dependence of R on P_i is more pronounced in the thicker FSJs, suggesting a stronger contribution from trap-assisted carrier recombination (Figure 5.7eii). All our FSJs reveal a similar high, fast temporal photoresponse. Figure 5.8a shows the temporal dependence of the current under illumination of an FSJ with $t = 200$ nm. The rise (τ_r) and decay (τ_d) times of the current are derived from an exponential fit to the data (Figure 5.8b): they are both relatively short (0.1 - 1 ms) with $\tau_d > \tau_r$ and both decreasing with increasing V and/or P_i .

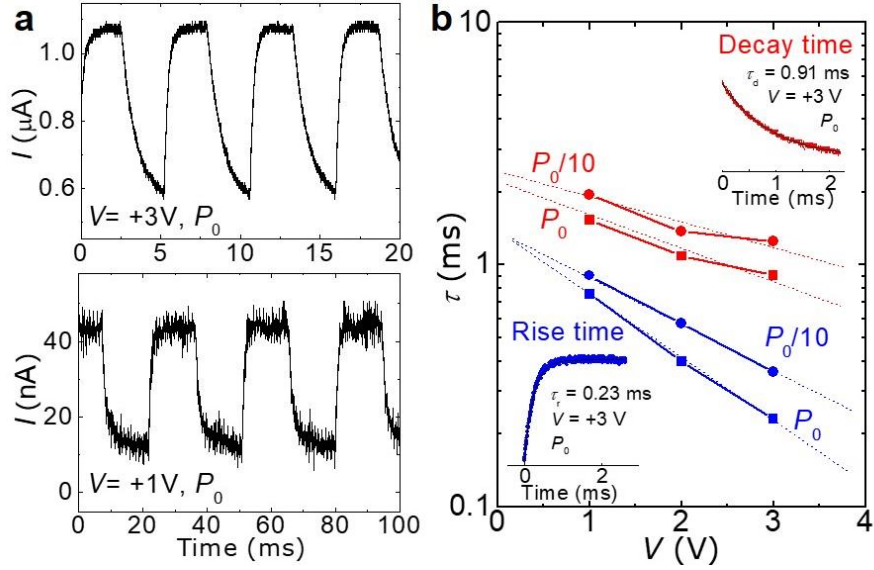


Figure 5.8 Modulation of the photocurrent in FSJs. (a) Temporal dependence of the current under illumination by a laser with wavelength $\lambda = 633$ nm, power $P_0 = 10^{-7}$ W and frequency $f < 200$ Hz at different voltages $V = +1$ V, $+3$ V. (b) V -dependence of the rise (τ_r) and decay (τ_d) times of the current at $P_0 = 10^{-7}$ W and $P_0 /10$. The rise times are marked in blue and the decay times are marked in red. Lines are guides to the eye. Insets: Exponential fit (lines) to the time-dependence of the current (points) to obtain τ_r and τ_d at $P_0 = 10^{-7}$ W and $V = +3$ V.

We examine the data on photoresponsivity under different applied voltages and powers to examine the role of the ferroelectric polarization on the photoresponse of the FSJs. The photoresponsivity increases by several orders of magnitude with increasing V (Figures 5.7a and 5.7b), reaching values comparable to or higher than those reported for other In_2Se_3 -based devices in the literature.^{56,111,115} The strong dependence of the photocurrent on V is also seen in tunnel junctions without the ferroelectric layer,⁴⁷ suggesting that the ferroelectric polarization of the In_2Se_3 layer does not play a critical role in the high values of R or in the dependence of R on V . The high photoresponsivity of the FSJ is primarily caused by a large internal gain and is not influenced by

polarization charges at the graphene/ α -In₂Se₃ interface. On the other hand, photocreated carriers act to neutralize polarization charges, reducing the hysteresis loops in I - V s (Figure 5.6).

5.5 α -In₂Se₃-capped graphene field effect transistors

To further investigate the interfacial electronic interactions and charge transfer at the α -In₂Se₃/graphene interface, we fabricated α -In₂Se₃-capped graphene field effect transistors (GFET), see the schematic and optical image in Figure 5.9a. A monolayer graphene flake is transferred onto a 300 nm SiO₂/Si substrate, which serves as the back gate. Two pre-patterned 100 nm/10 nm Au/Ti electrodes are used to contact the monolayer graphene layer, defining the source and drain of the FET. A 20-nm-thick α -In₂Se₃ is exfoliated on top of the graphene layer with an overlap area of 80 μm^2 . The α -In₂Se₃ and monolayer graphene flakes are encapsulated by a large area hBN flake.

The transfer characteristics of the α -In₂Se₃-capped GFET are measured at room temperature ($T = 300$ K). As shown in Figure 5.9b, the current–voltage $I_{\text{SD}}-V_{\text{G}}$ curves illustrate that the applied voltage required to reach the Dirac point shifts from $V_{\text{G}}^{\text{D}} = +17$ to $+27$ V going from the forward to the backward sweeping of V_{G} . The positive value of V_{G}^{D} indicates that graphene is p -type; also, the clockwise hysteresis of the transfer curve indicates the existence of defects at the graphene/In₂Se₃ interface.^{182,183} When a positive voltage is applied on the back gate, electrons are induced in the graphene channel. Some of these electrons can get trapped onto crystal defects in the

α -In₂Se₃ or at its interface with graphene. This localized charge is released slowly and acts as a negative “top gate” to induce holes in graphene. As a result, the $I_{SD} - V_G$ curve shifts towards positive V_G for the backward sweeping.

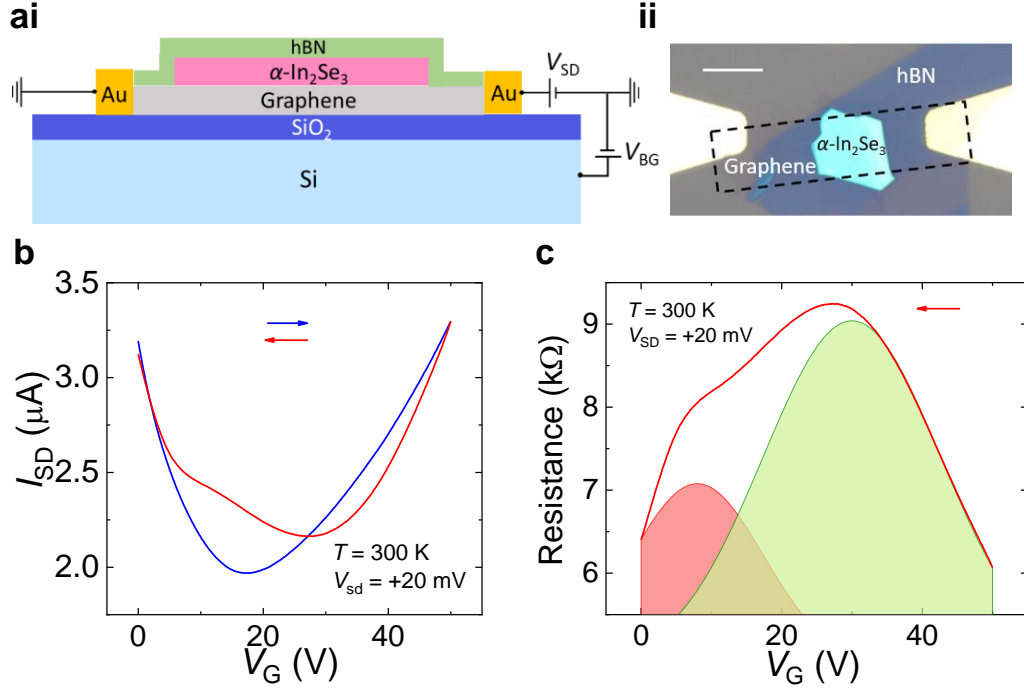


Figure 5.9 α -In₂Se₃-capped GFETs. (a) Schematic (i) and optical image (ii) of an α -In₂Se₃-capped GFET. Scale bar: 10 μ m. (b) Gate voltage dependence of source-drain current of an α -In₂Se₃-capped GFET. The $I_{SD} - V_G$ curves show a hysteresis between forward (blue) and backward (red) sweeps of V_G . (c) Resistance - V_G curve of the backward (red) sweep of V_G . The curve is convoluted by two distinct curves, contributed by pristine graphene and α -In₂Se₃-capped graphene, respectively.

Using the capacitance model for the FET¹⁸⁴, the carrier density of graphene can be estimated by $n = C_{SiO_2} V_G^D / e$, where $C_{SiO_2} = \epsilon \epsilon_0 / d = 1.15 \times 10^{-4}$ F/m² is the capacitance per unit area of the graphene/SiO₂/Si heterostructure, e is the elementary charge, $d = 300$ nm is the SiO₂ layer thickness, $\epsilon = 3.9$ is the relative dielectric

constant of SiO₂, and ϵ_0 is the permittivity of free space. At $V_G = 0$, the graphene hole density p increases from $1.2 \times 10^{12} \text{ cm}^{-2}$ to $1.9 \times 10^{12} \text{ cm}^{-2}$ going from the forward to the backward sweeping of V_G . The Fermi level relative to the Dirac point can be estimated by $E_F = v_F h \sqrt{n/4\pi}$, where $v_F = 10^6 \text{ m/s}$ is the Fermi velocity and h is the Planck constant. At $V_G = 0$, the Fermi level of graphene before and after sweeping lies at 0.13 eV and 0.16 eV below the Dirac point, respectively. Comparing backward and forward transfer curves near the graphene Dirac point, it can be seen that the slope dI/dV_G decreases, which indicate a reduction in carrier mobility due to charged impurities. As shown in Figures 5.9c, the backward transfer curves can be convoluted by two distinct curves that we assign to two types of graphene: pristine graphene ($V_G^D = +8 \text{ V}$) and α -In₂Se₃-capped graphene ($V_G^D = +30 \text{ V}$).

To obtain a better understanding of the graphene defects and charge transfer mechanism, we measured the transport characteristics of the α -In₂Se₃-capped GFET under illumination with laser light of energy $h\nu = 1.96 \text{ eV}$ ($\lambda = 633 \text{ nm}$) above the bandgap of α -In₂Se₃ ($E_g = 1.4 \text{ eV}$ at 300 K). Similar to other graphene hybrid photodevices¹⁸⁵⁻¹⁸⁷, carriers photogenerated in α -In₂Se₃ can transfer into the graphene layer, leading to a change of conductivity and enhanced photoresponse of graphene. As shown in Figure 5.10a, following light illumination, the $I_{SD} - V_G$ curve shifts to positive V_G ; this shift increases with increasing light power, indicating a light-induced p -doping effect of graphene. When the GFET is under light illumination, electron-hole pairs are generated in the α -In₂Se₃ layer. Because of the band bending at

the α -In₂Se₃/graphene interface (Figure 5.10ci), holes in the α -In₂Se₃ layer are more easily transferred to graphene while electrons tend to become localized on defects in the α -In₂Se₃ layer. As a result, the α -In₂Se₃ layer acts as a negative photogate and “pull down” the Fermi level of graphene (Figure 5.10cii), causing the transfer curves to shift to more positive V_G^D -values (Figure 5.10a).

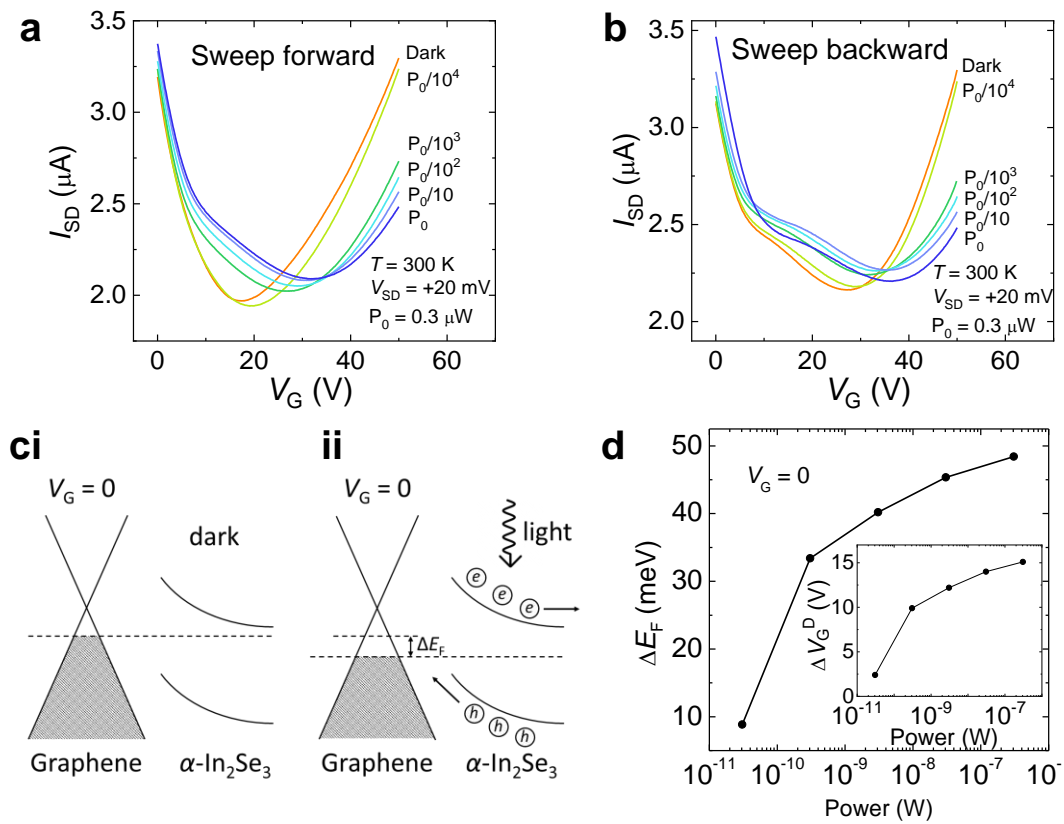


Figure 5.10 α -In₂Se₃-capped GFETs under light. (a) Source-drain current versus gate voltage V_G under different laser power ($\lambda = 633$ nm). The gate voltage is increased from 0 to +50 V. (b) Source-drain current versus gate voltage V_G under different laser power ($\lambda = 633$ nm). The gate voltage is decreased from +50 V to 0. (c) Band diagrams of the In₂Se₃/graphene heterostructure at $V_G = 0$ (i) in the dark and (ii) under light. (d) The shift of the Fermi level of graphene at $V_G = 0$ as a function of the laser power ($\lambda = 633$ nm). Inset: The shift of the graphene Dirac point ΔV_G^D in the I_{SD} - V_G curves as a function of the laser power ($\lambda = 633$ nm).

Using the capacitance model mentioned above, we can quantitatively investigate the value of the graphene Fermi level at $V_G = 0$. As the light power increases from 0.03 nW to 0.3 μ W, the “pull down” value ΔE_F of the graphene Fermi level at $V_G = 0$ increases from ~ 9 meV to 48 meV (Figure 5.10d). It can also be inferred that the number of electrons trapped in the α -In₂Se₃ layer saturates at high laser powers, leading to a corresponding saturation of ΔE_F . Similar to Figure 5.9c, we can convolute the transfer curve by two distinct curves, one associated to pristine graphene (the left peak), which is weakly affected by light, and one due to α -In₂Se₃/graphene (the right peak) that shifts under light (Figure 5.10b).

5.6 Summary

In conclusion, the polarization of the ferroelectric vdW semiconductor α -In₂Se₃ can be manipulated by applying a voltage across the two graphene electrodes of a graphene/ α -In₂Se₃/graphene junction. This acts to modify the Schottky barrier at the graphene/ α -In₂Se₃ interface: a change in the height of the barrier modulates the transmission of electrons across the interface, leading to memristive effects. This is a robust process over a wide range of temperatures. However, it can be influenced by ionization of defects and impurities that reside in n -type α -In₂Se₃, a phenomenon that tends to weaken the memristive effect. The additional free carriers generated by impact ionization, tunnelling and thermionic injection can neutralize the polarization charges at the graphene/ α -In₂Se₃ interface and influence the hysteretic behaviour in the electrical transport. Light provides an effective route for modifying electronic

properties and memristive effects. In particular, the FSJs reveal a high photoresponsivity and fast modulation of the photocurrent that exploit the optical absorption properties of α -In₂Se₃ and its favourable interface with graphene for charge extraction. Further research into device design, mechanisms and fabrication are crucial for reliable, optimized and predictable memristive behaviours and graphene-based vdW heterostructures with ferroelectric tunnelling barriers. Also, the development of ferroelectric semiconductors with controlled *n*- and *p*-type doping is critical to future implementation of ferroelectrics in multi-functional devices.

Chapter 6

Van der Waals interfaces for photodetection

This chapter reports a multi-layer junction that combines single-layer graphene and vdW semiconductors (p -GaSe and n -In₂Se₃) with strong optical absorption in the ultraviolet range. The junctions have broadband spectral response (0.3-1.0 μm) and high photoresponsivity under forward and reverse bias, or without any externally applied voltage. The photoresponse differs from that of a traditional pn -junction diode as it is governed by charge transport across thin layers and light-current conversion at three vdW interfaces (e.g. the graphene/GaSe, GaSe/In₂Se₃ and In₂Se₃/graphene interfaces). The type-II band alignment at the GaSe/In₂Se₃ interface and electric field at the three vdW interfaces are beneficial to suppress carrier recombination for enhanced photoresponsivity (up to $\sim 10^2$ A/W) and detectivity (up to $\sim 10^{13}$ Jones), beyond conventional UV-enhanced silicon detection technology.

The In₂Se₃ and GaSe bulk crystals were grown by Dr Zakhar Kudrynskyi and Prof. Zakhar Kovalyuk at The National Academy of Sciences of Ukraine. The exfoliated layers and devices were fabricated and modelled by myself and two 4th year undergraduate students under the supervision of Prof. Amalia Patanè. Transport measurements, optoelectronics experiments and optical studies were conducted by myself. The results presented in this chapter were published in *npj 2D Materials and Applications* **6**, 61 (2022).

6.1 Introduction

Photodetectors have potential for several applications, ranging from communication, aerospace and military technologies to pharmaceutical research.^{42,188} However, high-performance photodetection that extends into the ultraviolet (UV) range has proven to be challenging. Traditional Si-based thin-film technologies tend to underperform at short wavelengths due to a low optical absorption.^{43,189,190} Alternative devices, such as photomultiplier tubes (PMTs), charged-coupled devices (CCDs) and semiconductor photodiodes,^{42,191,192} can achieve higher absorption in the UV range but at the cost of a slow photoresponse, high power consumption and/or low efficiency.¹⁹²⁻¹⁹⁴ Two-dimensional (2D) van der Waals (vdW) semiconductors offer an alternative solution. They have tuneable absorption and fast temporal responses at room temperature while remaining flexible and power efficient.^{26,195-200} They also possess surfaces that are free of dangling bonds leading to a low density of interface traps and the formation of high-quality heterostructure devices without the need for lattice matching.²⁰¹ Thus, multi-layer vdW heterostructures could be used to enhance the performance of a photodetector by exploiting the optical properties of different materials and the unique effects that arise from their interactions, such as charge transfer, built-in electric fields, and moiré superlattices.²⁰²⁻²⁰⁵

Amongst the wide catalogue of 2D materials, the III-VI metal chalcogenide (MC) compounds have emerged as an ideal class of semiconductors for optoelectronics.^{26,55,206,207} High-performance photodetectors based on individual flakes of either GaSe or In₂Se₃ have been reported before.^{50,55,124,207,208} These two 2D

MC layers have optical bandgaps in the visible (GaSe)¹⁹⁴ and in the near-infrared (In₂Se₃)⁵⁷ spectral range, and strong absorption in the UV region.^{55,61,63,209} As demonstrated in Section 5.4, In₂Se₃ exhibits good photoresponse in FSJs. Here, we combined In₂Se₃ with GaSe to make photodiodes for broadband detection that extends into the UV range. The operation of this *pn*-junction based device differs qualitatively from that of a traditional semiconductor diode, as also observed in other thin vdW junctions in the literature.²¹⁰⁻²¹²

6.2 Photodetectors based on graphene-contacted *p*-GaSe/*n*-In₂Se₃ junctions

Figure 6.1a shows a schematic of the *p*-GaSe/*n*-In₂Se₃ heterojunction with two graphene electrodes (left) and an optical image of a typical device (right). The heterostructure is assembled by exfoliation and mechanical stamping of nanometer-thick vdW layers of α -In₂Se₃ and ϵ -GaSe. Details of the fabrication are in Chapter 3 Sample fabrication. The layers are prepared from bulk Bridgman-grown crystals of α -In₂Se₃ and ϵ -GaSe polytypes that have a hexagonal (2H) crystal structure (Figure 6.1b). The single α -In₂Se₃ vdW layer consists of five atomic layers stacked in the sequence Se–In–Se–In–Se (1 quintuplet layer, QL). For ϵ -GaSe, each vdW layer consists of four closely packed, covalently bonded, monoatomic sheets in the sequence Se–Ga–Ga–Se. Along the *c*-axis, the primitive unit cells of α -In₂Se₃ and ϵ -GaSe have lattice parameters of $c_{\text{In}_2\text{Se}_3} = 19.210 \text{ \AA}$ and $c_{\text{GaSe}} = 15.949 \text{ \AA}$, respectively. Within each *a*-*b* plane, atoms form hexagons with lattice parameters

$a_{\text{In}_2\text{Se}_3} = 4.031 \text{ \AA}$ and $a_{\text{GaSe}} = 3.755 \text{ \AA}$. Although the crystals are intentionally undoped, both layers contain residual dopants. For bulk $\alpha\text{-In}_2\text{Se}_3$, Hall effect measurements indicate an electron density $n = 4.9 \times 10^{17} \text{ cm}^{-3}$ at $T = 300 \text{ K}$ due to the existence of native donors.¹⁶⁰ The $p\text{-GaSe}$ crystals contain instead native acceptors and a low concentration of holes $p \sim 10^{13} \text{ cm}^{-3}$ at $T = 300 \text{ K}$.⁶⁰

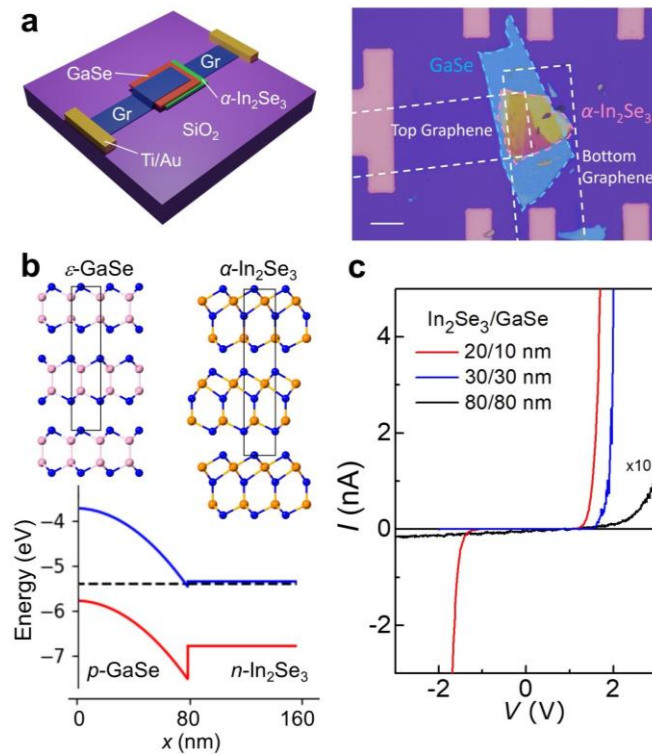


Figure 6.1 Graphene-contacted $p\text{-GaSe}/n\text{-In}_2\text{Se}_3$ heterojunctions. (a) Left: Schematic of a graphene contacted $p\text{-GaSe}/n\text{-In}_2\text{Se}_3$ junction. Right: Optical image of a device with $\alpha\text{-In}_2\text{Se}_3$ and $\epsilon\text{-GaSe}$ flakes with thickness of 20 nm and 10 nm, respectively. Scale bar: 10 μm . (b) Top: Crystal structure and unit cell of $\epsilon\text{-GaSe}$ and $\alpha\text{-In}_2\text{Se}_3$. Bottom: Band alignment and Fermi level (dashed line) of a bulk $\text{GaSe}/\text{In}_2\text{Se}_3$ junction in equilibrium. (c) Current–voltage $I\text{-}V$ curves in the dark ($T = 300 \text{ K}$) for three junctions with different layer thickness of the $\alpha\text{-In}_2\text{Se}_3$ (20, 30, 80 nm) and $\epsilon\text{-GaSe}$ (10, 30, 80 nm) flakes. The thicknesses are estimated by optical contrast measurements. The optical images for the 30/30 nm and 80/80 nm junctions are in Figure 6.5a and Figure 6.9a, respectively.

Figure 6.1b shows the type-II band alignment and built-in potential $eV_{\text{bi}} = 1.7$ eV of a p -GaSe/ n -In₂Se₃ junction at equilibrium at $T = 300$ K, as derived by solving Poisson's equation and taking into account the band alignment and doping of the bulk layers. Here, we have used the electron affinities from the literature ($\chi_{\text{GaSe}} = 3.7$ eV²¹³, $\chi_{\text{In}_2\text{Se}_3} = 3.6$ eV²¹⁴) and the measured bandgap energy of the bulk crystals ($E_{\text{GaSe}} = 2.0$ eV, $E_{\text{In}_2\text{Se}_3} = 1.4$ eV, see Figure 6.2). The depletion region of the junction extends primarily in the p -GaSe layer and is negligibly small in n -In₂Se₃ due to the much larger carrier concentration of In₂Se₃ (electron concentration in In₂Se₃ $\sim 4.9 \times 10^{17}$ cm⁻³ and hole concentration in GaSe $\sim 10^{13}$ cm⁻³). As shown in Figure 6.1c, the room-temperature current–voltage (I – V) characteristics are asymmetric with respect to the polarity of the applied voltage with a rectification ratio of up to 1000 at $V = \pm 2$ V (Figure 6.1c, blue curve). The current density remains small in both forward and reverse bias. Although the I – V curves of the junctions appear qualitatively similar to those of a traditional pn -junction, important differences emerge when we examine devices with thin layers (Figure 6.1c). As shown in Figure 6.1c, with decreasing layer thickness the current in both forward and reverse bias tends to increase and the I – V s become more symmetric with respect to the polarity of the applied voltage. These differences can arise from a qualitative change in the transport mechanisms. In a bulk-like junction, regions depleted of free carriers form on either side of the junction, thus generating built-in potentials. Carrier transport across the junction occurs by diffusion. However, for junctions composed of thin p - and n -type semiconductors, tunnelling-assisted interlayer recombination of majority carriers can increase the

current in forward bias;²¹² also, charge transport via tunnelling across a thin barrier between the two graphene electrodes and/or leakage via defects in the junction can dominate the current in both forward and reverse bias. Further differences emerge when we consider the photoresponse, as discussed below.

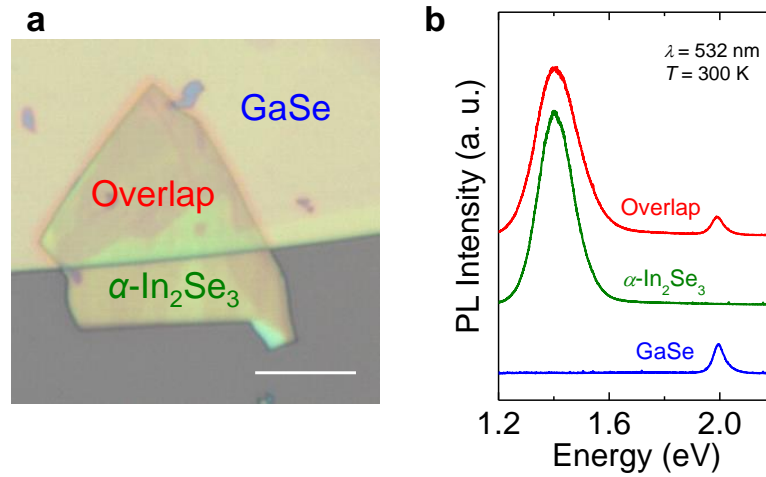


Figure 6.2 Photoluminescence of ϵ -GaSe, α -In₂Se₃, and ϵ -GaSe/ α -In₂Se₃ heterostructures. (a) Optical image of a GaSe/In₂Se₃ (thickness > 50/50 nm) heterostructure. Scale bar: 10 μ m. (b) Photoluminescence spectra (PL) of bulk In₂Se₃ and GaSe flakes, and their GaSe/In₂Se₃ overlapping area ($T = 300$ K, $\lambda = 532$ nm). The spectra show the band edge emission of In₂Se₃ and GaSe. The two emissions are centred at about 1.4 eV and 2 eV, respectively, as expected for isolated bulk layers.

Figure 6.3a shows the I - V characteristics of a junction under illumination with unfocused laser light of energy $h\nu = 3.06$ eV ($\lambda = 405$ nm). In both forward and reverse bias, the current increases with increasing incident power P_i . A photovoltaic response is also observed with a short-circuit current ($V = 0$) of up to 0.15 nA for $P_i = 0.11$ μ W (inset of Figure 6.3a). Figures 6.3b and 6.3c show the dependence of the photoresponsivity $R = \Delta I/P_i$, on V and P_i under unfocused light illumination with $\lambda =$

405 nm and $\lambda = 633$ nm, respectively. Here, $\Delta I = I_{\text{light}} - I_{\text{dark}}$ is the photocurrent. A large value of R of up to 145 A W^{-1} is observed at $V = +3 \text{ V}$ at $\lambda = 405 \text{ nm}$ and $P_i = 0.11 \text{ nW}$. The corresponding values of the external quantum efficiency ($EQE = Rhv/e$) and detectivity ($D^* = R(A/2eI_{\text{dark}})^{1/2}$) are $EQE = 4.4 \times 10^2$ and $D^* = 1.0 \times 10^{13}$ Jones, where $A = 20 \text{ }\mu\text{m}^2$ is the area of the device. Also, we estimate the noise equivalent power (NEP) as $NEP = \frac{I_{\text{noise}}}{R}$, where I_{noise} is the noise current derived from the standard deviation in the temporal fluctuations of the dark current. For $R = 145 \text{ A/W}$ and $I_{\text{noise}} = 4.8 \times 10^{-12} \text{ A}$, $NEP = 3.3 \times 10^{-14} \text{ W}$. The corresponding signal-to-noise ratio is $SNR = \frac{I_{\text{signal}}}{I_{\text{noise}}} = 6.0 \times 10^4$. For all applied voltages, R is approximately one order of magnitude larger at $\lambda = 405 \text{ nm}$ than at $\lambda = 633 \text{ nm}$, reflecting an increased optical absorption of the layers at shorter wavelengths. Furthermore, the junction can be switched between on and off states in a reproducible manner with rise and decay times of $\tau \sim 100 \text{ ms}$ and without any photo-induced memory effects and/or hysteresis in the I - V s (Figure 6.4). The trapping/detrapping of charge carriers due to the disordered potential of the heterostructure and/or crystal defects tend to slow down the photoresponse. We estimate the bandwidth from the photocurrent rise time/decay time, e.g. $f_{3\text{dB}} = 0.35/\tau = 4.5 \text{ Hz}$ and $\Delta f = f_{3\text{dB}}/0.886 = 5.1 \text{ Hz}$. Here, $f_{3\text{dB}}$ is the 3-dB bandwidth of the detector. This is defined as the frequency at which the photocurrent decreases by 3 dB of its maximum value.²¹⁵ Using these parameters to estimate the detectivity, we find $D^* = \frac{\sqrt{A\Delta f}}{NEP} \sim 3 \times 10^{10}$ Jones. This is smaller than the value of $D^* \sim 10^{13}$ Jones, as derived from $D^* = R(A/2eI_{\text{dark}})^{1/2}$, which assumes that the total noise is dominated by the shot noise from the dark current.

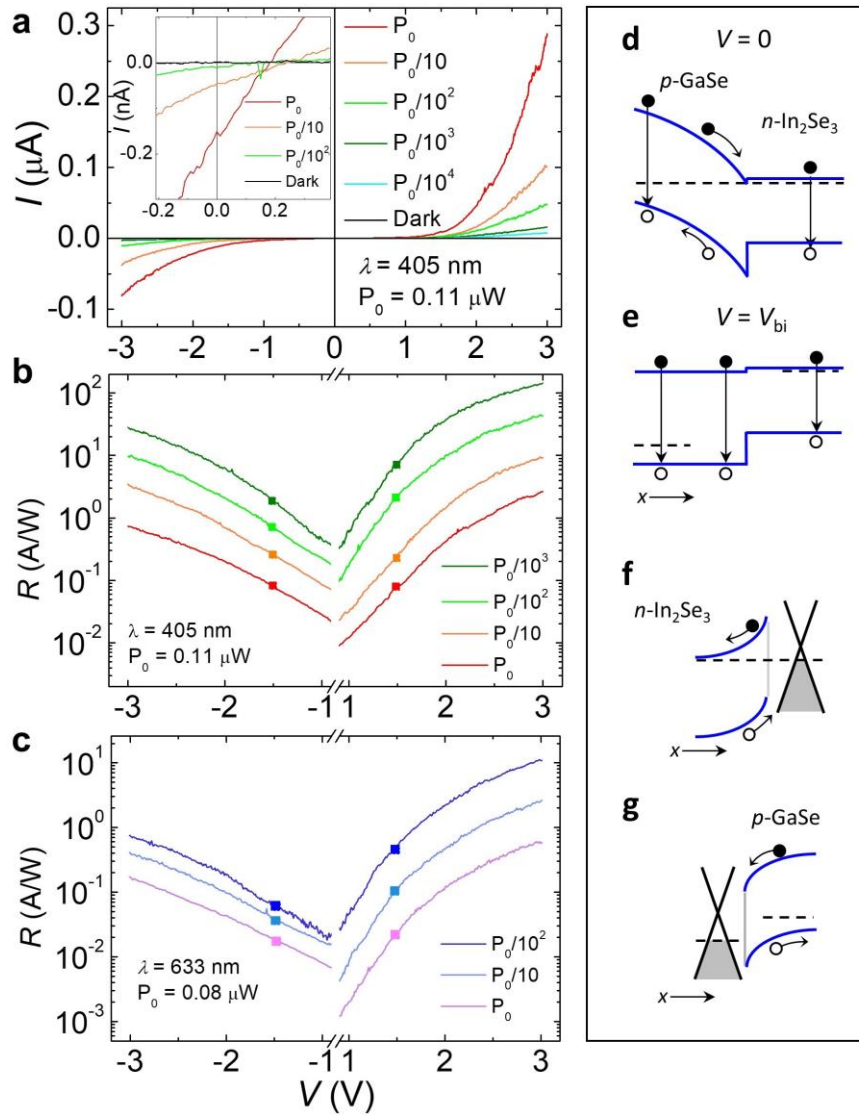


Figure 6.3 Heterojunctions under light illumination. (a) Current–voltage I – V characteristics of a graphene/ p -GaSe/ n -In₂Se₃/graphene junction (thickness of In₂Se₃/GaSe \sim 80/80 nm, optical image of the junction shown in Figure 6.9a) in the dark and under illumination with $\lambda = 405$ nm and different powers ($T = 300$ K, $P_0 = 0.11$ μ W). Inset: I – V curves near zero bias. (b–c) Photoresponsivity (R) versus V at different powers for (b) $\lambda = 405$ nm ($P_0 = 0.11$ μ W) and (c) $\lambda = 633$ nm ($P_0 = 0.08$ μ W) at $T = 300$ K. Square dots illustrate that the value of R in forward bias is larger than that in reverse bias. (d–g) Band alignment at the (d–e) GaSe/In₂Se₃, (f) In₂Se₃/graphene, and (g) graphene/GaSe interfaces. For the GaSe/In₂Se₃ interface, the alignment is shown at (d) equilibrium and (e) $V = V_{bi}$, where eV_{bi} is the built-in potential at the GaSe/In₂Se₃ junction.

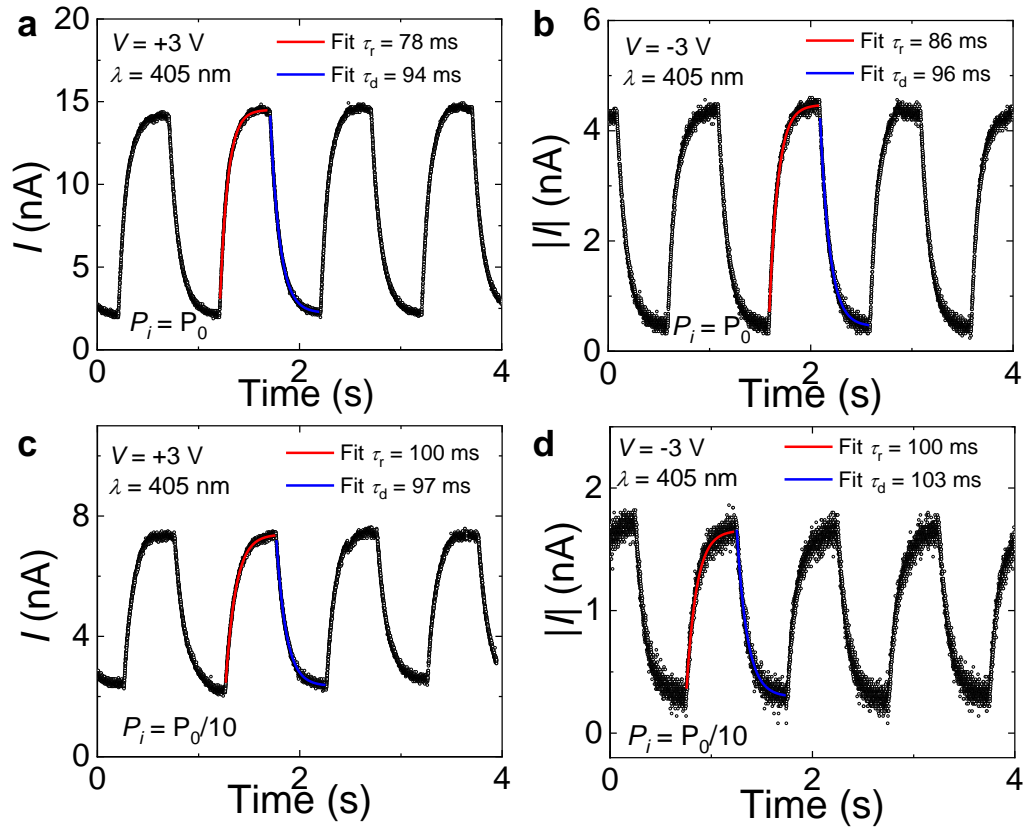


Figure 6.4 Time-dependent photocurrent of a device. Temporal dependence of the current under illumination at $\lambda = 405$ nm, power (a-b) $P_0 = 0.08 \mu\text{W}$ and (c-d) $P_0/10$ at different voltages $V = \pm 3$ V. The rise and decay times shown in these plots were estimated by fitting the data by $I(t) = I_0(1 - e^{-t/\tau_r})$ and $I(t) = I_0 e^{-t/\tau_d}$. The corresponding fits are plotted alongside the original dataset as red and blue lines.

We have investigated junctions with different thickness of the layers (Figures 6.5 and 6.6) and all devices revealed a similar behaviour with a photoresponse that extends from the NIR (near-infrared) to the VIS (visible) and the UV range even without any applied voltage. Figure 6.7 shows the dependence of the responsivity on the photon wavelength at $V = 0$ for a junction based on a relatively thin (~ 60 nm) $p\text{-GaSe}/n\text{-In}_2\text{Se}_3$ junction. It can be seen that the photoresponse increases with decreasing photon wavelength, with a stronger increase observed at energies larger

than the bandgap energy of GaSe ($E_g = hc/\lambda = 2.0$ eV, corresponding to $\lambda = 620$ nm). Although the responsivity remains high in all devices, the detectivity and photovoltaic response tend to become weaker in the shorter junctions due to larger dark currents and shorter depletion regions.

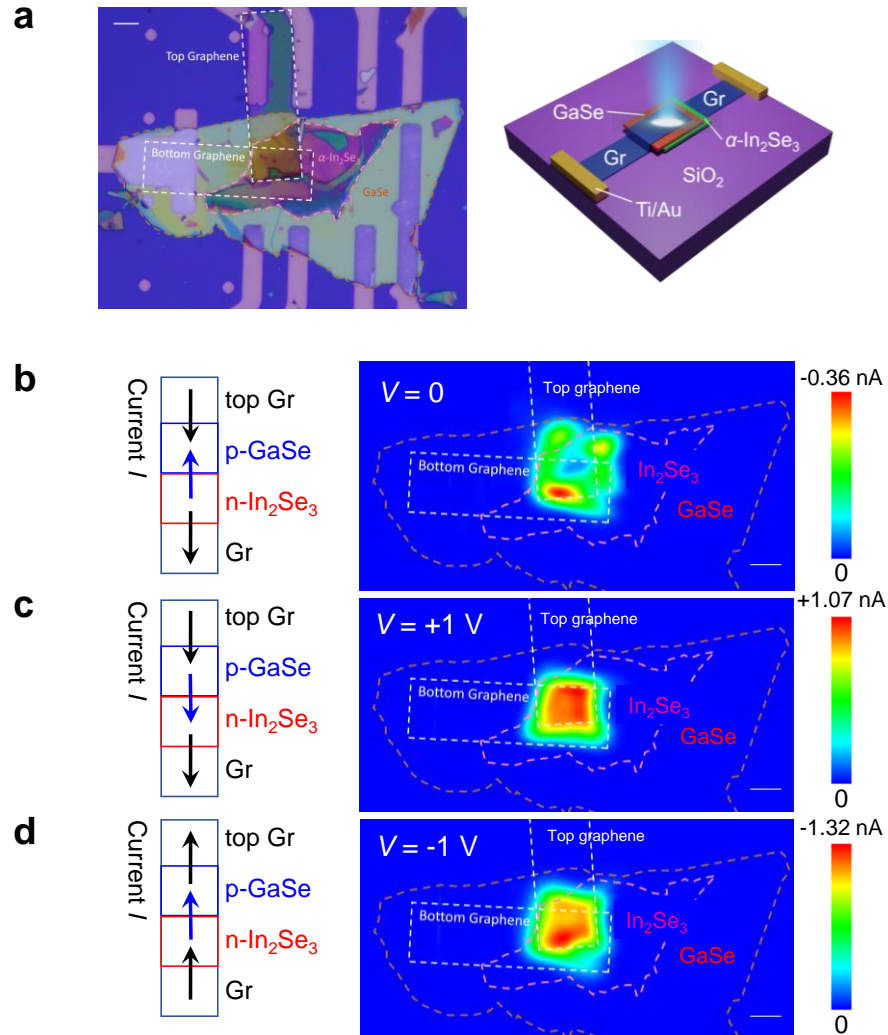


Figure 6.5 A graphene-contacted p -GaSe/ n -In₂Se₃ (30/30 nm) heterojunction. (a) Left: Optical image of the device. Right: Schematic of a graphene contacted p -GaSe/ n -In₂Se₃ junction (30/30 nm). Scale bar: 10 μ m. (b-d) Photocurrent (ΔI) maps at (b) $V = 0$, (c) +1 V and (d) -1 V. The laser beam ($\lambda = 425$ nm and $P_i = 15$ μ W) has a spot size of about 1 μ m. Scale bar: 10 μ m. The left insets illustrate the direction of the current across the three interfaces of the heterostructure.

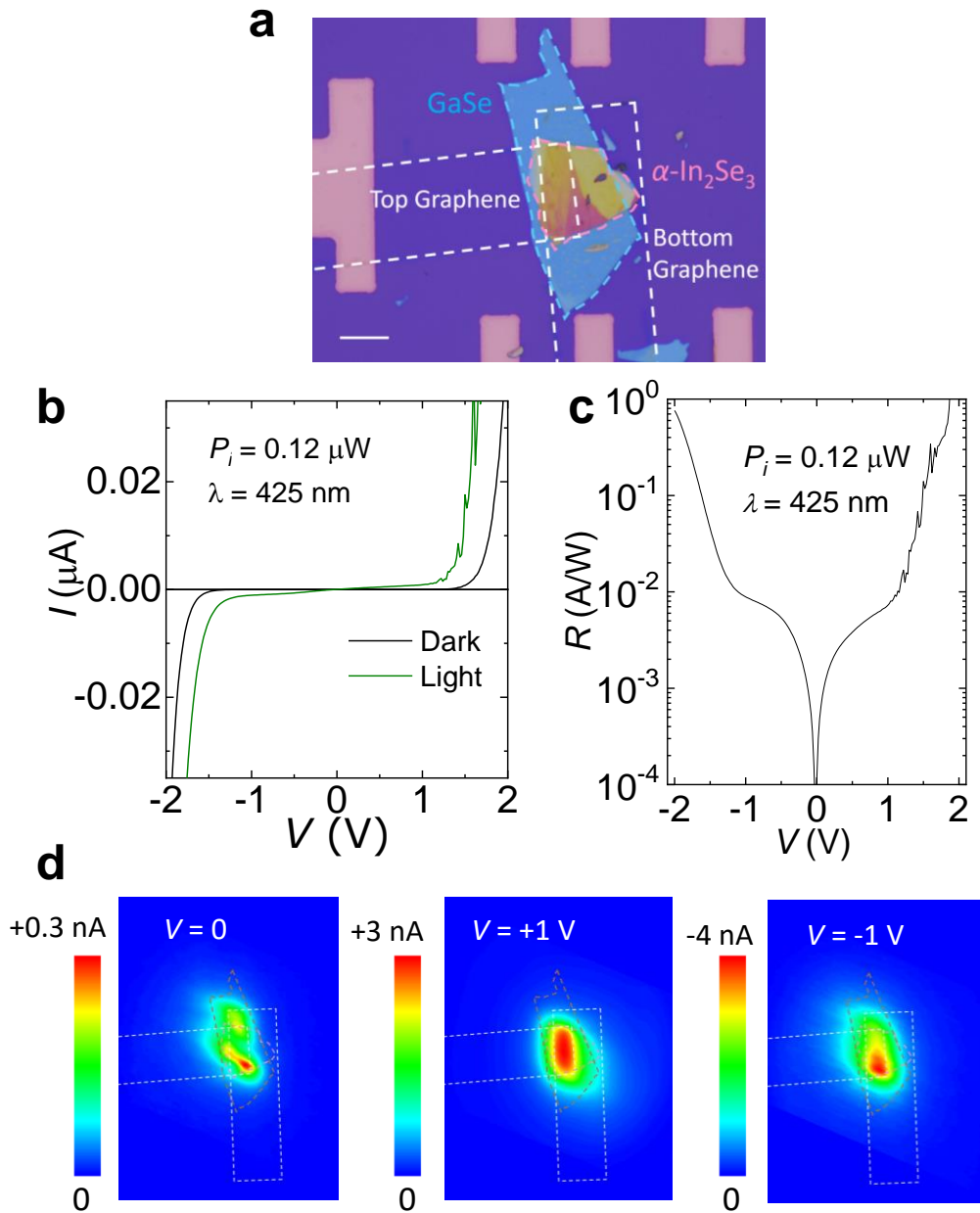


Figure 6.6 A graphene-contacted p -GaSe/ n -In₂Se₃ (10/20 nm) heterojunction. (a) Optical image of the device. Scale bar: 10 μm . (b) Current–voltage I – V characteristics in the dark and under illumination with $\lambda = 425$ nm ($T = 300$ K, $P_i = 0.12$ μW). (c) Photoresponsivity (R) versus V at $\lambda = 425$ nm ($P_i = 0.12$ μW) and $T = 300$ K. (d) Room temperature ($T = 300$ K) photocurrent (ΔI) maps at $V = 0$, $+1$ V and -1 V. The laser beam ($\lambda = 425$ nm and $P_i = 20$ μW) is focused by a microscope objective and the diameter of the spot size is around 1 μm . It can be seen that the photocurrent originates primarily from the region of overlap of the p -GaSe and n -In₂Se₃ layers with the bottom and top-graphene layers, rather than just the p -GaSe and graphene layers.

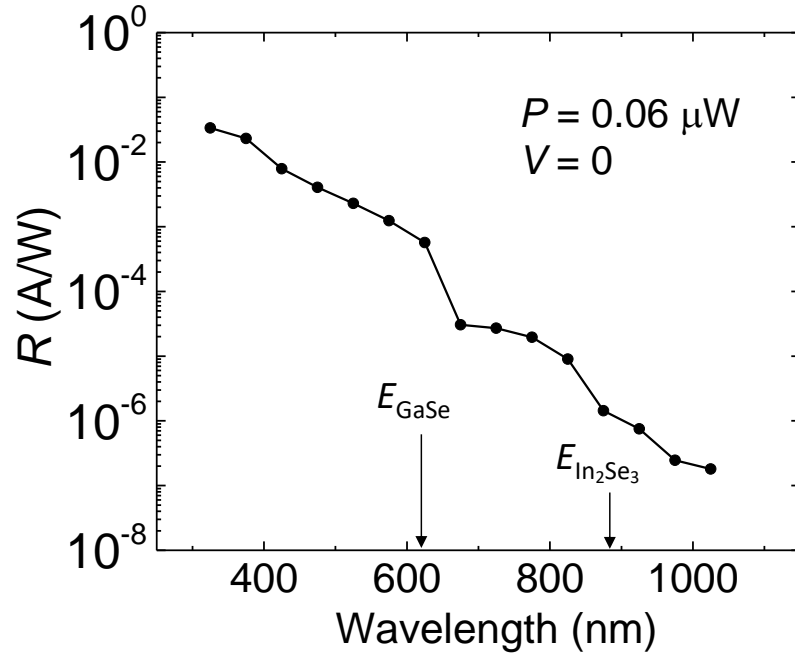


Figure 6.7 Wavelength-dependent photoresponsivity. Dependence of the photoresponsivity (R) on the photon wavelength for a graphene contacted p -GaSe/ n -In₂Se₃ junction (GaSe/In₂Se₃ thickness $\sim 30/30$ nm) at $V = 0$ and power $P_i = 0.06 \mu\text{W}$. The arrows indicate the bandgap energies of GaSe and In₂Se₃.

The responsivity of all devices is comparable or higher than the values for photodetectors based on individual flakes of GaSe^{50,55,61} or In₂Se₃^{56,57,111,124,179}. Also, p - n heterojunctions based on GaSe from this work and the literature (Table 6.1) tend to have a photoresponsivity that is higher under forward bias conditions. This behaviour differs from that of a traditional diode. In the latter, the photocurrent is larger in reverse bias as the spatial extent of the space charge region and the magnitude of the electric field increase with increasing reverse bias, thus facilitating the separation of photocreated electrons and holes and their collection at the electrodes. However, for our junctions, as the forward voltage increases above $V \sim +1.5$ V (Figures 6.3a-c), the photocurrent and photoresponse can become larger than

that in reverse bias. This behaviour is observed for different powers and laser wavelengths. Thus, the photoresponse cannot arise just from the photon-current conversion at the $\text{In}_2\text{Se}_3/\text{GaSe}$ interface (Figures 6.3d and 6.3e) and additional mechanisms should be considered at large positive V .

Table 6.1 Comparison of device performance parameters for UV photodetectors based on Si or vdW heterostructures from this work and the literature.

Materials	Responsivity	Working wavelength	Bias condition	Reference
Si	0.75 A W^{-1}	200 – 560 nm	2 V	216
a-Si:H	0.15 A W^{-1}	260 nm	20 V	217
WS_2/Si	5.7 A W^{-1}	340 – 1100 nm	-5 V	218
MoS_2/GaAs	0.657 A W^{-1}	300 – 873 nm	-1 V	219
GaSe/WS_2	149 A W^{-1}	270 – 740 nm	2 V	26
GaSe/InSe	350 A W^{-1}	270 – 920 nm	2 V	49
$\text{GaSe}/\text{Ga}_2\text{O}_3$	51.9 A W^{-1}	< 280 nm	10 V	51
InSe/ReS_2	1921 A W^{-1}	365 – 965 nm	1 V	220
$\text{GaSe}/\text{In}_2\text{Se}_3$	145 A W^{-1}	325 – 1025 nm	3 V	This work

6.3 Energy band alignment

We examined the energy band alignment for a graphene/ p -GaSe/ n - In_2Se_3 /graphene junction at $V = 0$ and under forward bias. The calculated band diagram at $V = 0$ is shown in Figure 6.8a and band diagrams at forward biases are shown in Figures 6.8b and 6.8c. We assumed that the layers are

fully depleted and that the pn -junction and Schottky junctions can be treated in isolation. Parameters (carrier density and electron affinity) for pristine graphene were used for both Schottky contacts and any shift in the Fermi level of graphene due to charge transfer between the semiconductors and graphene was neglected.

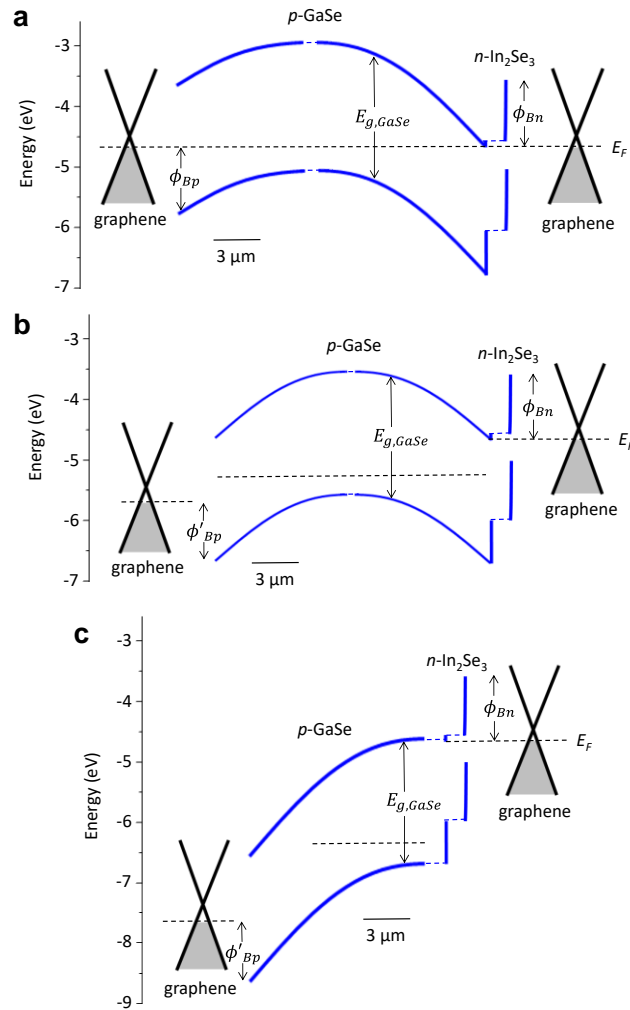


Figure 6.8 Energy band diagrams. Energy band diagrams of graphene-contacted p -GaSe/ n -In₂Se₃ heterojunctions at (a) $V = 0$, (b) $V = +1$ V and (c) $V = +2.95$ V. Blue dashed lines represent flat band regions of arbitrary length between the depletion regions.

Firstly, the energy step from (to) the valence (conduction) band in GaSe (In₂Se₃) to (from) the Fermi level is calculated using

$$V_p = k_B T \ln\left(\frac{N_V}{p}\right) = 0.37 \text{ eV} \quad (V_n = k_B T \ln\left(\frac{N_C}{n}\right) = 0.046 \text{ eV}), \quad (6.1)$$

where N_V (N_C) is the effective density of states in the valence (conduction) band and is given by

$$N_V = 2 \left(2\pi m_V^* k_B T / h^2\right)^{3/2} \quad (N_C = 2 \left(2\pi m_C^* k_B T / h^2\right)^{3/2}), \quad (6.2)$$

where m_V^* (m_C^*) is the effective mass of holes (electrons) in the valence (conduction) band (Table 6.2).

From the electron affinity of the layers ($\chi_p = \chi_{\text{GaSe}} = 3.7 \text{ eV}$ ²¹³, $\chi_n = \chi_{\text{In}_2\text{Se}_3} = 3.6 \text{ eV}$ ²¹⁴ and $\chi_{\text{Graphene}} = 4.5 \text{ eV}$ ⁴⁷) and their doping (Table 6.2), we estimated the Schottky barrier in GaSe $\phi_{Bp} = E_{g,p} + \chi_p - \phi_m = 1.04 \text{ eV}$ (Figure 6.8a). The Fermi level in the graphene layers (as measured in graphene field effect transistors is 0.16 eV below the Dirac point, corresponding to a hole concentration of $1.17 \times 10^{12} \text{ cm}^{-2}$) was treated as the work function of a metal, $\phi_m = \chi_{\text{Graphene}} + 0.16 \text{ eV} = 4.66 \text{ eV}$. The corresponding built-in potential is $V_{bi,p} = \phi_{Bp} - V_p = 0.67 \text{ eV}$. The depletion region width in the GaSe is $x_p = \sqrt{\frac{2\epsilon_s(V_{bi,p} - V)}{qp}} = 8 \mu\text{m}$ at zero bias, where ϵ_s is the dielectric permittivity of GaSe. A similar approach was used to calculate the corresponding parameters in In_2Se_3 , giving $\phi_{Bn} = \phi_m - \chi_n = 1.06 \text{ eV}$, $V_{bi,n} = \phi_{Bn} - V_n = 1.01 \text{ eV}$ and $x_n = \sqrt{\frac{2\epsilon_s(V_{bi,n} - V)}{qn}} = 54 \text{ nm}$ at zero bias. The pn -junction has a built-in potential given by $V_{bi,pn} = E_{g,p} + \chi_p - \chi_n - V_n - V_p = 2.0 + 3.7 - 3.6 - 0.046 - 0.37 = 1.68 \text{ eV}$.

The carrier concentration in In_2Se_3 is much higher than that in GaSe, so we treat the junction as one-sided and abrupt, with a depletion region entirely contained within the GaSe given by $W = \sqrt{\frac{2\epsilon_s(V_{bi,pn} - V)}{qp}} = 10.7 \mu\text{m}$ at $V = 0$.

Under an applied bias, we assumed that the electric field is linear throughout the structure. The relative voltage drop across the junctions is therefore equivalent to their relative depletion widths in the case of a device with layer thicknesses equal to the combined depletion widths from each junction. The depletion widths in GaSe are much larger than in In₂Se₃ due to the much lower carrier concentration in GaSe. In forward bias, this results in a negligible change in the bending of the In₂Se₃ bands (Figure 6.8b). In GaSe, the forward bias reduces the height of the *pn*-junction barrier, reaching the flat band condition $V_{bi,pn} = 1.68$ V at a total forward bias of $V = +2.95$ V (Figure 6.8c). The reduction in barrier height is also accompanied by a decrease in the depletion width, reducing to zero at the flat band condition. The GaSe band bending near the GaSe/graphene interface increases under a forward bias.

When the junction is forward biased, the photocurrent can increase due to an enhanced contribution to the photoresponse from the separation of electron-hole pairs at the In₂Se₃/graphene and GaSe/graphene interfaces (Figures 6.8b and 6.8c). Thus, in forward bias, both interfaces behave as reverse-biased Schottky contacts and can contribute to the I - V with a photocurrent that has the same polarity as the dark current. In summary, the three interfaces of the graphene/*p*-GaSe/*n*-In₂Se₃/graphene heterostructure contribute to the photodetection. Although our model does not capture the evolution of the multi-layer structure as the layer thickness decreases down to a few nanometres, it illustrates that the built-in potential at the three interfaces plays a critical role in the photoresponsivity. This is further examined by spatial mapping of the photoresponse of junctions with different thickness.

Table 6.2 Parameters of GaSe, In₂Se₃ and graphene used in the calculation of the energy band diagrams.

Properties	GaSe	In ₂ Se ₃	Graphene	Reference
m^*	0.8 m_0	0.24 m_0	N/A	221
p (n)	$1.0 \times 10^{13} \text{ cm}^{-3}$	$4.9 \times 10^{17} \text{ cm}^{-3}$	$1.2 \times 10^{12} \text{ cm}^{-2}$	This work
χ	3.7 eV	3.6 eV	4.5 eV	47,213,214
E_g	2.0 eV	1.4 eV	N/A	This work
ϵ_s	6.18 ϵ_0	16.68 ϵ_0	N/A	221
Φ_B	1.04 eV	1.06 eV	N/A	This work
V_{bi}	0.67 eV	1.01 eV	N/A	This work
$W_{Schottky} (V = 0)$	8 μm	54 nm	N/A	This work

6.4 Scanning photocurrent microscopy

We used a confocal optical microscope to obtain a photocurrent map of the junctions by focusing and scanning a laser beam onto the layer plane of the samples (Figures 6.5, 6.6 and 6.9). Figure 6.9a shows the bias-dependence of the photocurrent under focused laser excitation of a junction (inset of Figure 6.9a). The corresponding I - V curves under unfocused laser excitation are shown in Figure 6.3a. Figures 6.9b-f show the corresponding photocurrent maps of the device acquired under a range of bias voltages. To distinguish the different areas of the heterojunction, in each map, the GaSe, In₂Se₃ and graphene layers are marked by dashed lines. At zero bias (Figure 6.9b), the photocurrent signal arises from the area where the four layers (top and bottom graphene, GaSe and In₂Se₃) of the heterostructure overlap, indicating a built-in

potential at the pn -junction and efficient extraction of photo-created carriers at the two graphene electrodes.

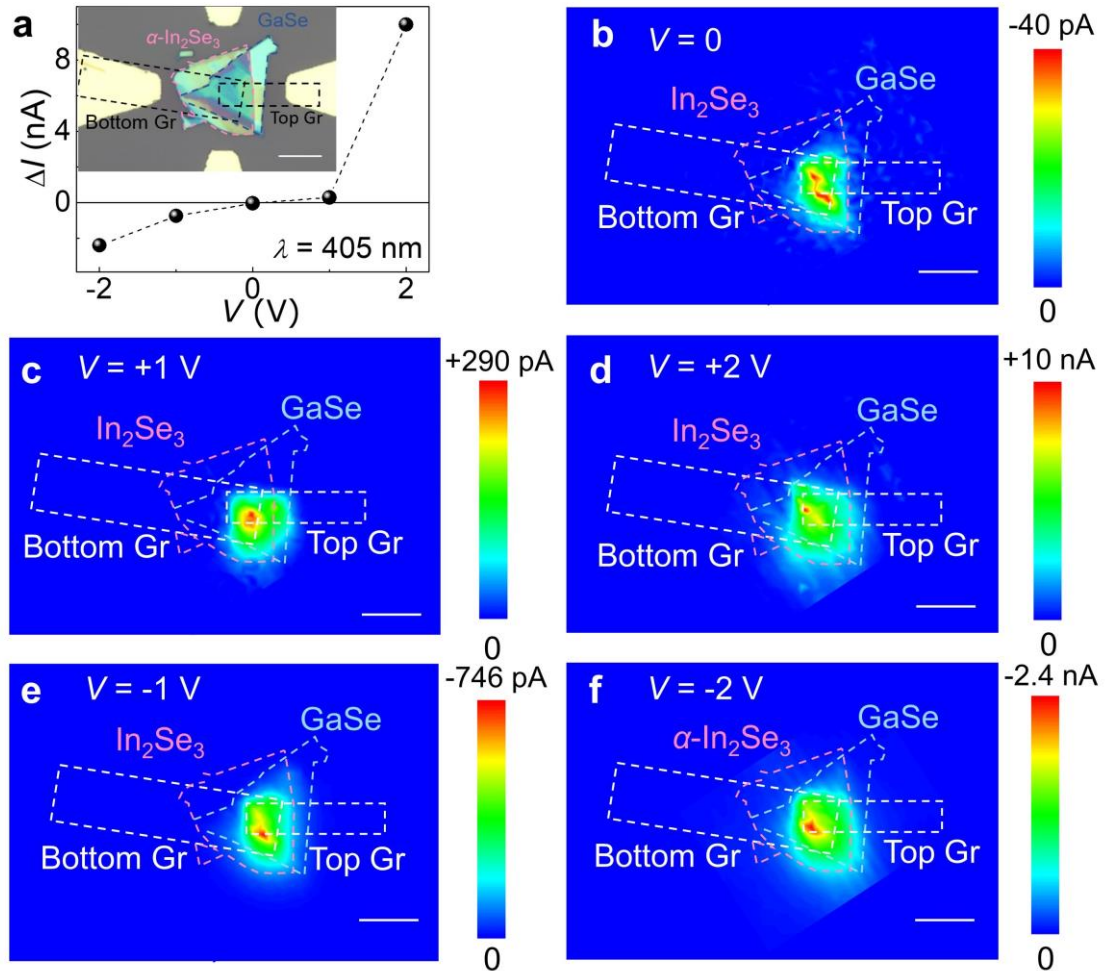


Figure 6.9 Photocurrent maps. (a) Room temperature ($T = 300$ K) photocurrent (ΔI) versus V under a focused laser beam ($\lambda = 405$ nm and $P_i = 0.75$ μW) for a bulk (thickness of $\text{In}_2\text{Se}_3/\text{GaSe} \sim 80/80$ nm) junction. The corresponding I - V curves under unfocused laser light are in Figure 6.3. The data correspond to the largest value of ΔI at each V . Inset: optical image of the device. Scale bar: 10 μm . (b-f) Photocurrent maps under bias $V = 0, +1, +2, -1, -2$ V. The laser beam ($\lambda = 405$ nm and $P_i = 0.75$ μW) is focused by the microscope objective to a spot size of around 1 μm . Scale bar: 10 μm .

Some general considerations can be drawn from the inspection of the photocurrent maps of several junctions. For example, by comparing the photocurrent maps of Figure 6.9, it can be seen that at $V = \pm 1$ V (Figures 6.9c and 6.9e) the amplitude of the photocurrent signal in forward bias is smaller than that in reverse bias; in contrast, at $V = \pm 2$ V (Figures 6.9d and 6.9f), the photocurrent in forward bias is larger than in reverse bias. This behaviour is illustrated by the bias dependence of the photocurrent in Figure 6.9a and is consistent with the I - V characteristics acquired under unfocused laser light in Figure 6.3.

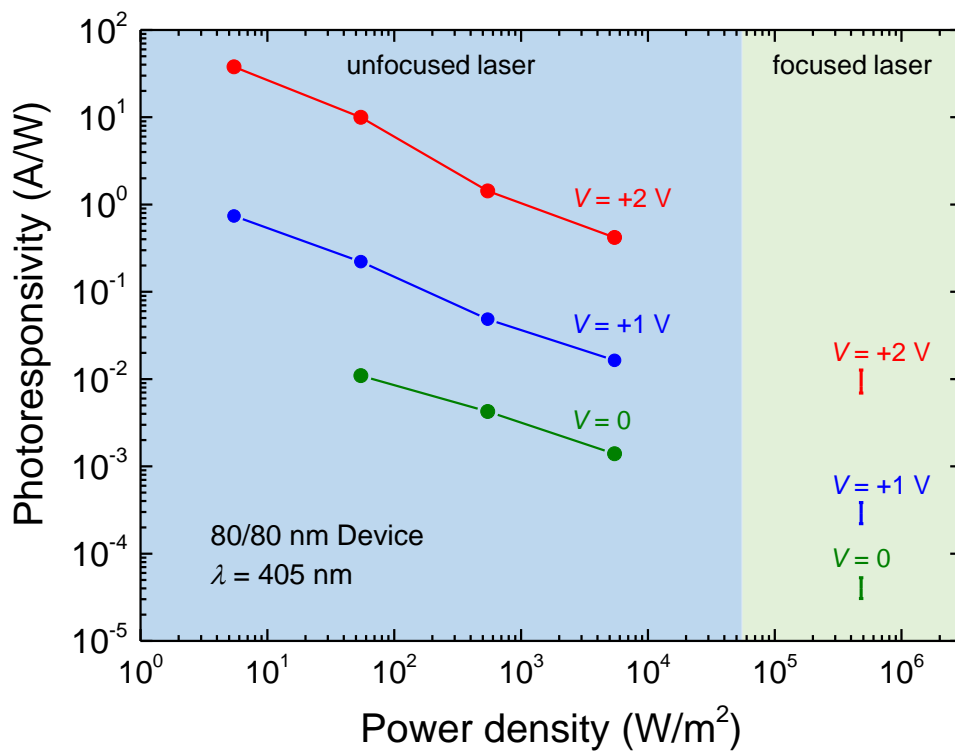


Figure 6.10 Photoresponse under unfocused/focused laser beam. Photoresponsivity versus laser power density for different applied voltages V under an unfocused (dots) and a focused (vertical lines) laser beam for a graphene contacted p -GaSe/ n -In₂Se₃ junction (80/80 nm).

The responsivity values in the focused and unfocused mode versus the laser power density are plotted in Figure 6.10. The data show that the responsivity in the focused laser mode is in line with data for the unfocused mode. In particular, the value of R tends to decrease with increasing laser power due to the increase in carrier recombination rate for increasing densities of photogenerated carriers.²⁵⁻²⁸ Although the behaviour of junctions with different layer thickness is qualitatively similar, in the thinner junctions the photoresponsivity becomes more symmetric with respect to a reversal of bias polarity (Figure 6.6).

In general, the photocurrent can be non-uniform in the plane of the junction, revealing hot spots of photoresponse. These can arise not only from the non-uniformity of the individual layers, but also from their interlayer coupling, which can vary in the layer plane due to defects and/or surface roughness, and a non-uniform spatial distribution of dopants at each interface. Thus, the relative contribution of the three vdW interfaces (*e.g.* GaSe/In₂Se₃, GaSe/graphene and In₂Se₃/graphene) to a photocurrent map can vary from device to device (Figures 6.5, 6.6 and 6.9). Figure 6.11 illustrates a junction in which the dominant contribution to the photocurrent arises from a large overlapping area between GaSe and graphene. Figure 6.11a shows the bias-dependence of the photocurrent under focused laser excitation of the junction (inset of Figure 6.11a). As the carrier density of In₂Se₃ is much larger than GaSe, the depletion region extends primarily in the *p*-GaSe layer and is negligibly small in *n*-In₂Se₃. Similarly, we expect a charge redistribution at the GaSe/graphene interface, leading to the formation of a GaSe/graphene Schottky contact. The separation of

photogenerated carriers at the GaSe/graphene interface generates a photocurrent with opposite sign to that of the pn -junction at $V = 0$ (Figure 6.11b) and same sign in forward and reverse bias (Figures 6.11c and 6.11d). For this junction, it can be seen that the photocurrent signal is observed outside the region of overlap between the two graphene layers, where the electric field should be effectively zero. This current can arise from a non-uniform electric field potential in the layer plane and a temperature gradient induced by non-uniform heating under the focused laser beam through the photo-thermoelectric effect^{8,222}.

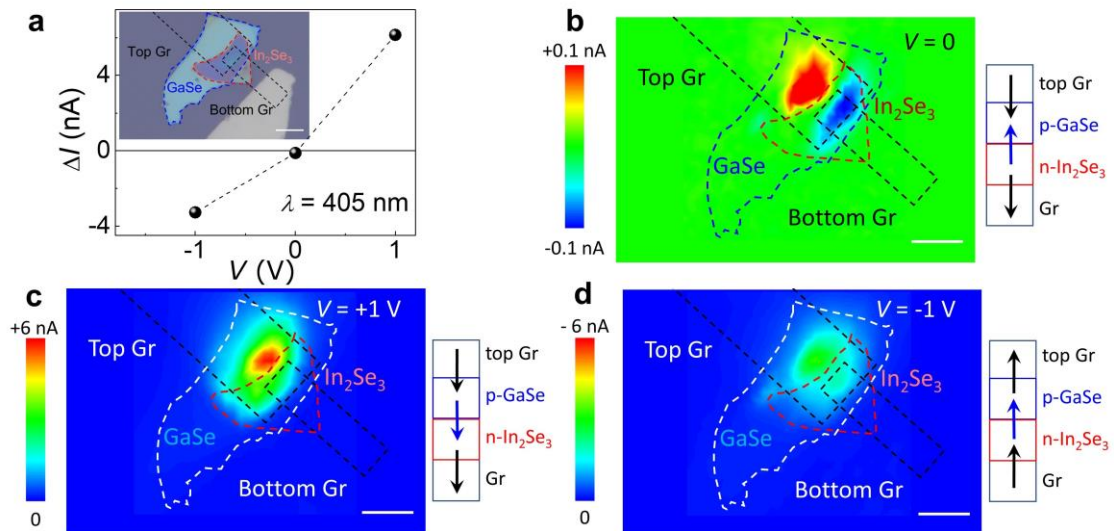


Figure 6.11 Schottky contacts in graphene-contacted p -GaSe/ n -In₂Se₃ heterojunctions. (a) Room temperature ($T = 300$ K) photocurrent (ΔI) versus V under a focused laser beam ($\lambda = 405$ nm and $P_i = 5 \mu\text{W}$) for a junction (thickness of In₂Se₃/GaSe $\sim 60/40$ nm). The data correspond to the largest value of ΔI at each V . Inset: optical image of the device. Scale bar: 10 μm . (b-d) Room temperature ($T = 300$ K) photocurrent (ΔI) maps at (b) $V = 0$, (c) +1 V and (d) -1 V. The laser beam ($\lambda = 405$ nm and $P_i = 5 \mu\text{W}$) has a spot size of about 1 μm . Scale bar: 10 μm . The right insets in part b-c-d illustrate the direction of the current across the three interfaces of the heterostructure.

In summary, these photodetectors enable an efficient collection of photo-generated carriers resulting into a high photoresponsivity. Bulk junctions are more preferable for photodetection as the dark current is lower in both forward and reverse bias, leading to a large detectivity. In reverse bias, the low dark current indicates a small leakage current due to negligible thermal excitation of carriers across the bandgaps of GaSe and In₂Se₃; in forward bias, the low dark current suggests instead a small recombination current. The mechanisms for photodetection in forward bias and the recombination of carriers are further examined in the following section.

6.5 Bias-dependent carrier recombination

We investigated the recombination of carriers by conducting electroluminescence (EL) and PL experiments under an applied voltage. No EL signal was detected in these junctions. However, a PL signal from both GaSe and In₂Se₃ was measured and found to be sensitive to the applied bias. Figure 6.12a shows the RT PL spectra at $V = 0$ for the junction of Figures 6.3 and 6.9. The PL spectrum comprises a weak band edge emission from the In₂Se₃ (band I) and GaSe (band III) layers, and a broad, structured emission (band II) centred at around 1.8 eV, at energies between band I and III, with amplitude that tends to saturate with increasing laser power. This emission is spatially localized (see micro-PL imaging in Figure 6.12b), indicative of an extrinsic carrier recombination in GaSe.

The energy peak position of band II does not reveal any significant shift with the applied bias. However, the intensity of this band is modulated by the applied

voltage, reaching a maximum at $V \sim 1.5$ V (Figures 6.12c and 6.12d). As V increases, the built-in electric field at the $\text{In}_2\text{Se}_3/\text{GaSe}$ interface decreases and electron-hole recombination becomes more favourable. On the other hand, as V increases, the electric field at the graphene/ GaSe interface also increases, thus causing a bias-induced quenching of the PL emission at large V . The quenching of the PL emission over a wide range of biases is pronounced ($\sim 100\%$), supporting an effective charge separation and light-current conversion at the $\text{In}_2\text{Se}_3/\text{GaSe}$ and $\text{GaSe}/\text{graphene}$ interfaces.

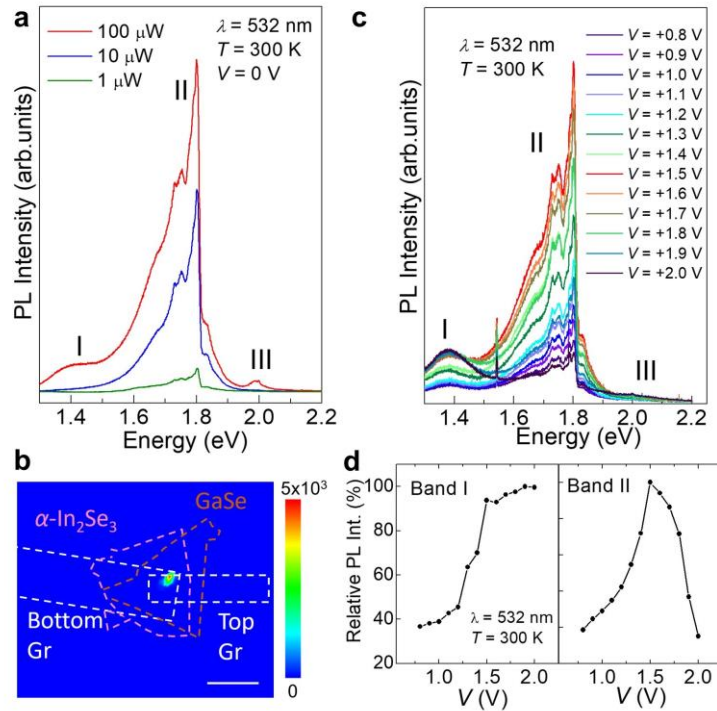


Figure 6.12 Bias-dependent photoluminescence. (a) Photoluminescence (PL) spectra of the $p\text{-GaSe}/n\text{-In}_2\text{Se}_3$ photodetector shown in Figures 6.3 and 6.9 for different excitation powers, showing three main bands: band I, II and III. The PL emission arises from a localized region of the junction, as probed by the PL intensity map in part (b). Scale bar: 10 μm . (c) PL spectra of the photodetector for different voltages V . (d) V -dependence of the PL intensity of bands I and II ($T = 300$ K, $\lambda = 532$ nm).

We note that the bias-dependence of the PL emission due to In₂Se₃ (band I, Figure 6.12d) is slightly different. Although the initial increase of PL intensity with increasing V is observed also in this case, this is then followed by a saturation of the PL signal at large V . We assign this different behaviour to the larger carrier concentration in In₂Se₃ ($n \sim 10^{17} \text{ cm}^{-3}$) compared to that in GaSe ($p \sim 10^{13} \text{ cm}^{-3}$). Combined with a large dielectric contrast of In₂Se₃ ($\epsilon_{\text{In}_2\text{Se}_3} \sim 17$ and $\epsilon_{\text{GaSe}} \sim 6$),^{223,224} this leads to more effective screening of the electric field in In₂Se₃.

While the separation of charges at three interfaces can explain both the photoresponse and carrier recombination, the origin of band II remains unclear. In particular, the observation of this band is suggestive of a recombination channel that is not beneficial for photodetection. Theoretical studies of the energetics of crystal defects in GaSe have shown that acceptor levels due to Ga vacancies (V_{Ga}) have energies at approximately 0.2 eV above the valence band (VB) edge, while interstitial Ga (Ga_i) create donor levels at 0.2 eV below the conduction band (CB) edge.²²⁵ Large scale defects, including clusters of point defects and cracks/local stacking faults, can also form as the result of mechanical stress applied to a crystal during fabrication.²²⁶ These can induce localized regions with enhanced PL emission in the range 1.7–2.0 eV,²²⁷ as observed in our micro-PL imaging studies (Figure 6.12b). Similar, but broader extrinsic PL emissions can be generated via controlled thermal annealing of individual flakes of GaSe: A focused laser beam with a diameter of $\sim 1 \mu\text{m}$, power $P_i > 0.5 \text{ mW}$ and $\lambda = 532 \text{ nm}$ was used to anneal a GaSe flake for a time interval in the range $\Delta t = 10 \text{ s}$ to 60 s . After each annealing, the sample was allowed to cool down

for approximately 20 s before conducting PL and Raman measurements. All measurements were taken on the same point of the flake at $T = 300$ K. Figure 6.13 shows the PL (a) and Raman (b) spectra of a GaSe flake before and after laser annealing at $T = 300$ K. The time for each curve shows the total annealing time at the given laser power. Following a prolonged laser annealing, the band edge PL emission weakens and is replaced by a broad PL emission peaked at ~ 1.7 eV. The strengthening of the Raman line at 255 cm^{-1} following the annealing is attributed to the local photo-oxidation of the flake due to the formation of amorphous selenium (α -Se).²²⁸

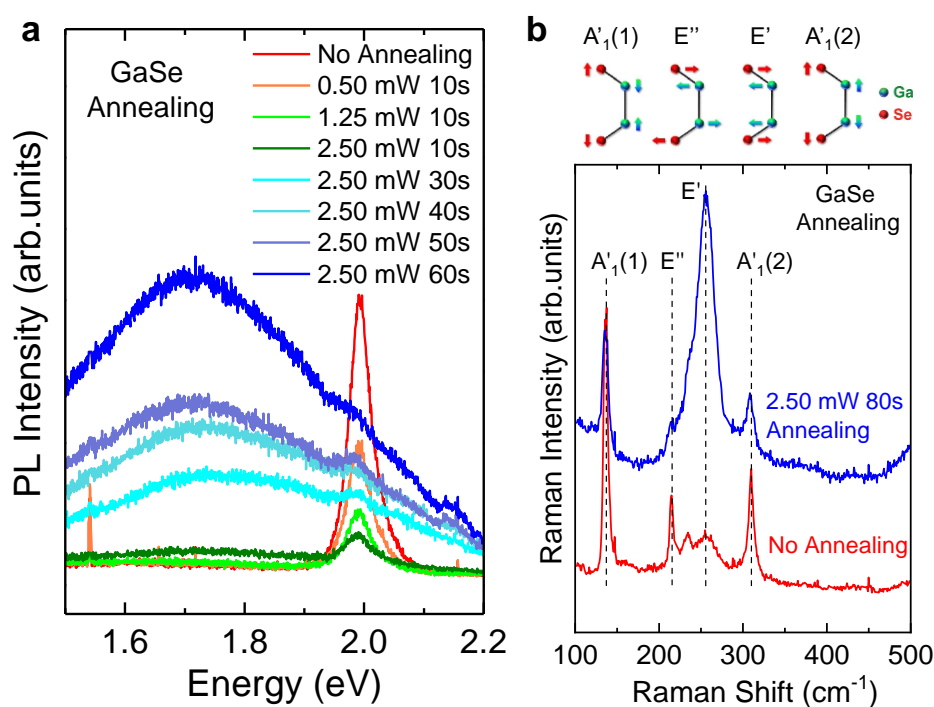


Figure 6.13 Laser annealing of GaSe flakes. (a) PL spectra of a GaSe flake before and after laser annealing in air with different powers/annealing times ($T = 300$ K, $\lambda = 532$ nm). (b) Atomic displacements of GaSe vibrational modes and Raman spectra of a GaSe flake before and after annealing ($T = 300$ K, $\lambda = 532$ nm). The enhancement of the E' peak is attributed to the photo-oxidation of GaSe. The atomic displacements are reproduced from ref.^{229,230}.

The sensitivity of these junctions to charges trapped by defects of GaSe indicates that efficient optoelectronic devices based on this material require an optimization of the fabrication process. A crucial requirement is the in-plane spatial homogeneity of the layers, which can affect interlayer coupling and band alignments. Furthermore, GaSe can oxidize in air leading to morphological and chemical changes of its surface. Thus, an effective passivation strategy should also be adopted to mitigate these effects.

6.6 Summary

In conclusion, we have exploited the vdW interfaces of the graphene/*p*-GaSe/*n*-In₂Se₃/graphene heterostructure to fabricate high-responsivity UV photodetectors. Their operation exploits the optical absorption of the metal chalcogenide layers and the built-in potential at the three vdW interfaces of the heterostructure. The junctions can have high photoresponsivity and low dark current in both forward and reverse biases, and without any externally applied bias. Thus, these multi-layer vdW heterostructures could play a crucial role in the development of high performance 2D semiconductor-based devices for a broad range of applications. Scanning photocurrent microscopy revealed that the contribution of the three interfaces to the overall responsivity can differ from device to device due to the non-uniformity of the layers and their coupling. For example, defects can act as recombination centres in GaSe leading to a photoluminescence emission that is modulated by the applied voltage. Thus, these devices could be improved by

optimization of their fabrication to reduce the contribution of crystal defects and optimize interlayer coupling. Further optimization of the layer thickness and doping, and scalable growth of the layers could also lead to optimal designs for even larger responsivity and detectivity, offering an alternative to conventional UV detection technologies.

Chapter 7

Room-temperature magnetoresistance in magnetic tunnel junctions

The magnetic tunnel junction (MTJ) is widely used in memory technologies and sensing applications.^{231,232} In particular, MTJs based on two-dimensional (2D) van der Waals (vdW) heterostructures offer unprecedented opportunities for low power consumption and miniaturization of spintronic devices. However, their operation at room temperature remains a challenge. In this chapter, we report a large tunnel magnetoresistance (TMR) of up to 85% at room temperature ($T = 300$ K) in vdW MTJs based on a thin (< 10 nm) semiconductor spacer WSe_2 layer embedded between two Fe_3GaTe_2 electrodes with intrinsic above-room-temperature ferromagnetism. The TMR in the MTJ increases with decreasing temperature up to 164% at $T = 10$ K. The demonstration of TMR in these ultra-thin MTJs at room temperature, as well as other similar MTJs under investigation, opens a realistic and promising route for next-generation spintronic applications beyond the current state of the art.

The Fe_3GaTe_2 bulk crystals were grown by Prof. Haixin Chang at Huazhong University of Science and Technology, China. The exfoliated layers and devices were fabricated by Dr Wenkai Zhu. Transport measurements and optical studies were conducted by myself and Dr Hailong Lin at the Institute of Semiconductors, Chinese Academy of Sciences. The results presented in this chapter were published in *Chinese Physics Letters* **39**, 128501 (2022).

7.1 Introduction

Magnetic tunnel junctions (MTJs) with large tunnel magnetoresistance (TMR) play an important role in many technologies ranging from magnetic-field sensing and non-volatile magnetic random-access memories (MRAM) to programmable spin logic devices.²³³⁻²³⁶ Traditional MTJs normally consist of three-dimensionally bonded ferromagnetic metals and non-magnetic wide-gap oxides, such as Fe/MgO/Fe and NiFe/TaO/Al₂O₃/Co.²³⁷⁻²⁴⁰ Different from covalently bonded multilayer systems, van der Waals (vdW) heterostructures with atomically sharp and clean interfaces offer opportunities to build high-quality junctions without the requirement of lattice matching.^{64,209} Specifically, the recent discovery of magnetic two-dimensional (2D) vdW materials, such as Cr₂Ge₂Te₆¹³⁹, CrI₃^{138,241}, Fe₃GeTe₂^{18,150} and Fe₅GeTe₂¹⁴³ not only provide platforms for studies of novel physics phenomena, but also offer promising application prospects for 2D electronic devices where the spin is used as an extra degree of freedom.^{142,149,242-252}

Although the Curie temperature (T_C) of 2D magnets can be tuned to room temperature by electrostatic gating¹⁸, high-pressure²⁵³ or interlayer magnetic coupling²⁵⁴, the room temperature operation of vertical MTJs under these conditions remains a challenge, hindering prospects for future applications.²⁵⁵ On the other hand, there is the ambition for all-2D room-temperature MTJs to be manufactured for production within the next decade.²³³ This could be facilitated by the recent discovery of the vdW crystal Fe₃GaTe₂ that has a high saturation magnetic moment, robust large

perpendicular magnetic anisotropy (PMA), and Curie temperature T_C of up to 380 K.¹³⁰

In this chapter, we use Fe_3GaTe_2 as the ferromagnetic electrodes in an all-vdW MTJ. The tunnel barrier of the MTJ is the transition-metal dichalcogenide (TMDC) semiconductor WSe_2 . Due to its tunable bandgap and long spin diffusion length, WSe_2 is suitable for the construction of 2D magnetic devices, such as MTJs^{250,256} and spin field-effect transistors (FETs).²⁵⁷ Moreover, the magnetoresistance of MTJs can be tuned by the thickness of the WSe_2 spacer layer through the spin filtering effect.²⁵⁰ Here, we describe the properties of the Fe_3GaTe_2 layers and of the $\text{Fe}_3\text{GaTe}_2/\text{WSe}_2/\text{Fe}_3\text{GaTe}_2$ MTJs. Preliminary results are also presented for $\text{Fe}_3\text{GaTe}_2/\text{GaSe}/\text{Fe}_3\text{GaTe}_2$ MTJs.

7.2 Anomalous Hall effect in Fe_3GaTe_2

High-quality vdW ferromagnetic crystal Fe_3GaTe_2 is grown by the self-flux method and has a hexagonal structure of space group $P6_3/mmc$ with lattice parameters $a = b = 3.9860 \text{ \AA}$ and $c = 16.2290 \text{ \AA}$ ($\alpha = \beta = 90^\circ$, $\gamma = 120^\circ$).¹³⁰ In the Fe_3GaTe_2 crystal, the Fe_3Ga heterometallic slab is sandwiched between two Te layers, and the vdW gap is between two adjacent Te atoms. In Figure 7.1a, two inequivalent Fe sites are distinguished by brown and blue balls, respectively. The slabs of Fe_3GaTe_2 are stacked along the c -axis with an interlayer spacing of $\sim 0.78 \text{ nm}$.¹³⁰ As the magnetic moment of Ga and Te atoms in Fe_3GaTe_2 are negligible, the ferromagnetism of Fe_3GaTe_2 mainly comes from the $3d$ -orbital electrons in the Fe atoms.¹³⁰ An

exfoliated 10-nm-thick Fe_3GaTe_2 flake was used to fabricate a Hall-bar (Figure 7.1b) and investigate the magnetic properties of Fe_3GaTe_2 . The thickness of Fe_3GaTe_2 is measured by atomic force microscopy (AFM) (Figure 7.1c upper-left inset).

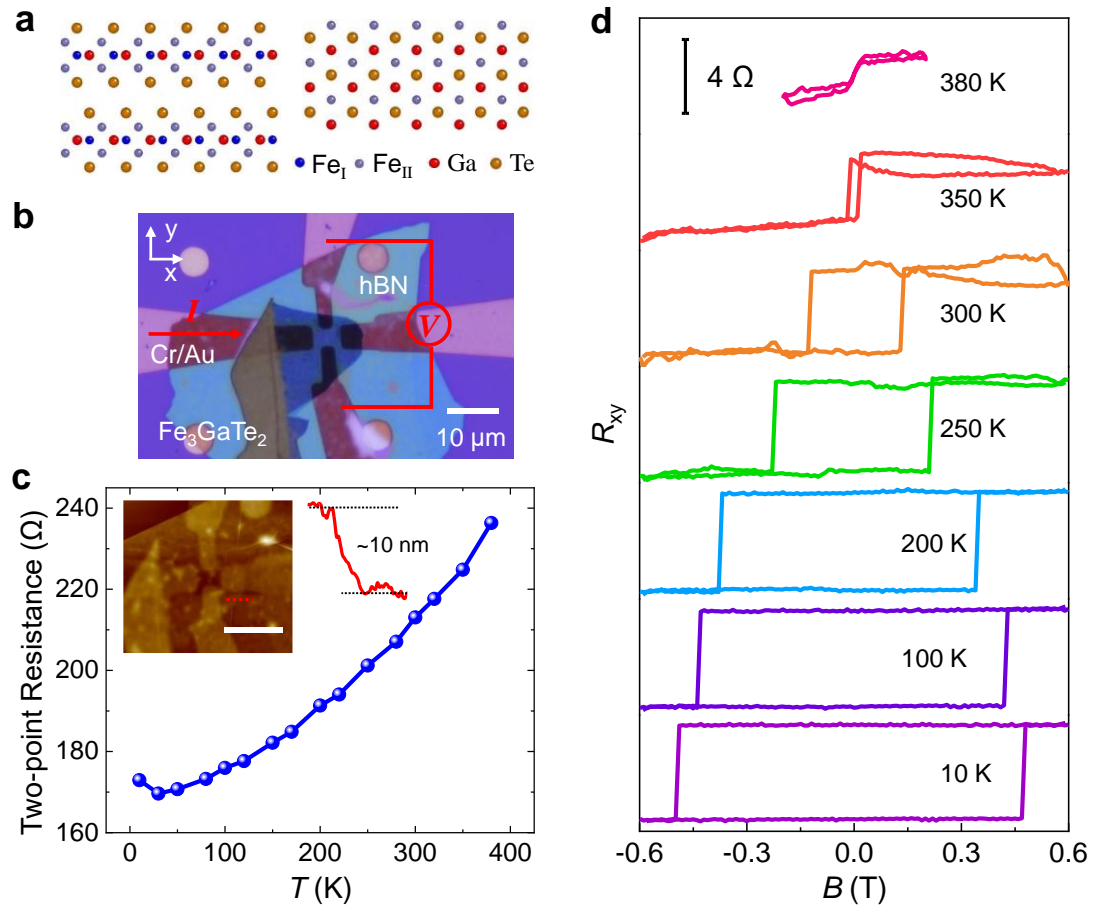


Figure 7.1 Anomalous Hall effect in few-layer Fe_3GaTe_2 . (a) Side (left) and top views (right) of the crystal structure of Fe_3GaTe_2 . (b) The optical image of a Fe_3GaTe_2 Hall-bar device capped by hBN. Scale bar: 10 μm . The direction of the current and the electrodes used in the Hall measurements are shown in red. (c) Two-point resistance versus temperature from 10 to 380 K. Upper-left inset: AFM image and height profile of the Fe_3GaTe_2 . Scale bar: 10 μm . (d) Hall resistance R_{xy} versus perpendicular magnetic field (B) of a 10-nm-thick Fe_3GaTe_2 at different temperatures ranging from 10 to 380 K. The bias current I_{xx} is fixed at 10 μA .

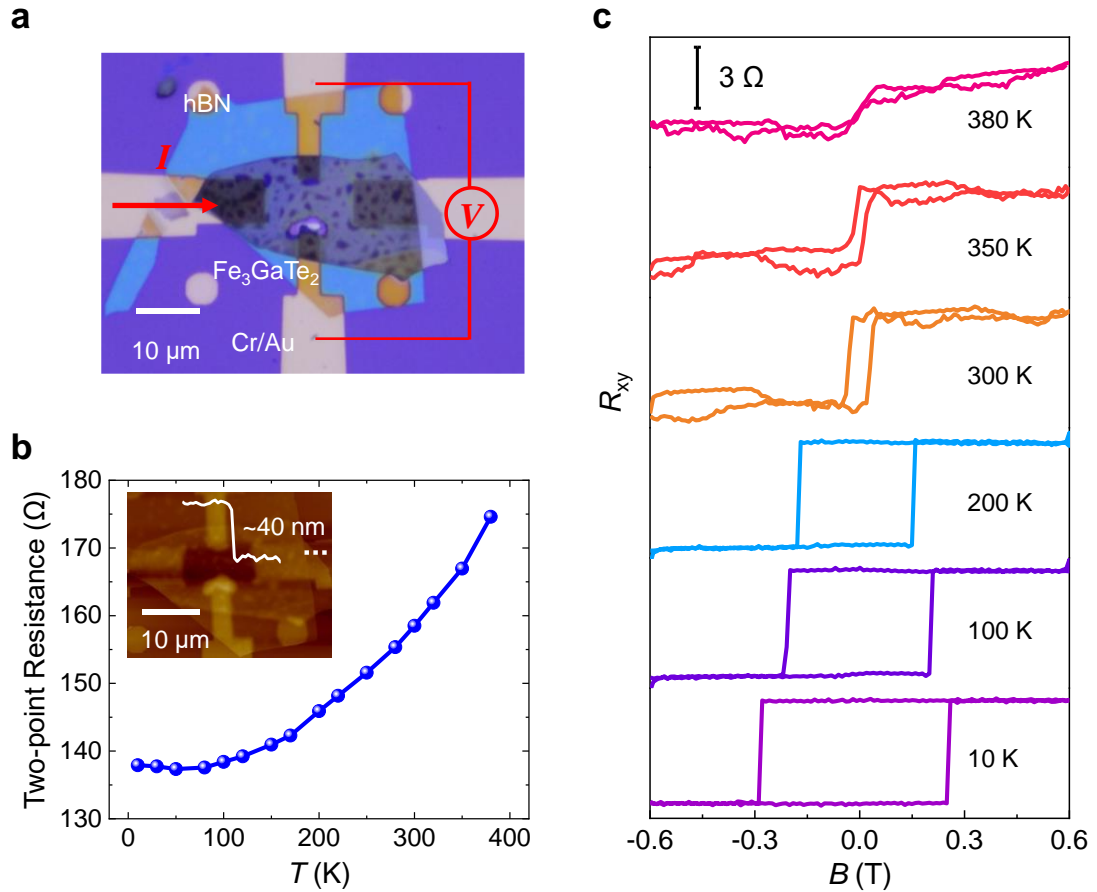


Figure 7.2 Anomalous Hall effect in bulk Fe_3GaTe_2 . (a) The optical image of a thick (40 nm) Fe_3GaTe_2 Hall-bar device capped by hBN. Scale bar: 10 μm . The direction of the current and the electrodes used in the Hall measurements are shown in red. (b) Two-point resistance versus temperature from 10 to 380 K. Upper-left inset: AFM image and height profile of the Fe_3GaTe_2 Hall-bar device. Scale bar: 10 μm . (c) Hall resistance R_{xy} versus perpendicular magnetic field (B) at different temperatures ranging from 10 to 380 K. The bias current I_{xx} is fixed at 10 μA .

In the anomalous Hall effect (AHE) measurements, the two-terminal resistance increases monotonically with increasing temperature, as expected for a metallic layer (Figure 7.1c). Figure 7.1d depicts the temperature-dependent AHE signal R_{xy} (transverse resistance) as the perpendicular applied magnetic field B sweeps between -0.6 and $+0.6$ T. As the temperature increases from 10 to 380 K, the $R_{xy}-B$

curves display almost perfectly square-shaped hysteresis loops, indicating that the Fe_3GaTe_2 flake has strong PMA. Especially, the AHE signal of the Fe_3GaTe_2 Hall-bar is still measurable at room temperature. Due to the enhancement of the thermal fluctuations close to T_C , the coercivity also decreases monotonically with increasing temperature and nearly vanishes at 380 K. Another thicker Fe_3GaTe_2 (~ 40 nm) flake shows the same above-room-temperature T_C and a smaller coercivity (Figure 7.2). Due to the contribution of $\text{Fe}_3\text{GaTe}_2/\text{Au}$ contact resistances, although the Fe_3GaTe_2 thickness in the thick Hall bar is around 4 times that of the thin device, its two-point resistance is not 1/4 of the thin device. The high T_C , large coercivity, and robust PMA make the Fe_3GaTe_2 flake an ideal metallic ferromagnetic electrode for MTJs working at room temperature.¹³⁰

7.3 Room-temperature magnetoresistance in Fe_3GaTe_2 -based MTJs

We now focus on the fabrication and properties of the MTJ. Figures 7.3a and 7.3b show the schematic and optical image of the two-terminal MTJ. Here, two metallic Fe_3GaTe_2 ferromagnetic electrodes are separated by a non-magnetic WSe_2 spacer layer. The whole structure is capped with a hBN layer (typically 10-30 nm) to prevent degradation or oxidation once the MTJ is exposed to air. The semiconductor 2H- WSe_2 is a typical TMDC material with a hexagonal structure and space group $P6_3/mmc$, consisting of van der Waals bonded Se-W-Se layers.²⁵⁸ The bulk WSe_2 is an indirect-gap semiconductor with a bandgap of 1.20 eV, while single-layer WSe_2 has a direct bandgap of 1.65 eV.²⁵⁹ The AFM study of the MTJ indicates that the

thickness of the spacer WSe_2 layer is ~ 7 nm (around 11 layers).²⁶⁰ To distinguish the coercivities of the top and bottom ferromagnetic electrodes in the MTJs, we selected Fe_3GaTe_2 flakes with different thicknesses (~ 11 nm bottom Fe_3GaTe_2 and ~ 17 nm top Fe_3GaTe_2). The different switching fields of the top and bottom ferromagnetic layers enable the parallel and antiparallel configurations under different specific magnetic fields, corresponding to the low and high resistance states of the MTJ.²⁶¹

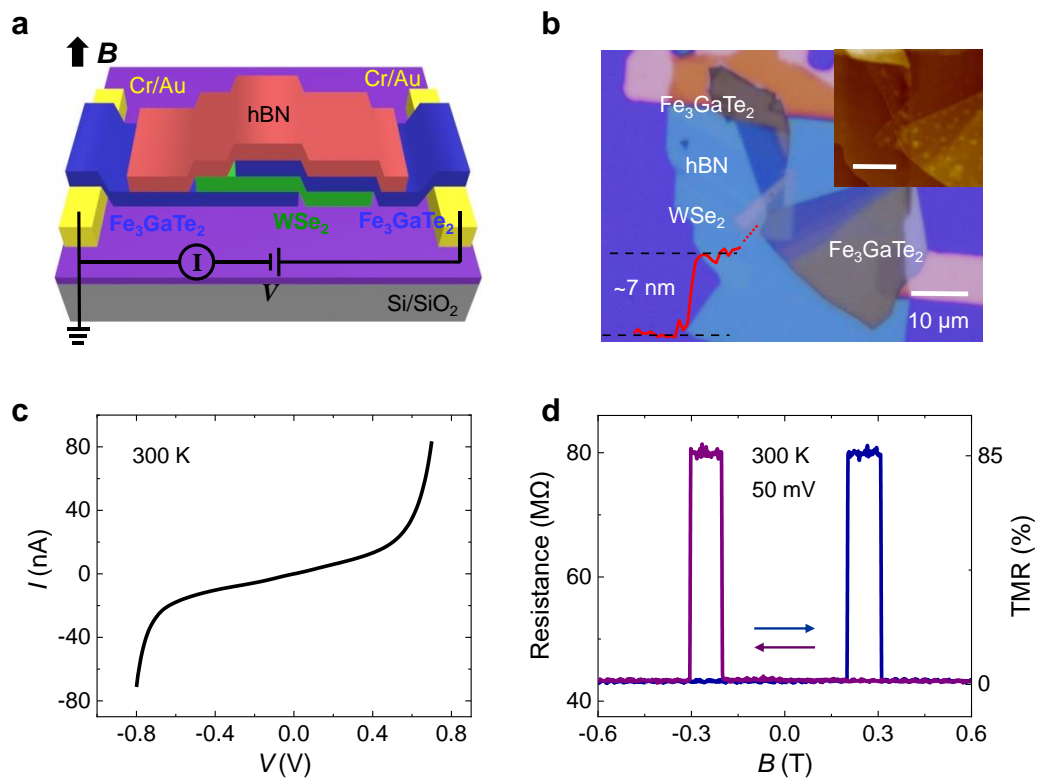


Figure 7.3 Room-temperature magnetoresistance in a $\text{Fe}_3\text{GaTe}_2/\text{WSe}_2/\text{Fe}_3\text{GaTe}_2$ magnetic tunnel junction. (a) Schematic of $\text{Fe}_3\text{GaTe}_2/\text{WSe}_2/\text{Fe}_3\text{GaTe}_2$ MTJs. (b) Optical image and AFM image (upper-right inset) of a representative $\text{Fe}_3\text{GaTe}_2/\text{WSe}_2/\text{Fe}_3\text{GaTe}_2$ (thickness 17 nm/7 nm/11 nm) heterojunction device encapsulated by a top hBN layer. Scale bar: $10\ \mu\text{m}$. The lower-left inset shows the height profile of the spacer WSe_2 layer. (c) I - V characteristics of the device at $T = 300$ K. (d) Room-temperature resistance and TMR versus perpendicular magnetic field (B) of the device at a constant bias voltage $V = 50$ mV.

Raman spectroscopy was used to characterise the Fe_3GaTe_2 and WSe_2 layers (Figures 7.4a and 7.4b). The WSe_2 layer has a room temperature photoluminescence (PL) emission centred at 1.38 eV (Figure 7.4c), in good agreement with previous experimental results.^{130,262} The preliminary studies indicate a high-quality WSe_2 spacer layer, as required to preserve the polarization of the electron as it tunnels in the MTJ.²⁴²

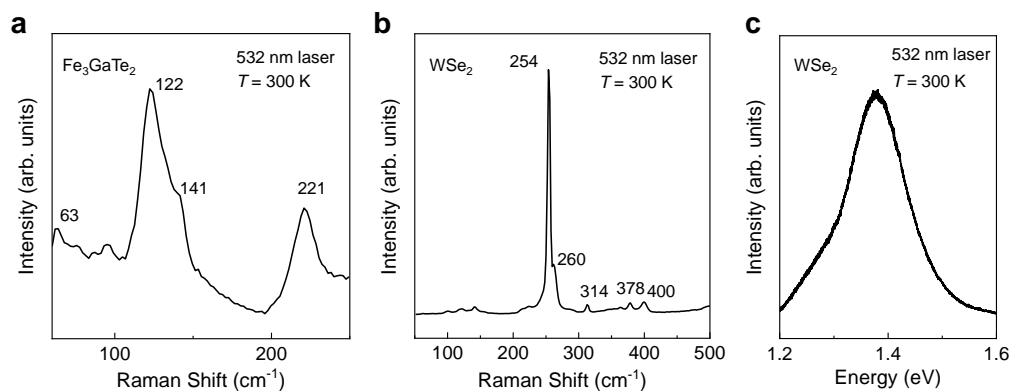


Figure 7.4 Raman and PL characterizations of Fe_3GaTe_2 and WSe_2 layers. (a) Raman spectrum of a bulk Fe_3GaTe_2 flake ($T = 300$ K, $\lambda = 532$ nm). (b) Raman spectrum of a bulk WSe_2 flake ($T = 300$ K, $\lambda = 532$ nm). (c) Photoluminescence (PL) spectrum of a bulk WSe_2 flake ($T = 300$ K, $\lambda = 532$ nm). The spectrum shows the band edge emission of WSe_2 , which is centred at about 1.38 eV.

Figure 7.3c shows a symmetric, nonlinear I - V curve of the device, which point to a typical tunnelling behaviour.^{249,263} By applying a constant bias voltage ($V = 50$ mV) and sweeping the perpendicular magnetic field (B), we observed a sharp jump of the resistance from low (R_P) to high-resistance state (R_{AP}) at $B = 0.20$ T (Figure 7.3d). With further increasing B to 0.31 T, the resistance jumps back to the low-resistance state. Symmetric resistance jumps are also observed for sweeping B from positive to negative values. The distinct low- and high-resistance states correspond to the

magnetization of the two Fe_3GaTe_2 layers in parallel ($\downarrow\downarrow$ or $\uparrow\uparrow$) and antiparallel ($\downarrow\uparrow$ or $\uparrow\downarrow$) magnetization configurations, respectively. In the parallel configuration, spin-dependent tunnelling occurs between the same spin states, representing R_P with the product of the DOS of the majority (D_\uparrow) and minority (D_\downarrow) spins as $1/R_P \propto (D_\uparrow \times D_\uparrow) + (D_\downarrow \times D_\downarrow)$.²⁵⁶ In the antiparallel configuration, R_{AP} is conversely determined by the cross product of the DOS with different spin states as $1/R_{AP} \propto 2D_\uparrow \times D_\downarrow$, leading to a larger R_{AP} for MTJs under low bias voltages.²⁵⁶ At $V = 50$ mV and $T = 300$ K, the R_P and R_{AP} of the junction are $43.3 \text{ M}\Omega$ and $80.4 \text{ M}\Omega$, respectively. The corresponding $\text{TMR} = (R_{AP} - R_P)/R_P$ is 85 %, even higher than that of some reported conventional MTJs working at room temperature, such as $\text{Fe}/\text{Al}_2\text{O}_3/\text{Fe}$ ($\text{TMR} = 18 \%$)²⁶⁴ and $\text{Fe}/\text{MgO}/\text{Fe}$ ($\text{TMR} = 30\%$)²⁶⁵.

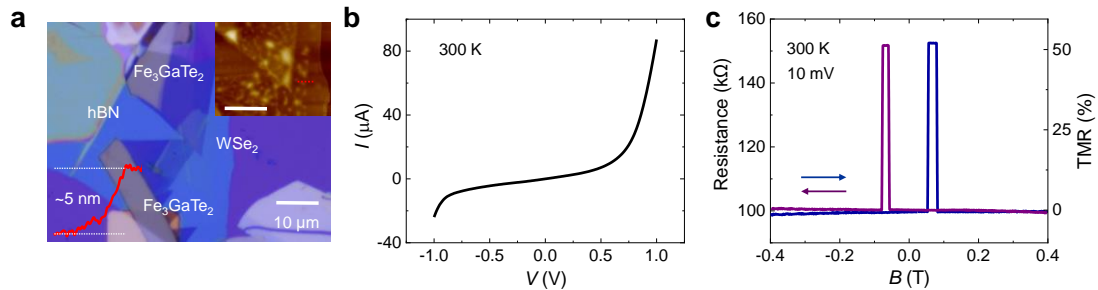


Figure 7.5 Room-temperature magnetoresistance in a MTJ with a thin (5 nm) spacer layer. (a) Optical image and AFM image (upper right inset) of another $\text{Fe}_3\text{GaTe}_2/\text{WSe}_2/\text{Fe}_3\text{GaTe}_2$ (thickness 9 nm/5 nm/8 nm) MTJ device. Scale bar: 10 μm . Lower-left inset: the height profile of the spacer WSe_2 layer. (b) I – V characteristics of the device at $T = 300$ K. (c) Room-temperature resistance and TMR versus B at 10 mV bias.

Similar results were obtained in another device with a thin (5 nm) spacer layer displaying a TMR of 53% at room temperature (Figure 7.5). The room-temperature

TMR in our devices is an important achievement, filling a gap in the current literature on TMR in all-2D vdW MTJs.

7.4 Temperature-dependent magnetoresistance

Figures 7.6a and 7.6b show the TMR– B curves measured at various temperatures of the device shown in Figure 7.3b. A TMR of 164% is observed at $T = 10$ K, while another device shown in Figure 7.5a exhibits a larger TMR of 210% at the same temperature (Figure 7.7). With increasing temperature, the magnitude of the TMR decreases and vanishes above T_C (Figure 7.6c). The spin polarization is proportional to the magnetization and decreases with increasing temperature,²⁶⁶ thus leading to a smaller TMR. Moreover, due to the reduction of perpendicular anisotropic energy and the enhancement of thermal energy, the coercivity of Fe_3GaTe_2 decreases with increasing temperature as well.²⁶⁶ This is reflected in the reduction of the critical magnetic switching field of the MTJ in Figures 7.6a and 7.6b. Interestingly, some TMR– B curves in Figure 7.6a are asymmetric, indicating that the coercivity of Fe_3GaTe_2 can be different at positive and negative magnetic field. This can be attributed to the defect-related pinning effect, which is weakened at high temperatures (Figure 7.6b).²⁶⁷ The TMR can be defined as $\text{TMR} = 2P^2/(1 - P^2)$, where $P = (D_\uparrow - D_\downarrow)/(D_\uparrow + D_\downarrow)$ denotes the spin polarization at the Fermi-level (E_F) for the injector and detector Fe_3GaTe_2 electrodes.²⁶⁸ A room-temperature spin polarization P of 55 % is derived from a value of the TMR of 85%. As shown in Figure 7.6d, the estimated temperature-dependence of the spin polarization can be fitted well by a

power law given by $P = P_0(1-T/T_C)^\gamma$, where P_0 is the spin polarization at 0 K and γ is a material-dependent constant that can be fitted to $\gamma = 0.137$.^{141,269} Our fitting results also indicate that $T_C = 400$ K, which is close to that obtained in Figure 7.6b.

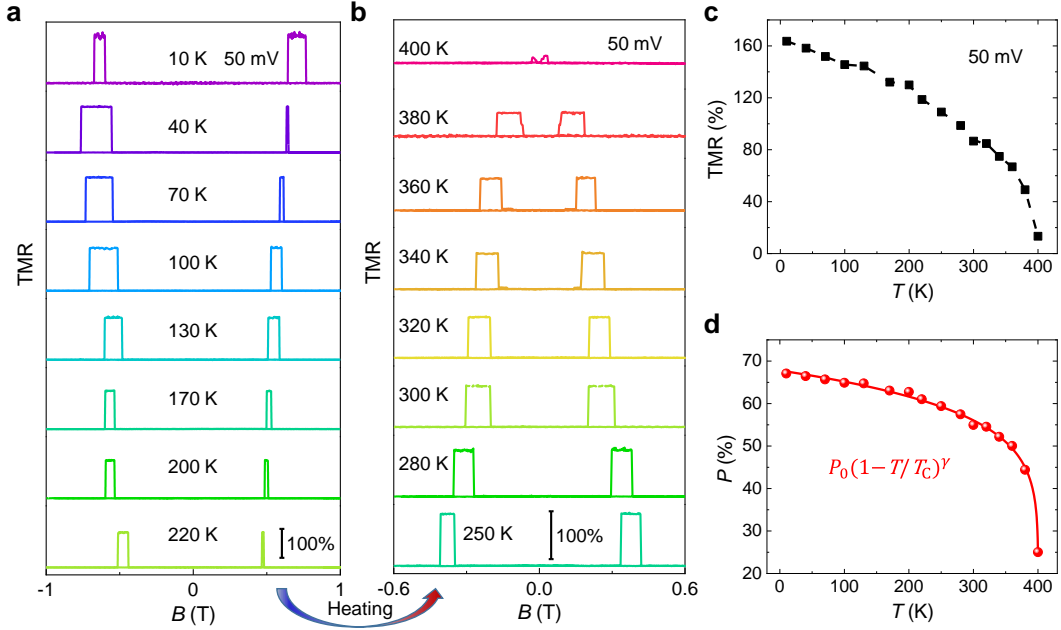


Figure 7.6 Temperature-dependent magnetoresistance in a MTJ. (a-b) TMR versus B of the device (17 nm/7 nm/11 nm $\text{Fe}_3\text{GaTe}_2/\text{WSe}_2/\text{Fe}_3\text{GaTe}_2$, optical image of the junction shown in Figure 7.3b) at different temperatures ranging from 10 to 400 K. (c) TMR versus temperature of the device shown in Figure 7.3b at $V = 50$ mV. The values of TMR are derived from (a-b). (d) Spin polarization (P) versus temperature of the device. The fitting curve is the function $P = P_0(1-T/T_C)^\gamma$, where $P_0 = 68 \pm 2$ %, $T_C = 400 \pm 2$ K, $\gamma = 0.137 \pm 0.003$.

Figures 7.7a and 7.7b show the TMR curves of another device shown in Figure 7.5a measured at various temperatures. An extremely large TMR of 210% in the device is observed at $T = 10$ K. Same as the device in Figure 7.6, the magnitude of the TMR decreases with increasing temperature and vanishes above T_C (Figure 7.7c). Interestingly, the TMR of this device (210%, 10K) is larger than that of the device in

Figure 7.6 (164%, 10K) at a low temperature, but the TMR of this device (53%, 300 K) is smaller than that of the device in Figure 7.6 (85%, 300K) at room temperature, which indicates that the TMR of this device decays more significantly with increasing temperature. This is caused by the difference in T_C of Fe_3GaTe_2 between the two devices. By fitting the measured polarization by the power-law $P = P_0(1-T/T_C)^\gamma$ (Figure 7.7d), we derive a $T_C = 357$ K of Fe_3GaTe_2 in this device, which is lower than that of the device in Figure 7.6 ($T_C = 400$ K). From the literature¹³⁰, we know that the T_C of Fe_3GaTe_2 decreases monotonically with decreasing thickness. Thinner Fe_3GaTe_2 layers (~ 8 nm bottom layer and ~ 9 nm top layer) in this device lead to a lower T_C , resulting in a smaller TMR at room temperature.

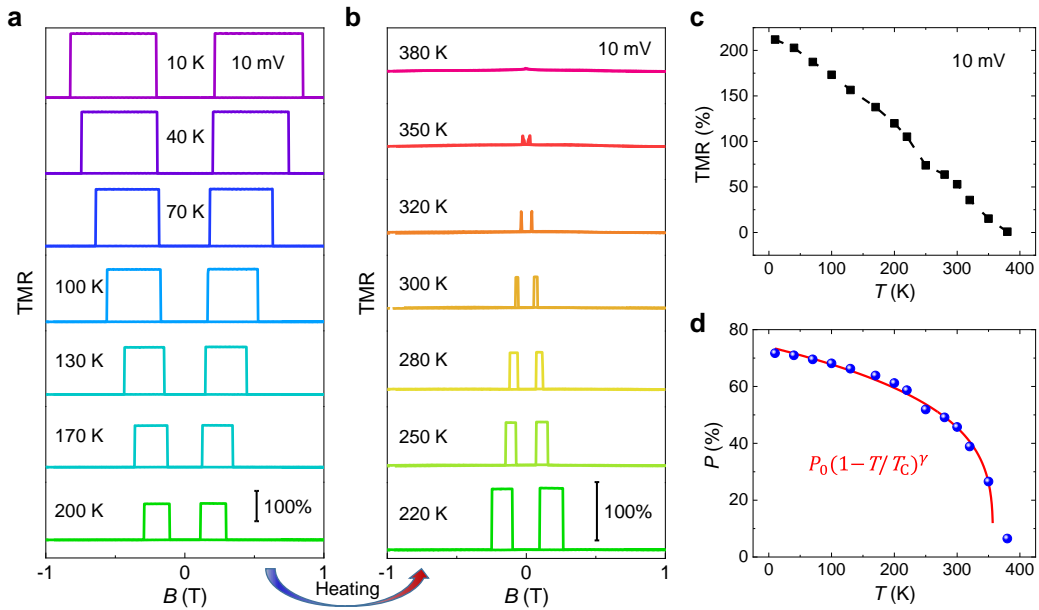


Figure 7.7 Temperature-dependent magnetoresistance in a MTJ with a thin (5 nm) spacer layer. (a-b) TMR versus B of another device shown in Figure 7.5a at different temperatures ranging from 10 to 380 K. (c) TMR versus temperature of the device at $V = 10$ mV. The values of TMR are obtained from parts (a-b). (d) Spin polarization (P) versus temperature of the device. The fitting curve is the function $P = P_0(1-T/T_C)^\gamma$, where $P_0 = 74 \pm 2$ %, $T_C = 357 \pm 5$ K, $\gamma = 0.26 \pm 0.03$.

7.5 Magnetoresistance in $\text{Fe}_3\text{GaTe}_2/\text{GaSe}/\text{Fe}_3\text{GaTe}_2$ MTJs

In this section, we present an investigation of Fe_3GaTe_2 -based MTJs in which the tunnel barrier is based on the vdW semiconductor GaSe. Figure 7.8a shows a typical $\text{Fe}_3\text{GaTe}_2/\text{GaSe}/\text{Fe}_3\text{GaTe}_2$ heterojunction. The AFM study indicates that the thickness of the spacer GaSe layer is ~ 8 nm (inset of Figure 7.8a). By applying a constant bias voltage ($V = 0.5$ V) and sweeping the perpendicular magnetic field (B), we observed a room-temperature magnetoresistance of 36%, which is similar to that measured in $\text{Fe}_3\text{GaTe}_2/\text{WSe}_2/\text{Fe}_3\text{GaTe}_2$ MTJs, see Figure 7.8b. We observed similar behaviours in other MTJs based on GaSe layers of different thickness (Table 7.1).

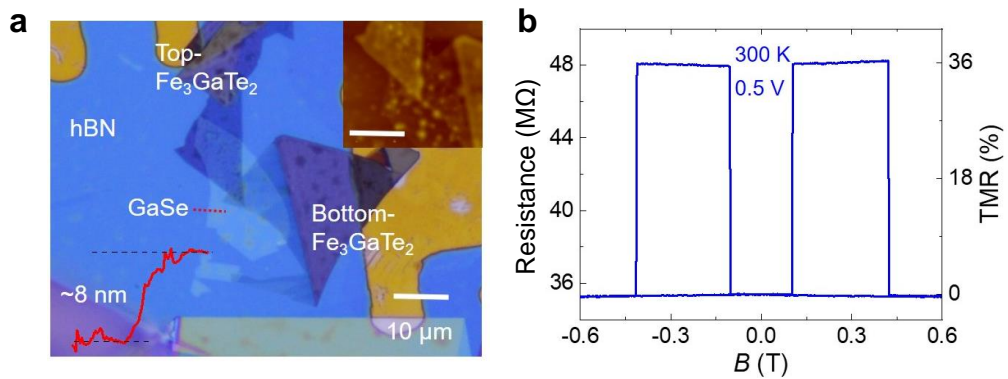


Figure 7.8 Room-temperature magnetoresistance in a $\text{Fe}_3\text{GaTe}_2/\text{GaSe}/\text{Fe}_3\text{GaTe}_2$ MTJ. (a) Optical image and AFM image (upper-right inset) of a $\text{Fe}_3\text{GaTe}_2/\text{GaSe}/\text{Fe}_3\text{GaTe}_2$ (thickness 20 nm/8 nm/12 nm) heterojunction device encapsulated by a top hBN layer. Scale bar: $10 \mu\text{m}$. The lower-left red line shows the height profile of the GaSe layer. (b) Room-temperature resistance and TMR versus perpendicular magnetic field (B) of the device at $V = 0.5$ V.

The TMR– B curves of the $\text{Fe}_3\text{GaTe}_2/\text{GaSe}/\text{Fe}_3\text{GaTe}_2$ MTJ under different bias voltages are shown in Figures 7.9a ($T = 10$ K) and 7.9b ($T = 300$ K). As the positive voltage increases, the TMR first increases and then decreases, and reaches a

maximum value at $V = +0.5$ V. A similar dependence is observed in the negative voltage range with a maximum TMR at $V = -0.5$ V. To better understand the variation of the TMR with bias, we measured the I - V curves of the devices in parallel and antiparallel states, respectively (Figure 7.9c). The TMR- V curves at different temperatures are shown in Figure 7.9d. Each curve exhibits an M-shaped dependence on the TMR on V . In Figure 7.9d, the TMR- V curves overlap with the data (circles) extracted from Figures 7.9a and 7.9b. The investigation of this characteristic voltage dependence of the TMR is ongoing and involves an understanding of the band structures of GaSe and Fe_3GaTe_2 , and the dependence of magneto-tunnelling on the applied voltage.

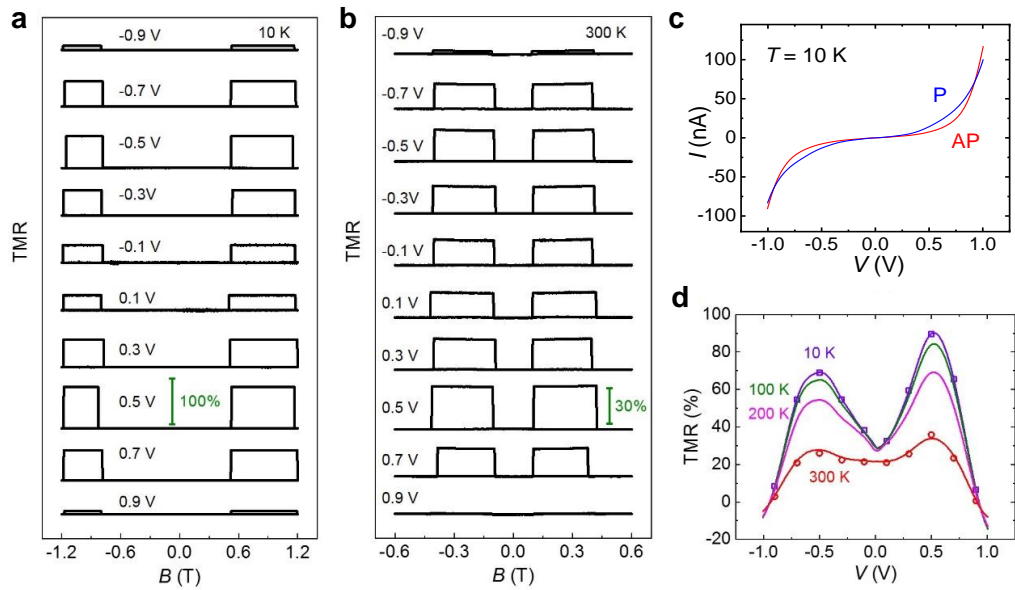


Figure 7.9 Bias-dependent magnetoresistance in a $\text{Fe}_3\text{GaTe}_2/\text{GaSe}/\text{Fe}_3\text{GaTe}_2$ MTJ. (a-b) TMR versus B of the device at different bias voltages ranging from -0.9 V to +0.9 V at (a) $T = 10$ K and (b) $T = 300$ K. (c) I - V curves of the device in parallel (blue) and antiparallel (red) states at $T = 10$ K. (d) The corresponding TMR as a function of V at different temperatures ranging from 10 K to 300 K. The hollow symbols are extracted from the TMR- B curves in Figures (a-b).

Table 7.1 Magnetoresistance in $\text{Fe}_3\text{GaTe}_2/\text{GaSe}/\text{Fe}_3\text{GaTe}_2$ MTJs with different GaSe thicknesses at $T = 10$ K and $T = 300$ K.

GaSe thickness	TMR	TMR
	($T = 10$ K, $V = +0.5$ V)	($T = 300$ K, $V = +0.5$ V)
7 nm	74%	18%
8 nm	90%	36%
10 nm	101%	27%

7.6 Summary

In summary, our results demonstrate that the vdW heterostructure $\text{Fe}_3\text{GaTe}_2/\text{WSe}_2/\text{Fe}_3\text{GaTe}_2$ provides an excellent platform for MTJs. It exhibits an ideal tunnelling behaviour with a TMR signal as large as 85 % at room temperature, corresponding to a spin polarization of 55 %. The large room-temperature magnetoresistance is comparable to that of state-of-the-art conventional MTJs and represents a significant advance due to the absence of room-temperature TMR in all-2D MTJs. We also observed room-temperature TMR in $\text{Fe}_3\text{GaTe}_2/\text{GaSe}/\text{Fe}_3\text{GaTe}_2$ MTJs. In this case, we revealed a characteristic dependence of the TMR on the applied voltage, which requires further investigation. By adjusting the thickness of the spacer layer, the TMR could be further increased. Also, we envisage that the use of tunnel barriers in Fe_3GaTe_2 -based MTJs, such as the vdW insulator hBN, larger TMRs could be achieved, offering opportunities for further advances and new possibilities for next-generation spintronic devices.

Chapter 8

Conclusions and outlook

This PhD focused on the investigation of charge- and spin-quanta in van der Waals (vdW) heterostructures, that combine nanolayers of graphene, GaSe, WSe₂, ferroelectric α -In₂Se₃ or ferromagnetic Fe₃GaTe₂. Devices based on these two-dimensional (2D) materials demonstrate great potential for future technologies, such as ultraviolet photodetectors, non-volatile memories and low-power electronics.

The sections below examine these findings and discuss future prospects for development.

8.1 Graphene/In₂Se₃/graphene ferroelectric semiconductor junctions

We demonstrated the potential of ferroelectric semiconductor junctions (FSJs) consisting of α -In₂Se₃ sandwiched between two single-layer graphene electrodes. The ferroelectric polarization of the α -In₂Se₃ layer can be manipulated by applying a voltage, resulting in the tuning of the Schottky barrier height at the graphene/ α -In₂Se₃ interface, and thus modulating the electron transmission across the junction, which causes memristive effects. These effects are robust processes over a wide range of temperatures (100 ~ 380 K). However, they can be influenced by the ionization of defects and impurities that reside in *n*-type α -In₂Se₃, a phenomenon that tends to weaken the memristive effect. The additional free carriers generated by impact ionization, tunnelling and thermionic injection can neutralize the polarization charges at the graphene/ α -In₂Se₃ interface and influence the hysteretic behaviour in the

electrical transport. Furthermore, light has been shown to effectively modify the electronic properties and memristive effects of these FSJs, with high photoresponsivity ($\sim 10^5$ A/W) and rapid photocurrent modulation (~ 1 ms) as a result of α -In₂Se₃'s suitable bandgap (1.4 eV) and its favourable interface with graphene. As FSJs with symmetrical two-terminal structures, graphene/In₂Se₃/graphene heterojunctions achieve robust memristive effects, like other α -In₂Se₃-based FSJs or ferroelectric field-effect transistors (FeFETs).^{97,109,112,113,169,270-273} Due to high storage density, low energy cost and short response time, vdW FSJs are promising for use in high-performance nanoelectronic devices. This work was published in *2D Materials* **8**, 045020 (2021).

8.2 Van der Waals interfaces for ultraviolet photodetection

We have examined the vdW interfaces in graphene/*p*-GaSe/*n*-In₂Se₃/graphene heterostructures for high-responsivity ultraviolet (UV) photodetectors. These junctions exhibit high photoresponsivity and low dark current under forward or reverse biases, or even without any externally applied bias. As a result, these multilayer vdW heterostructures could play a pivotal role in advancing high-performance 2D semiconductor-based devices for a wide array of applications. The operation of this type of *pn*-junction based differs qualitatively from that of a traditional semiconductor diode, as also observed in other thin vdW junctions in the literature.^{26,63,202,215,274-277} The type-II band alignment at the GaSe/In₂Se₃ interface and the built-in potential at the three vdW interfaces (*e.g.*, graphene/GaSe, GaSe/In₂Se₃,

and In₂Se₃/graphene interfaces) help to reduce carrier recombination, resulting in enhanced photoresponsivity (up to 10² A/W) and detectivity (up to 10¹³ Jones), surpassing conventional UV-enhanced silicon detection technology.^{197,216,217} Scanning photocurrent microscopy reveals that the contributions of the three vdW interfaces to overall responsivity can vary between devices due to layer non-uniformity and coupling. For instance, defects in GaSe can act as recombination centres, leading to a voltage-modulated photoluminescence emission. These results were published in *npj 2D Materials and Applications* **6**, 61 (2022).

8.3 Room-temperature magnetoresistance in magnetic tunnel junctions

We demonstrated a large tunnel magnetoresistance (TMR) at room temperature ($T = 300$ K) in vdW magnetic tunnel junctions (MTJs) based on a thin (< 10 nm) semiconductor spacer WSe₂ layer embedded between two Fe₃GaTe₂ electrodes with intrinsic above-room-temperature ferromagnetism. This Fe₃GaTe₂/WSe₂/Fe₃GaTe₂ heterostructure is an excellent platform for MTJs, which are the core component of in-memory technologies, such as magnetic random-access memory, magnetic sensors and programmable logic devices. The MTJ exhibits an ideal tunnelling behaviour with a TMR signal as large as 85 % at room temperature, corresponding to a spin polarization of 55 %. The large room-temperature magnetoresistance is comparable to that of state-of-the-art conventional MTJs and represents a significant advance due to the absence of room-temperature TMR in all-2D MTJs.^{234,248,249,261,278} The TMR

decreases as the temperature increases, disappearing above the Curie temperature of Fe_3GaTe_2 (~ 400 K), while the temperature-dependent spin polarization can be fitted well by a power law given by $P = P_0(1-T/T_C)^\gamma$. We also observed room-temperature TMR in $\text{Fe}_3\text{GaTe}_2/\text{GaSe}/\text{Fe}_3\text{GaTe}_2$ MTJs, which provides the conditions for further study of the magneto-tunnelling transport mechanisms. These results were published in *Chinese Physics Letters* **39**, 128501 (2022).

8.4 Outlook

Throughout this PhD project, novel discoveries have emerged, as well as new questions have been raised. These have sparked ideas and possibilities for further exploration, and triggered thinking about the development of 2D materials, which are detailed in this section.

To advance the field of FSJs, continued research into device design, mechanisms, and fabrication is essential for achieving reliable, optimized, and predictable memristive behaviours in graphene-based vdW heterostructures with ferroelectric tunnelling barriers. Literature demonstrates that a higher on/off ratio can be achieved by introducing an asymmetry in the FSJ structure.²⁷¹ Preparing thinner ferroelectric material interlayers also contributes to achieving higher tunnelling electroresistance (TER) in these devices, although there are still doubts about whether materials can maintain their ferroelectric properties at extremely thin thicknesses.^{15,89,279,280} Additionally, the development of ferroelectric semiconductors with controlled n - and p -type doping is critical for the integration of ferroelectric

materials into multi-functional devices in the future.

For the investigation of vdW photodetectors, optimizing their fabrication to minimize the impact of crystal defects can improve these devices.²²⁶ Further optimization of layer thickness, doping, and scalable growth could yield designs with even higher responsivity and detectivity, providing an alternative to traditional UV detection technologies. Fabricating sharper and polymer-free vdW interfaces can overcome slow photoresponse dynamics by reducing interlayer charge trap density, which is a technical challenge rather than an intrinsic limitation.²⁷⁴ Another possible technological advancement would involve incorporating vdW photodetectors into conventional complementary metal-oxide-semiconductor (CMOS) imaging systems. Potential areas of application could include imaging sensors or integrated optoelectronic circuits.^{185,274,281}

VdW magnetic tunnel junctions also require further investigation. By adjusting the thickness of the spacer layer, the TMR could be further increased. Also, we envisage that the use of tunnel barriers in Fe₃GaTe₂-based MTJs, such as the vdW insulator hBN, larger TMRs could be achieved, offering opportunities for further advances and new possibilities for next-generation spintronic devices. More significantly, by combining ferroelectrics and ferromagnets layered materials, multiferroic tunnel junctions (MFTJs) have the potential ability to control magnetism via an electric field and vice versa. Using first-principles simulations, literature has proposed artificial 2D multiferroics via a vdW heterostructure formed by ferroelectric/ferromagnet/ferroelectric, for multifunctional nanoelectronics.^{280,282-285}

However, the experimental realization of MFTJs remains a challenge due to the influence of the depolarization field and poor interface quality.

Generally, 2D materials offer unique opportunities for a wide range of vdW heterostructures without the constraint of lattice matching, which helps to explore novel optical, electrical, and magnetic devices. However, current research on devices based on 2D vdW materials is still at the laboratory stage. To promote their development towards the industrial field for programmable logic devices or in-memory computing in the post-Moore era, practical difficulties need to be overcome:

1. Develop feasible processes for large-scale fabrication of vdW devices, including wafer-scale growth technologies for mass production and processes for the batch assembly of vdW heterostructure devices. Through chemical vapour deposition (CVD), molecular beam epitaxy (MBE) and other methods, wafer-scale growth of vdW materials has been widely achieved, while the assembly process still usually uses dry transfer technology, which is only suitable for laboratory situations with low device quantity requirements.

2. Improve the stability of vdW devices. Exfoliation-made electronic and optoelectronic devices based on vdW materials usually have poor stability, with device parameters and performance easily changing over time, which is extremely unfavourable for practical applications. Among potential vdW integrated circuits, strict control of the production process is required to ensure that each vdW transistor meets the electrical requirements.

Although there are still many difficulties to be solved on the road to the application of vdW materials, they are an indispensable choice for studying novel physical effects. Since the advent of 2D materials, people's understanding of low-dimensional physics has been greatly expanded. 2D vdW materials are excellent platforms for observing various quantum phenomena, such as quantum Hall effects in graphene/InSe heterostructures and Mott transitions in semiconductor moiré superlattices.^{286,287} As the study deepens, more interesting physical phenomena and novel research areas will undoubtedly be discovered and explored.

Bibliography

- 1 Moore, G. E. Lithography and the future of Moore's Law. *IEEE J. Solid-State Circuits* **11**, 37-42 (2006).
- 2 Khan, H. N., Hounshell, D. A. & Fuchs, E. R. H. Science and research policy at the end of Moore's law. *Nat. Electron.* **1**, 14-21 (2018).
- 3 Novoselov, K. S. *et al.* A roadmap for graphene. *Nature* **490**, 192-200 (2012).
- 4 Novoselov, K. S. *et al.* Electric Field Effect in Atomically Thin Carbon Films. *Science* **306**, 666-669 (2004).
- 5 Zhang, Y., Tan, Y. W., Stormer, H. L. & Kim, P. Experimental observation of the quantum Hall effect and Berry's phase in graphene. *Nature* **438**, 201-204 (2005).
- 6 Geim, A. K. Graphene: Status and Prospects. *Science* **324**, 1530-1534 (2009).
- 7 Castro Neto, A. H., Guinea, F., Peres, N. M. R., Novoselov, K. S. & Geim, A. K. The electronic properties of graphene. *Rev. Mod. Phys.* **81**, 109-162 (2009).
- 8 Xu, X., Gabor, N. M., Alden, J. S., van der Zande, A. M. & McEuen, P. L. Photo-thermoelectric effect at a graphene interface junction. *Nano Lett.* **10**, 562-566 (2010).
- 9 Geim, A. K. & Novoselov, K. S. The rise of graphene. *Nat. Mater.* **6**, 183-191 (2007).
- 10 Geim, A. K. & Grigorieva, I. V. Van der Waals heterostructures. *Nature* **499**, 419-425 (2013).

- 11 Burch, K. S., Mandrus, D. & Park, J. G. Magnetism in two-dimensional van der Waals materials. *Nature* **563**, 47-52 (2018).
- 12 Wang, C., You, L., Cobden, D. & Wang, J. Towards two-dimensional van der Waals ferroelectrics. *Nat. Mater.* **22**, 542-552 (2023).
- 13 Tang, W. *et al.* A van der Waals Ferroelectric Tunnel Junction for Ultrahigh-Temperature Operation Memory. *Small Methods* **6**, 2101583 (2022).
- 14 Liu, Z. *et al.* In-plane ferroelectric tunnel junctions based on 2D α -In₂Se₃/semiconductor heterostructures. *npj Comput. Mater.* **9**, 6 (2023).
- 15 Wu, J. *et al.* High tunnelling electroresistance in a ferroelectric van der Waals heterojunction via giant barrier height modulation. *Nat. Electron.* **3**, 466-472 (2020).
- 16 Wang, X. *et al.* Van der Waals negative capacitance transistors. *Nat. Commun.* **10**, 3037 (2019).
- 17 Wang, X. *et al.* Van der Waals engineering of ferroelectric heterostructures for long-retention memory. *Nat. Commun.* **12**, 1109 (2021).
- 18 Deng, Y. *et al.* Gate-tunable room-temperature ferromagnetism in two-dimensional Fe₃GeTe₂. *Nature* **563**, 94-99 (2018).
- 19 Chen, X. *et al.* Octupole-driven magnetoresistance in an antiferromagnetic tunnel junction. *Nature* **613**, 490-495 (2023).
- 20 Da Browski, M. *et al.* All-optical control of spin in a 2D van der Waals magnet. *Nat. Commun.* **13**, 5976 (2022).

- 21 Tang, M. *et al.* Continuous manipulation of magnetic anisotropy in a van der Waals ferromagnet via electrical gating. *Nat. Electron.* **6**, 28-36 (2022).
- 22 Bertolazzi, S. *et al.* Nonvolatile Memories Based on Graphene and Related 2D Materials. *Adv. Mater.* **31**, 1806663 (2019).
- 23 Zheng, Z. *et al.* Unconventional ferroelectricity in moire heterostructures. *Nature* **588**, 71-76 (2020).
- 24 Andrei, E. Y. & MacDonald, A. H. Graphene bilayers with a twist. *Nat. Mater.* **19**, 1265-1275 (2020).
- 25 Freitag, M., Chiu, H. Y., Steiner, M., Perebeinos, V. & Avouris, P. Thermal infrared emission from biased graphene. *Nat. Nanotechnol.* **5**, 497-501 (2010).
- 26 Lv, Q., Yan, F., Wei, X. & Wang, K. High-Performance, Self-Driven Photodetector Based on Graphene Sandwiched GaSe/WS₂ Heterojunction. *Adv. Opt. Mater.* **6**, 1700490 (2018).
- 27 Zhu, W. *et al.* Broadband polarized photodetector based on p-BP/n-ReS₂ heterojunction. *J. Semicond.* **40**, 092001 (2019).
- 28 Lv, Q. *et al.* Interlayer Band-to-Band Tunneling and Negative Differential Resistance in van der Waals BP/InSe Field-Effect Transistors. *Adv. Funct. Mater.* **30**, 1910713 (2020).
- 29 Song, T. *et al.* Giant tunneling magnetoresistance in spin-filter van der Waals heterostructures. *Science* **360**, 1214-1218 (2018).
- 30 Cao, Y. *et al.* Correlated insulator behaviour at half-filling in magic-angle graphene superlattices. *Nature* **556**, 80-84 (2018).

- 31 Cao, Y. *et al.* Unconventional superconductivity in magic-angle graphene superlattices. *Nature* **556**, 43-50 (2018).
- 32 Nimbalkar, A. & Kim, H. Opportunities and Challenges in Twisted Bilayer Graphene: A Review. *Nano-Micro Lett.* **12**, 126 (2020).
- 33 Roy, S. *et al.* Structure, Properties and Applications of Two-Dimensional Hexagonal Boron Nitride. *Adv. Mater.* **33**, 2101589 (2021).
- 34 Xue, J. *et al.* Scanning tunnelling microscopy and spectroscopy of ultra-flat graphene on hexagonal boron nitride. *Nat. Mater.* **10**, 282-285 (2011).
- 35 Lee, J. S. *et al.* Wafer-scale single-crystal hexagonal boron nitride film via self-collimated grain formation. *Science* **362**, 817-821 (2018).
- 36 Wu, L. *et al.* Atomically sharp interface enabled ultrahigh-speed non-volatile memory devices. *Nat. Nanotechnol.* **16**, 882-887 (2021).
- 37 Mishchenko, A. *et al.* Twist-controlled resonant tunnelling in graphene/boron nitride/graphene heterostructures. *Nat. Nanotechnol.* **9**, 808-813 (2014).
- 38 Raj, V. *et al.* Passivation of InP solar cells using large area hexagonal-BN layers. *npj 2D Mater. Appl.* **5**, 12 (2021).
- 39 Gorbachev, R. V. *et al.* Strong Coulomb drag and broken symmetry in double-layer graphene. *Nat. Phys.* **8**, 896-901 (2012).
- 40 Sajid, A., Ford, M. J. & Reimers, J. R. Single-photon emitters in hexagonal boron nitride: a review of progress. *Rep. Prog. Phys.* **83**, 044501 (2020).
- 41 Caldwell, J. D. *et al.* Photonics with hexagonal boron nitride. *Nat. Rev. Mater.* **4**, 552-567 (2019).

- 42 Monroy, E., Omnès, F. & Calle, F. Wide-bandgap semiconductor ultraviolet photodetectors. *Semicond. Sci. Technol.* **18**, R33-R51 (2003).
- 43 Salvato, M. *et al.* Time response in carbon nanotube/Si based photodetectors. *Sens. Actuators, A* **292**, 71-76 (2019).
- 44 Riordan, M., Hoddeson, L. & Herring, C. The invention of the transistor. *Rev. Mod. Phys.* **71**, S336-S345 (1999).
- 45 Chaves, A. *et al.* Bandgap engineering of two-dimensional semiconductor materials. *npj 2D Mater. Appl.* **4**, 29 (2020).
- 46 Balakrishnan, N. *et al.* Room Temperature Electroluminescence from Mechanically Formed van der Waals III-VI Homojunctions and Heterojunctions. *Adv. Opt. Mater.* **2**, 1064-1069 (2014).
- 47 Mudd, G. W. *et al.* High broad-band photoresponsivity of mechanically formed InSe-graphene van der Waals heterostructures. *Adv. Mater.* **27**, 3760-3766 (2015).
- 48 Kim, W. *et al.* Tunable Graphene-GaSe Dual Heterojunction Device. *Adv. Mater.* **28**, 1845-1852 (2016).
- 49 Yan, F. *et al.* Fast, multicolor photodetection with graphene-contacted p-GaSe/n-InSe van der Waals heterostructures. *Nanotechnology* **28**, 27LT01 (2017).
- 50 Kim, W. *et al.* Photoresponse of Graphene-Gated Graphene-GaSe Heterojunction Devices. *ACS Appl. Nano Mater.* **1**, 3895-3902 (2018).

- 51 Wang, Y. *et al.* p-GaSe/n-Ga₂O₃ van der Waals Heterostructure Photodetector at Solar-Blind Wavelengths with Ultrahigh Responsivity and Detectivity. *ACS Photonics* **8**, 2256-2264 (2021).
- 52 Liang, G. *et al.* High-Performance Phototransistors by Alumina Encapsulation of a 2D Semiconductor with Self-Aligned Contacts. *Adv. Electron. Mater.* **8**, 2100954 (2022).
- 53 Balakrishnan, N. *et al.* Epitaxial growth of γ -InSe and α , β , and γ -In₂Se₃ on ϵ -GaSe. *2D Mater.* **5**, 035026 (2018).
- 54 Kuhn, A., Chevy, A. & Chevalier, R. Crystal structure and interatomic distances in GaSe. *Phys. Status Solidi A* **31**, 469-475 (1975).
- 55 Hu, P., Wen, Z., Wang, L., Tan, P. & Xiao, K. Synthesis of Few-Layer GaSe Nanosheets for High Performance Photodetectors. *ACS Nano* **6**, 5988-5994 (2012).
- 56 Jacobs-Gedrim, R. B. *et al.* Extraordinary photoresponse in two-dimensional In₂Se₃ nanosheets. *ACS Nano* **8**, 514-521 (2014).
- 57 Island, J. O., Blanter, S. I., Buscema, M., van der Zant, H. S. & Castellanos-Gomez, A. Gate controlled photocurrent generation mechanisms in high-gain In₂Se₃ phototransistors. *Nano Lett.* **15**, 7853-7858 (2015).
- 58 Zultak, J. *et al.* Ultra-thin van der Waals crystals as semiconductor quantum wells. *Nat. Commun.* **11**, 125 (2020).
- 59 Shigetomi, S. & Ikari, T. Optical properties of GaSe grown with an excess and a lack of Ga atoms. *J. Appl. Phys.* **94**, 5399-5401 (2003).

- 60 Katerinchuk, V. N., Kovalyuk, Z. D., Netyaga, V. V. & Betsa, T. V. Heterojunctions Produced from the Layered Semiconductors SnS_{1.9}Se_{0.1} and GaSe<Cd>. *Inorg. Mater.* **37**, 336-338 (2001).
- 61 Sorifi, S., Moun, M., Kaushik, S. & Singh, R. High-Temperature Performance of a GaSe Nanosheet-Based Broadband Photodetector. *ACS Appl. Electron. Mater.* **2**, 670-676 (2020).
- 62 Rybkovskiy, D. V. *et al.* Size-induced effects in gallium selenide electronic structure: The influence of interlayer interactions. *Phys. Rev. B* **84**, 085314 (2011).
- 63 Cao, Y. *et al.* Strong enhancement of photoresponsivity with shrinking the electrodes spacing in few layer GaSe photodetectors. *Sci. Rep.* **5**, 8130 (2015).
- 64 Xie, S. *et al.* Van der Waals interfaces in multilayer junctions for ultraviolet photodetection. *npj 2D Mater. Appl.* **6**, 61 (2022).
- 65 Lines, M. E. & Glass, A. M. *Principles and applications of ferroelectrics and related materials.* (Oxford university press, 2001).
- 66 Garcia, V. *et al.* Giant tunnel electroresistance for non-destructive readout of ferroelectric states. *Nature* **460**, 81-84 (2009).
- 67 Kim, P. *et al.* High Energy Density Nanocomposites Based on Surface-Modified BaTiO₃ and a Ferroelectric Polymer. *ACS Nano* **3**, 2581-2592 (2009).

- 68 Kang, L. *et al.* Giant tunneling electroresistance in two-dimensional ferroelectric tunnel junctions with out-of-plane ferroelectric polarization. *Phys. Rev. B* **101**, 014105 (2020).
- 69 Sharma, P. *et al.* Nonvolatile ferroelectric domain wall memory. *Sci. Adv.* **3**, e1700512 (2017).
- 70 Scott, J. Applications of modern ferroelectrics. *Science* **315**, 954-959 (2007).
- 71 Ahn, C., Rabe, K. & Triscone, J.-M. Ferroelectricity at the nanoscale: local polarization in oxide thin films and heterostructures. *Science* **303**, 488-491 (2004).
- 72 A century of ferroelectricity. *Nat. Mater.* **19**, 129 (2020).
- 73 Valasek, J. Piezo-electric and allied phenomena in Rochelle salt. *Phys. Rev.* **17**, 475-471 (1921).
- 74 Zhou, T. *et al.* Improving Dielectric Properties of BaTiO₃/Ferroelectric Polymer Composites by Employing Surface Hydroxylated BaTiO₃ Nanoparticles. *ACS Appl. Mater. Interfaces* **3**, 2184-2188 (2011).
- 75 Eichel, R.-A. *et al.* Defect-Dipole Formation in Copper-Doped PbTiO₃ Ferroelectrics. *Phys. Rev. Lett.* **100**, 095504 (2008).
- 76 Setter, N. *et al.* Ferroelectric thin films: Review of materials, properties, and applications. *J. Appl. Phys.* **100**, 051606 (2006).
- 77 Pawley, G. S., Cochran, W., Cowley, R. A. & Dolling, G. Diatomic Ferroelectrics. *Phys. Rev. Lett.* **17**, 753-755 (1966).

- 78 Chang, K. *et al.* Discovery of robust in-plane ferroelectricity in atomic-thick SnTe. *Science* **353**, 274-278 (2016).
- 79 Liu, F. *et al.* Room-temperature ferroelectricity in CuInP₂S₆ ultrathin flakes. *Nat. Commun.* **7**, 12357 (2016).
- 80 Zhou, Y. *et al.* Out-of-Plane Piezoelectricity and Ferroelectricity in Layered α -In₂Se₃ Nanoflakes. *Nano Lett.* **17**, 5508-5513 (2017).
- 81 Li, W. *et al.* Large disparity between optical and fundamental band gaps in layered In₂Se₃. *Phys. Rev. B* **98**, 165134 (2018).
- 82 Fei, Z. *et al.* Ferroelectric switching of a two-dimensional metal. *Nature* **560**, 336-339 (2018).
- 83 Yang, Q., Wu, M. & Li, J. Origin of Two-Dimensional Vertical Ferroelectricity in WTe₂ Bilayer and Multilayer. *J. Phys. Chem.* **9**, 7160-7164 (2018).
- 84 Wan, Y. *et al.* Room-Temperature Ferroelectricity in 1T'-ReS₂ Multilayers. *Phys. Rev. Lett.* **128**, 067601 (2022).
- 85 Yuan, S. *et al.* Room-temperature ferroelectricity in MoTe₂ down to the atomic monolayer limit. *Nat. Commun.* **10**, 1775 (2019).
- 86 Barraza-Lopez, S., Fregoso, B. M., Villanova, J. W., Parkin, S. S. P. & Chang, K. Colloquium: Physical properties of group-IV monochalcogenide monolayers. *Rev. Mod. Phys.* **93**, 011001 (2021).

- 87 Park, C. B. *et al.* Observation of Spin-Induced Ferroelectricity in a Layered van der Waals Antiferromagnet CuCrP₂S₆. *Adv. Electron. Mater.* **8**, 2101072 (2022).
- 88 Liu, K., Lu, J., Picozzi, S., Bellaiche, L. & Xiang, H. Intrinsic Origin of Enhancement of Ferroelectricity in SnTe Ultrathin Films. *Phys. Rev. Lett.* **121**, 027601 (2018).
- 89 Ding, W. *et al.* Prediction of intrinsic two-dimensional ferroelectrics in In₂Se₃ and other III₂-VI₃ van der Waals materials. *Nat. Commun.* **8**, 14956 (2017).
- 90 Wang, X. *et al.* Interfacial ferroelectricity in rhombohedral-stacked bilayer transition metal dichalcogenides. *Nat. Nanotechnol.* **17**, 367-371 (2022).
- 91 Jindal, A. *et al.* Coupled ferroelectricity and superconductivity in bilayer T_d-MoTe₂. *Nature* **613**, 48-52 (2023).
- 92 Rogée, L. *et al.* Ferroelectricity in untwisted heterobilayers of transition metal dichalcogenides. *Science* **376**, 973-978 (2022).
- 93 Yasuda, K., Wang, X., Watanabe, K., Taniguchi, T. & Jarillo-Herrero, P. Stacking-engineered ferroelectricity in bilayer boron nitride. *Science* **372**, 1458-1462 (2021).
- 94 Vizner Stern, M. *et al.* Interfacial ferroelectricity by van der Waals sliding. *Science* **372**, 1462-1466 (2021).
- 95 Li, W. *et al.* Emergence of ferroelectricity in a nonferroelectric monolayer. *Nat. Commun.* **14**, 2757 (2023).

- 96 Zhang, J.-J. *et al.* Type-II Multiferroic Hf₂VC₂F₂ MXene Monolayer with High Transition Temperature. *J. Am. Chem. Soc.* **140**, 9768-9773 (2018).
- 97 Han, W. *et al.* Phase-controllable large-area two-dimensional In₂Se₃ and ferroelectric heterophase junction. *Nat. Nanotechnol.* **18**, 55-63 (2022).
- 98 Lin, M. *et al.* Controlled Growth of Atomically Thin In₂Se₃ Flakes by van der Waals Epitaxy. *J. Am. Chem. Soc.* **135**, 13274-13277 (2013).
- 99 Xue, F. *et al.* Gatetunable and multidirection-switchable memristive phenomena in a Van Der Waals ferroelectric. *Adv. Mater.* **31**, 1901300 (2019).
- 100 Eddrief, M., Julien, C., Balkanski, M. & Kambas, K. Optimization of growth conditions for In₂Se₃ films. *Mater. Lett.* **2**, 432-436 (1984).
- 101 Emziane, M., Marsillac, S. & Bernède, J. C. Preparation of highly oriented α -In₂Se₃ thin films by a simple technique. *Mater. Chem. Phys.* **62**, 84-87 (2000).
- 102 El-Shair, H. T. & Bekheet, A. E. Effect of heat treatment on the optical properties of In₂Se₃ thin films. *J. Phys. D: Appl. Phys.* **25**, 1122 (1992).
- 103 Debbichi, L., Eriksson, O. & Lebègue, S. Two-Dimensional Indium Selenides Compounds: An Ab Initio Study. *J. Phys. Chem.* **6**, 3098-3103 (2015).
- 104 Ji, H. *et al.* Crystal structure and elementary electronic properties of Bi-stabilized α -In₂Se₃. *Mater. Res. Bull.* **48**, 2517-2521 (2013).
- 105 Vaidyanathan, R., Stickney, J. L., Cox, S. M., Compton, S. P. & Happek, U. Formation of In₂Se₃ thin films and nanostructures using electrochemical atomic layer epitaxy. *J. Electroanal. Chem.* **559**, 55-61 (2003).

- 106 Quereda, J. *et al.* Strong Quantum Confinement Effect in the Optical Properties of Ultrathin α -In₂Se₃. *Adv. Opt. Mater.* **4**, 1939-1943 (2016).
- 107 Xue, F. *et al.* Room-temperature ferroelectricity in hexagonally layered α -In₂Se₃ nanoflakes down to the monolayer limit. *Adv. Funct. Mater.* **28**, 1803738 (2018).
- 108 Xiao, J. *et al.* Intrinsic two-dimensional ferroelectricity with dipole locking. *Phys. Rev. Lett.* **120**, 227601 (2018).
- 109 Si, M. *et al.* A ferroelectric semiconductor field-effect transistor. *Nat. Electron.* **2**, 580-586 (2019).
- 110 Li, J., Li, H., Niu, X. & Wang, Z. Low-Dimensional In₂Se₃ Compounds: From Material Preparations to Device Applications. *ACS Nano* **15**, 18683–18707 (2021).
- 111 Wu, G. *et al.* Visible to short wavelength infrared In₂Se₃-nanoflake photodetector gated by a ferroelectric polymer. *Nanotechnology* **27**, 364002 (2016).
- 112 Poh, S. M. *et al.* Molecular-beam epitaxy of two-dimensional In₂Se₃ and its giant electroresistance switching in ferroresistive memory junction. *Nano Lett.* **18**, 6340-6346 (2018).
- 113 Wan, S. *et al.* Room-temperature ferroelectricity and a switchable diode effect in two-dimensional α -In₂Se₃ thin layers. *Nanoscale* **10**, 14885-14892 (2018).

- 114 Hou, P. *et al.* Resistive switching behavior in α -In₂Se₃ nanoflakes modulated by ferroelectric polarization and interface defects. *RSC Adv.* **9**, 30565-30569 (2019).
- 115 Li, W. *et al.* Synchronous enhancement for responsivity and response speed in In₂Se₃ photodetector modulated by piezoresistive effect. *ACS Appl. Mater. Interfaces* **11**, 47098-47105 (2019).
- 116 Wan, S. *et al.* Nonvolatile Ferroelectric Memory Effect in Ultrathin α -In₂Se₃. *Adv. Funct. Mater.* **29**, 1808606 (2019).
- 117 Liu, B. *et al.* Photodetector based on heterostructure of two-dimensional WSe₂/In₂Se₃. *Nanotechnology* **31**, 065203 (2020).
- 118 Shi, H. *et al.* Ultrafast Electrochemical Synthesis of Defect-Free In₂Se₃ Flakes for Large-Area Optoelectronics. *Adv. Mater.* **32**, 1907244 (2020).
- 119 Wang, L. *et al.* Exploring ferroelectric switching in α -In₂Se₃ for neuromorphic computing. *Adv. Funct. Mater.* **30**, 2004609 (2020).
- 120 Xue, F. *et al.* Optoelectronic Ferroelectric Domain-Wall Memories Made from a Single Van Der Waals Ferroelectric. *Adv. Funct. Mater.* **30**, 2004206 (2020).
- 121 Zhang, Y. *et al.* Analog and Digital Mode α -In₂Se₃ Memristive Devices for Neuromorphic and Memory Applications. *Adv. Electron. Mater.* **7**, 2100609 (2021).
- 122 Yang, J. *et al.* Ultrasensitive Ferroelectric Semiconductor Phototransistors for Photon-Level Detection. *Adv. Funct. Mater.* **32**, 2205468 (2022).

- 123 Han, E. *et al.* Bend-Induced Ferroelectric Domain Walls in alpha-In₂Se₃. *ACS Nano* **17**, 7881-7888 (2023).
- 124 Xie, S. *et al.* Ferroelectric semiconductor junctions based on graphene/In₂Se₃/graphene van der Waals heterostructures. *2D Mater.* **8**, 045020 (2021).
- 125 Du Trémolet de Lacheisserie, É., Gignoux, D. & Schlenker, M. (Springer New York, 2005).
- 126 Jiles, D. *Introduction to magnetism and magnetic materials*. (CRC press, 2015).
- 127 Julliere, M. Tunneling between ferromagnetic films. *Phys. Lett. A* **54**, 225-226 (1975).
- 128 Chappert, C., Fert, A. & Van Dau, F. N. The emergence of spin electronics in data storage. *Nat. Mater.* **6**, 813-823 (2007).
- 129 Ikeda, S. *et al.* Tunnel magnetoresistance of 604% at 300K by suppression of Ta diffusion in CoFeB/MgO/CoFeB pseudo-spin-valves annealed at high temperature. *Appl. Phys. Lett.* **93**, 082508 (2008).
- 130 Zhang, G. *et al.* Above-room-temperature strong intrinsic ferromagnetism in 2D van der Waals Fe₃GaTe₂ with large perpendicular magnetic anisotropy. *Nat. Commun.* **13**, 5067 (2022).
- 131 Tedrow, P. M. & Meservey, R. Spin-Dependent Tunneling into Ferromagnetic Nickel. *Phys. Rev. Lett.* **26**, 192-195 (1971).

- 132 Meservey, R. & Tedrow, P. M. Spin polarization of tunneling electrons from films of Fe, Co, Ni, and Gd. *Solid State Commun.* **11**, 333-336 (1972).
- 133 Wei, H. X., Qin, Q. H., Ma, M., Sharif, R. & Han, X. F. 80% tunneling magnetoresistance at room temperature for thin Al–O barrier magnetic tunnel junction with CoFeB as free and reference layers. *J. Appl. Phys.* **101**, 09B501 (2007).
- 134 Onsager, L. Crystal Statistics. I. A Two-Dimensional Model with an Order-Disorder Transition. *Phys. Rev.* **65**, 117-149 (1944).
- 135 Brush, S. G. History of the Lenz-Ising Model. *Rev. Mod. Phys.* **39**, 883-893 (1967).
- 136 Slota, M. *et al.* Magnetic edge states and coherent manipulation of graphene nanoribbons. *Nature* **557**, 691-695 (2018).
- 137 Tucek, J. *et al.* Emerging chemical strategies for imprinting magnetism in graphene and related 2D materials for spintronic and biomedical applications. *Chem. Soc. Rev.* **47**, 3899-3990 (2018).
- 138 Huang, B. *et al.* Layer-dependent ferromagnetism in a van der Waals crystal down to the monolayer limit. *Nature* **546**, 270-273 (2017).
- 139 Gong, C. *et al.* Discovery of intrinsic ferromagnetism in two-dimensional van der Waals crystals. *Nature* **546**, 265-269 (2017).
- 140 Wang, Z. *et al.* Magnetization dependent tunneling conductance of ferromagnetic barriers. *Nat. Commun.* **12**, 6659 (2021).

- 141 Bedoya-Pinto, A. *et al.* Intrinsic 2D-XY ferromagnetism in a van der Waals monolayer. *Science* **374**, 616-620 (2021).
- 142 Liu, S. *et al.* Wafer-scale two-dimensional ferromagnetic Fe₃GeTe₂ thin films grown by molecular beam epitaxy. *npj 2D Mater. Appl.* **1**, 30 (2017).
- 143 May, A. F. *et al.* Ferromagnetism Near Room Temperature in the Cleavable van der Waals Crystal Fe₅GeTe₂. *ACS Nano* **13**, 4436-4442 (2019).
- 144 Zhang, H. *et al.* Cavity-enhanced linear dichroism in a van der Waals antiferromagnet. *Nat. Photonics* **16**, 311-317 (2022).
- 145 Deng, Y. *et al.* Quantum anomalous Hall effect in intrinsic magnetic topological insulator MnBi₂Te₄. *Science* **367**, 895-900 (2020).
- 146 Bonilla, M. *et al.* Strong room-temperature ferromagnetism in VSe₂ monolayers on van der Waals substrates. *Nat. Nanotechnol.* **13**, 289-293 (2018).
- 147 Huang, B. *et al.* Emergent phenomena and proximity effects in two-dimensional magnets and heterostructures. *Nat. Mater.* **19**, 1276-1289 (2020).
- 148 Yi, J. *et al.* Competing antiferromagnetism in a quasi-2D itinerant ferromagnet: Fe₃GeTe₂. *2D Mater.* **4**, 011005 (2016).
- 149 Kim, K. *et al.* Large anomalous Hall current induced by topological nodal lines in a ferromagnetic van der Waals semimetal. *Nat. Mater.* **17**, 794-799 (2018).

- 150 Fei, Z. *et al.* Two-dimensional itinerant ferromagnetism in atomically thin Fe_3GeTe_2 . *Nat. Mater.* **17**, 778-782 (2018).
- 151 Zhuang, H. L., Kent, P. R. C. & Hennig, R. G. Strong anisotropy and magnetostriction in the two-dimensional Stoner ferromagnet Fe_3GeTe_2 . *Phys. Rev. B* **93**, 134407 (2016).
- 152 May, A. F., Calder, S., Cantoni, C., Cao, H. & McGuire, M. A. Magnetic structure and phase stability of the van der Waals bonded ferromagnet $\text{Fe}_{3-x}\text{GeTe}_2$. *Phys. Rev. B* **93**, 014411 (2016).
- 153 Zhu, J.-X. *et al.* Electronic correlation and magnetism in the ferromagnetic metal Fe_3GeTe_2 . *Phys. Rev. B* **93**, 144404 (2016).
- 154 Wang, Y. *et al.* Anisotropic anomalous Hall effect in triangular itinerant ferromagnet Fe_3GeTe_2 . *Phys. Rev. B* **96**, 134428 (2017).
- 155 J Lopes, J. M. *et al.* Large-area van der Waals epitaxy and magnetic characterization of Fe_3GeTe_2 films on graphene. *2D Mater.* **8**, 041001 (2021).
- 156 Kim, D. *et al.* Antiferromagnetic coupling of van der Waals ferromagnetic Fe_3GeTe_2 . *Nanotechnology* **30**, 245701 (2019).
- 157 Zhu, W. *et al.* Large Room-Temperature Magnetoresistance in van der Waals Ferromagnet/Semiconductor Junctions. *Chin. Phys. Lett.* **39**, 128501 (2022).
- 158 del Barrio, J. & Sánchez-Somolinos, C. Light to Shape the Future: From Photolithography to 4D Printing. *Adv. Opt. Mater.* **7**, 1900598 (2019).
- 159 Pimpin, A. & Srituravanich, W. Review on micro-and nanolithography techniques and their applications. *Eng. J.* **16**, 37-56 (2012).

- 160 Zasloukin, A., Kovalyuk, Z. & Mintyanskii, I. Electrical properties of In_2Se_3 layered crystals doped with cadmium, iodine, or copper. *Inorg. Mater.* **43**, 1271-1274 (2007).
- 161 Castellanos-Gomez, A. *et al.* Deterministic transfer of two-dimensional materials by all-dry viscoelastic stamping. *2D Mater.* **1**, 011002 (2014).
- 162 Bie, Y.-Q. *et al.* Site-Specific Transfer-Printing of Individual Graphene Microscale Patterns to Arbitrary Surfaces. *Adv. Mater.* **23**, 3938-3943 (2011).
- 163 Mazumder, D. *Optoelectronic properties of the two-dimensional van der Waals semiconductor indium selenide (InSe)*, University of Nottingham (2022).
- 164 Güthner, P. & Dransfeld, K. Local poling of ferroelectric polymers by scanning force microscopy. *Appl. Phys. Lett.* **61**, 1137-1139 (1992).
- 165 Jesse, S., Baddorf, A. P. & Kalinin, S. V. Dynamic behaviour in piezoresponse force microscopy. *Nanotechnology* **17**, 1615 (2006).
- 166 Soergel, E. Piezoresponse force microscopy (PFM). *J. Phys. D: Appl. Phys.* **44**, 464003 (2011).
- 167 Kittel, C. *Introduction to solid state physics*. (John Wiley & sons, inc., 1976).
- 168 Patane, A. & Balkan, N. *Semiconductor Research: Experimental Techniques*. Vol. 150 (Springer Science & Business Media, 2012).
- 169 Liu, K. *et al.* An optoelectronic synapse based on $\alpha\text{-In}_2\text{Se}_3$ with controllable temporal dynamics for multimode and multiscale reservoir computing. *Nat. Electron.* **5**, 761–773 (2022).

- 170 Parker, J. & Gu, Y. Highly Efficient Polarization-Controlled Electrical Conductance Modulation in a van der Waals Ferroelectric/Semiconductor Heterostructure. *Adv. Electron. Mater.* **8**, 2200413 (2022).
- 171 Jin, J. *et al.* Multifunctional Dual Gated Coupling Device Using Van Der Waals Ferroelectric Heterostructure. *Adv. Electron. Mater.* **8**, 2200210 (2022).
- 172 Küpers, M. *et al.* Controlled crystal growth of indium selenide, In_2Se_3 , and the crystal structures of $\alpha\text{-In}_2\text{Se}_3$. *Inorg. Chem.* **57**, 11775-11781 (2018).
- 173 He, Q. *et al.* Epitaxial Growth of Large Area Two-Dimensional Ferroelectric $\alpha\text{-In}_2\text{Se}_3$. *Nano Lett.* **23**, 3098–3105 (2023).
- 174 Claro, M. S., Grzonka, J., Nicoara, N., Ferreira, P. J. & Sadewasser, S. Wafer-Scale Fabrication of 2D $\beta\text{-In}_2\text{Se}_3$ Photodetectors. *Adv. Opt. Mater.* **9**, 2001034 (2020).
- 175 Sze, S. M. *Semiconductor devices: physics and technology*. (John wiley & sons, 2008).
- 176 Grinberg, I. *et al.* Perovskite oxides for visible-light-absorbing ferroelectric and photovoltaic materials. *Nature* **503**, 509-512 (2013).
- 177 Lee, D. *et al.* Polarity control of carrier injection at ferroelectric/metal interfaces for electrically switchable diode and photovoltaic effects. *Phys. Rev. B* **84**, 125305 (2011).
- 178 Yuan, Y., Xiao, Z., Yang, B. & Huang, J. Arising applications of ferroelectric materials in photovoltaic devices. *J. Mater. Chem. A*. **2**, 6027-6041 (2014).

- 179 Xu, K. *et al.* Optical control of ferroelectric switching and multifunctional devices based on van der Waals ferroelectric semiconductors. *Nanoscale* **12**, 23488-23496 (2020).
- 180 Wang, J. *et al.* Selective Enhancement of Photoresponse with Ferroelectric-Controlled BP/In₂Se₃ vdW Heterojunction. *Adv. Sci.* **10**, 2205813 (2023).
- 181 Buscema, M. *et al.* Fast and broadband photoresponse of few-layer black phosphorus field-effect transistors. *Nano Lett.* **14**, 3347-3352 (2014).
- 182 Xiao, S., Chen, J.-H., Adam, S., Williams, E. D. & Fuhrer, M. S. Charged impurity scattering in bilayer graphene. *Phys. Rev. B* **82**, 041406 (2010).
- 183 Lee, Y. G. *et al.* Fast transient charging at the graphene/SiO₂ interface causing hysteretic device characteristics. *Appl. Phys. Lett.* **98**, 183508 (2011).
- 184 Zhang, L. *et al.* Direct Observation of Charge Injection of Graphene in the Graphene/WSe₂ Heterostructure by Optical-Pump Terahertz-Probe Spectroscopy. *ACS Appl. Mater. Interfaces* **11**, 47501-47506 (2019).
- 185 Xu, H. *et al.* High Responsivity and Gate Tunable Graphene-MoS₂ Hybrid Phototransistor. *Small* **10**, 2300-2306 (2014).
- 186 Liu, Y. *et al.* Planar carbon nanotube-graphene hybrid films for high-performance broadband photodetectors. *Nat. Commun.* **6**, 8589 (2015).
- 187 Liu, Q. *et al.* Fowler-Nordheim tunneling mechanism for performance improvement in graphene 2D/GaN 3D heterojunction ultraviolet photodetector. *Carbon* **201**, 1061-1067 (2023).

- 188 Hu, T. *et al.* High-Sensitivity and Fast-Speed UV Photodetectors Based on Asymmetric Nanoporous-GaN/Graphene Vertical Junction. *ACS Nano* **17**, 8411-8419 (2023).
- 189 Wan, X. *et al.* A self-powered high-performance graphene/silicon ultraviolet photodetector with ultra-shallow junction: breaking the limit of silicon? *npj 2D Mater. Appl.* **1**, 4 (2017).
- 190 Tran, H. *et al.* Si-Based GeSn Photodetectors toward Mid-Infrared Imaging Applications. *ACS Photonics* **6**, 2807-2815 (2019).
- 191 Razeghi, M. Short-wavelength solar-blind detectors-status, prospects, and markets. *Proc. IEEE* **90**, 1006-1014 (2002).
- 192 Li, Q. *et al.* Gas-mediated liquid metal printing toward large-scale 2D semiconductors and ultraviolet photodetector. *npj 2D Mater. Appl.* **5**, 36 (2021).
- 193 Lin, C.-H. *et al.* A flexible solar-blind 2D boron nitride nanopaper-based photodetector with high thermal resistance. *npj 2D Mater. Appl.* **2**, 23 (2018).
- 194 Xie, C. *et al.* Recent Progress in Solar-Blind Deep-Ultraviolet Photodetectors Based on Inorganic Ultrawide Bandgap Semiconductors. *Adv. Funct. Mater.* **29**, 1806006 (2019).
- 195 Long, M., Wang, P., Fang, H. & Hu, W. Progress, Challenges, and Opportunities for 2D Material Based Photodetectors. *Adv. Funct. Mater.* **29**, 1803807 (2019).

- 196 George, A. *et al.* Giant persistent photoconductivity in monolayer MoS₂ field-effect transistors. *npj 2D Mater. Appl.* **5**, 15 (2021).
- 197 Wang, X., Cheng, Z., Xu, K., Tsang, H. K. & Xu, J.-B. High-responsivity graphene/silicon-heterostructure waveguide photodetectors. *Nat. Photonics* **7**, 888-891 (2013).
- 198 Jariwala, D. *et al.* Near-Unity Absorption in van der Waals Semiconductors for Ultrathin Optoelectronics. *Nano Lett.* **16**, 5482-5487 (2016).
- 199 Wong, J. *et al.* High Photovoltaic Quantum Efficiency in Ultrathin van der Waals Heterostructures. *ACS Nano* **11**, 7230-7240 (2017).
- 200 Wu, F. *et al.* High efficiency and fast van der Waals hetero-photodiodes with a unilateral depletion region. *Nat. Commun.* **10**, 4663 (2019).
- 201 Novoselov, K. S., Mishchenko, A., Carvalho, A. & Castro Neto, A. H. 2D materials and van der Waals heterostructures. *Science* **353**, aac9439 (2016).
- 202 Fang, H. & Hu, W. Photogating in Low Dimensional Photodetectors. *Adv. Sci.* **4**, 1700323 (2017).
- 203 Yan, F., Hu, C., Wang, Z., Lin, H. & Wang, K. Perspectives on photodetectors based on selenides and their van der Waals heterojunctions. *Appl. Phys. Lett.* **118**, 190501 (2021).
- 204 Chen, Y. *et al.* Unipolar barrier photodetectors based on van der Waals heterostructures. *Nat. Electron.* **4**, 357-363 (2021).
- 205 Song, Q. *et al.* Moiré Perovskite Photodetector toward High-Sensitive Digital Polarization Imaging. *Adv. Energy Mater.* **11**, 2100742 (2021).

- 206 Chu, J. *et al.* High-Performance Ultraviolet Photodetector Based on a Few-Layered 2D NiPS₃ Nanosheet. *Adv. Funct. Mater.* **27**, 1701342 (2017).
- 207 Wang, F. *et al.* 2D library beyond graphene and transition metal dichalcogenides: a focus on photodetection. *Chem. Soc. Rev.* **47**, 6296-6341 (2018).
- 208 Zou, J. *et al.* Broadband Visible–Near Infrared Two-Dimensional WSe₂/In₂Se₃ Photodetector for Underwater Optical Communications. *Adv. Opt. Mater.* **10**, 2200143 (2022).
- 209 Ning, J. *et al.* Self-driven photodetector based on a GaSe/MoSe₂ selenide van der Waals heterojunction with the hybrid contact. *Appl. Phys. Lett.* **117**, 163104 (2020).
- 210 Jariwala, D. *et al.* Gate-tunable carbon nanotube-MoS₂ heterojunction p-n diode. *Proc. Natl. Acad. Sci. U.S.A.* **110**, 18076-18080 (2013).
- 211 Jariwala, D. *et al.* Hybrid, Gate-Tunable, van der Waals p-n Heterojunctions from Pentacene and MoS₂. *Nano Lett.* **16**, 497-503 (2016).
- 212 Lee, C. H. *et al.* Atomically thin p-n junctions with van der Waals heterointerfaces. *Nat. Nanotechnol.* **9**, 676-681 (2014).
- 213 Jaegermann, W., Klein, A. & Pettenkofer, C. in *Electron Spectroscopies Applied to Low-Dimensional Materials* 317-402 (Springer, 2002).
- 214 Drapak, S., Kovalyuk, Z., Netyaga, V. & Orletskii, V. On the mechanisms of current transfer in n-In₂Se₃-p-GaSe heterostructures. *Tech. Phys. Lett* **28**, 707-710 (2002).

- 215 Kaushik, S. & Singh, R. 2D Layered Materials for Ultraviolet Photodetection: A Review. *Adv. Opt. Mater.* **9**, 2002214 (2021).
- 216 Nayfeh, O. M., Rao, S., Smith, A., Therrien, J. & Nayfeh, M. H. Thin Film Silicon Nanoparticle UV Photodetector. *IEEE Photon. Technol. Lett.* **16**, 1927-1929 (2004).
- 217 Khodami, I., Taghibakhsh, F. & Karim, K. S. UV-Enhanced a-Si:H Metal–Semiconductor–Metal Photodetector. *IEEE Electron Device Lett.* **29**, 1007-1010 (2008).
- 218 Lan, C. *et al.* Zener Tunneling and Photoresponse of a WS₂/Si van der Waals Heterojunction. *ACS Appl. Mater. Interfaces* **8**, 18375-18382 (2016).
- 219 Xu, Z. *et al.* Monolayer MoS₂/GaAs heterostructure self-driven photodetector with extremely high detectivity. *Nano Energy* **23**, 89-96 (2016).
- 220 Ma, H. *et al.* Ultrasensitive and Broad-Spectrum Photodetectors Based on InSe/ReS₂ Heterostructure. *Adv. Opt. Mater.* **10**, 2101772 (2021).
- 221 Madelung, O. *Semiconductors: data handbook*. (Springer Science & Business Media, 2004).
- 222 Zhao, H. *et al.* Conjoined photo-thermoelectric effect in ZnO-graphene nanocomposite foam for self-powered simultaneous temperature and light sensing. *Sci. Rep.* **10**, 11864 (2020).
- 223 Errandonea, D., Segura, A., Muñoz, V. & Chevy, A. Effects of pressure and temperature on the dielectric constant of GaS, GaSe, and InSe: Role of the electronic contribution. *Phys. Rev. B* **60**, 15866-15874 (1999).

- 224 Wu, D. *et al.* Thickness-Dependent Dielectric Constant of Few-Layer In₂Se₃ Nanoflakes. *Nano Lett.* **15**, 8136-8140 (2015).
- 225 Deak, P., Han, M., Lorke, M., Tabriz, M. F. & Frauenheim, T. Intrinsic defects of GaSe. *J. Condens. Matter Phys.* **32**, 285503 (2020).
- 226 Hopkinson, D. G. *et al.* Formation and Healing of Defects in Atomically Thin GaSe and InSe. *ACS Nano* **13**, 5112-5123 (2019).
- 227 Tonndorf, P. *et al.* Single-photon emitters in GaSe. *2D Mater.* **4**, 021010 (2017).
- 228 Rahaman, M., Rodriguez, R. D., Monecke, M., Lopez-Rivera, S. A. & Zahn, D. R. T. GaSe oxidation in air: from bulk to monolayers. *Semicond. Sci. Technol.* **32**, 105004 (2017).
- 229 Molas, M. R. *et al.* Raman spectroscopy of GaSe and InSe post-transition metal chalcogenides layers. *Faraday Discuss.* **227**, 163-170 (2021).
- 230 Osiekowicz, M. *et al.* Resonance and antiresonance in Raman scattering in GaSe and InSe crystals. *Sci. Rep.* **11**, 924 (2021).
- 231 Zhu, J.-G. & Park, C. Magnetic tunnel junctions. *Mater. Today* **9**, 36-45 (2006).
- 232 Maciel, N., Marques, E., Naviner, L., Zhou, Y. & Cai, H. Magnetic Tunnel Junction Applications. *Sensors* **20**, 121 (2020).
- 233 Yang, H. *et al.* Two-dimensional materials prospects for non-volatile spintronic memories. *Nature* **606**, 663-673 (2022).

- 234 Moodera, J. S., Kinder, L. R., Wong, T. M. & Meservey, R. Large magnetoresistance at room temperature in ferromagnetic thin film tunnel junctions. *Phys. Rev. Lett.* **74**, 3273-3276 (1995).
- 235 Wang, W.-G., Li, M., Hageman, S. & Chien, C. L. Electric-field-assisted switching in magnetic tunnel junctions. *Nat. Mater.* **11**, 64-68 (2011).
- 236 Wang, W. *et al.* Spin-Valve Effect in NiFe/MoS₂/NiFe Junctions. *Nano Lett.* **15**, 5261-5267 (2015).
- 237 Butler, W. H., Zhang, X. G., Schulthess, T. C. & MacLaren, J. M. Spin-dependent tunneling conductance of Fe|MgO|Fe sandwiches. *Phys. Rev. B* **63**, 054416 (2001).
- 238 Yuasa, S., Nagahama, T., Fukushima, A., Suzuki, Y. & Ando, K. Giant room-temperature magnetoresistance in single-crystal Fe/MgO/Fe magnetic tunnel junctions. *Nat. Mater.* **3**, 868-871 (2004).
- 239 Kalitsov, A. *et al.* Bias dependence of tunneling magnetoresistance in magnetic tunnel junctions with asymmetric barriers. *J. Phys. Condens. Matter* **25**, 496005 (2013).
- 240 Dorneles, L. S., Sommer, R. L. & Schelp, L. F. Tunnel magnetoresistance in NiFe/TaO_x/Al₂O₃/Co junctions with a thin TaO_x layer. *J. Appl. Phys.* **91**, 7971-7973 (2002).
- 241 Huang, B. *et al.* Electrical control of 2D magnetism in bilayer CrI₃. *Nat. Nanotechnol.* **13**, 544-548 (2018).

- 242 Hu, C. *et al.* From two- to multi-state vertical spin valves without spacer layer based on Fe₃GeTe₂ van der Waals homo-junctions. *Sci. Bull.* **65**, 1072-1077 (2020).
- 243 Ye, X.-G. *et al.* Orbit-Transfer Torque Driven Field-Free Switching of Perpendicular Magnetization. *Chin. Phys. Lett.* **39**, 037303 (2022).
- 244 Feng, H. *et al.* Resistance anomaly and linear magnetoresistance in thin flakes of itinerant ferromagnet Fe₃GeTe₂. *Chin. Phys. Lett.* **39**, 077501 (2022).
- 245 Albarakati, S. *et al.* Antisymmetric magnetoresistance in van der Waals Fe₃GeTe₂/graphite/Fe₃GeTe₂ trilayer heterostructures. *Sci. Adv.* **5**, eaaw0409 (2019).
- 246 Alghamdi, M. *et al.* Highly Efficient Spin-Orbit Torque and Switching of Layered Ferromagnet Fe₃GeTe₂. *Nano Lett.* **19**, 4400-4405 (2019).
- 247 Ding, B. *et al.* Observation of Magnetic Skyrmion Bubbles in a van der Waals Ferromagnet Fe₃GeTe₂. *Nano Lett.* **20**, 868-873 (2019).
- 248 Lin, H. *et al.* Spin-Valve Effect in Fe₃GeTe₂/MoS₂/Fe₃GeTe₂ van der Waals Heterostructures. *ACS Appl. Mater. Interfaces* **12**, 43921-43926 (2020).
- 249 Zhu, W. *et al.* Large Tunneling Magnetoresistance in van der Waals Ferromagnet/Semiconductor Heterojunctions. *Adv. Mater.* **33**, 2104658 (2021).
- 250 Zheng, Y. *et al.* Spin filtering effect in all-van der Waals heterostructures with WSe₂ barriers. *npj 2D Mater. Appl.* **6**, 62 (2022).

- 251 Lin, H. *et al.* Current-assisted magnetization reversal in Fe₃GeTe₂ van der
Waals homojunctions. *Nanoscale* **14**, 2352-2358 (2022).
- 252 Kao, I. H. *et al.* Deterministic switching of a perpendicularly polarized magnet
using unconventional spin-orbit torques in WTe₂. *Nat. Mater.* **21**, 1029-1034
(2022).
- 253 Li, Z. *et al.* Magnetic Anisotropy Control with Curie Temperature above 400
K in a van der Waals Ferromagnet for Spintronic Device. *Adv. Mater.* **34**,
2201209 (2022).
- 254 Cao, Y. *et al.* Room-Temperature van der Waals Perpendicular Ferromagnet
Through Interlayer Magnetic Coupling. *Phys. Rev. Appl.* **17**, L051001 (2022).
- 255 Zhou, H., Zhang, Y. & Zhao, W. Tunable Tunneling Magnetoresistance in van
der Waals Magnetic Tunnel Junctions with 1T-CrTe₂ Electrodes. *ACS Appl.*
Mater. Interfaces **13**, 1214-1221 (2021).
- 256 Min, K.-H. *et al.* Tunable spin injection and detection across a van der Waals
interface. *Nat. Mater.* **21**, 1144–1149 (2022).
- 257 Gong, K. *et al.* Electric control of spin in monolayer WSe₂ field effect
transistors. *Nanotechnology* **25**, 435201 (2014).
- 258 Kumar, A. & Ahluwalia, P. K. Electronic structure of transition metal
dichalcogenides monolayers 1H-MX₂ (M = Mo, W; X = S, Se, Te) from
ab-initio theory: new direct band gap semiconductors. *Eur. Phys. J. B* **85**, 186
(2012).

- 259 Pudasaini, P. R. *et al.* High-performance multilayer WSe₂ field-effect transistors with carrier type control. *Nano Res.* **11**, 722-730 (2017).
- 260 Stolz, S. *et al.* Layer-dependent Schottky contact at van der Waals interfaces: V-doped WSe₂ on graphene. *npj 2D Mater. Appl.* **6**, 66 (2022).
- 261 Bowen, M. *et al.* Large magnetoresistance in Fe/MgO/FeCo(001) epitaxial tunnel junctions on GaAs(001). *Appl. Phys. Lett.* **79**, 1655-1657 (2001).
- 262 Shi, W. *et al.* Raman and photoluminescence spectra of two-dimensional nanocrystallites of monolayer WS₂ and WSe₂. *2D Mater.* **3**, 025016 (2016).
- 263 Wang, Z. *et al.* Tunneling Spin Valves Based on Fe₃GeTe₂/hBN/Fe₃GeTe₂ van der Waals Heterostructures. *Nano Lett.* **18**, 4303-4308 (2018).
- 264 Miyazaki, T. & Tezuka, N. Giant magnetic tunneling effect in Fe/Al₂O₃/Fe junction. *J. Magn. Magn. Mater.* **139**, L231-L234 (1995).
- 265 Tiusan, C. *et al.* Interfacial Resonance State Probed by Spin-Polarized Tunneling in Epitaxial Fe/MgO/Fe Tunnel Junctions. *Phys. Rev. Lett.* **93**, 106602 (2004).
- 266 Hu, C., Yan, F., Li, Y. & Wang, K. Vertical WS₂ spin valve with Ohmic property based on Fe₃GeTe₂ electrodes. *Chin. Phys. B* **30**, 097505 (2021).
- 267 Dho, J., Lee, E. K., Park, J. Y. & Hur, N. H. Effects of the grain boundary on the coercivity of barium ferrite BaFe₁₂O₁₉. *J. Magn. Magn. Mater.* **285**, 164-168 (2005).
- 268 Žutić, I., Fabian, J. & Das Sarma, S. Spintronics: Fundamentals and applications. *Rev. Mod. Phys.* **76**, 323-410 (2004).

- 269 Wang, X. *et al.* Ferromagnetism in 2D Vanadium Diselenide. *ACS Nano* **15**, 16236-16241 (2021).
- 270 Wang, S. *et al.* Two-dimensional ferroelectric channel transistors integrating ultra-fast memory and neural computing. *Nat. Commun.* **12**, 53 (2021).
- 271 Si, M. *et al.* Asymmetric Metal/ α -In₂Se₃/Si Crossbar Ferroelectric Semiconductor Junction. *ACS Nano* **15**, 5689-5695 (2021).
- 272 Zhang, D., Schoenherr, P., Sharma, P. & Seidel, J. Ferroelectric order in van der Waals layered materials. *Nat. Rev. Mater.* **8**, 25-40 (2022).
- 273 Liu, X. *et al.* Two-dimensional α -In₂Se₃-based ferroelectric semiconductor junction for reconfigurable photodetectors. *Appl. Phys. Lett.* **122**, 193101 (2023).
- 274 Lopez-Sanchez, O., Lembke, D., Kayci, M., Radenovic, A. & Kis, A. Ultrasensitive photodetectors based on monolayer MoS₂. *Nat. Nanotechnol.* **8**, 497-501 (2013).
- 275 Wei, X., Yan, F., Lv, Q., Shen, C. & Wang, K. Fast gate-tunable photodetection in the graphene sandwiched WSe₂/GaSe heterojunctions. *Nanoscale* **9**, 8388-8392 (2017).
- 276 Lu, J. *et al.* Graphene/In₂S₃ van der Waals Heterostructure for Ultrasensitive Photodetection. *ACS Photonics* **5**, 4912-4919 (2018).
- 277 Duan, J. *et al.* Self-Driven Broadband Photodetectors Based on MoSe₂/FePS₃ van der Waals n-p Type-II Heterostructures. *ACS Appl. Mater. Interfaces* **14**, 11927–11936 (2022).

- 278 De Teresa, J. M. *et al.* Inverse Tunnel Magnetoresistance in Co/SrTiO₃/La_{0.7}Sr_{0.3}MnO₃: New Ideas on Spin-Polarized Tunneling. *Phys. Rev. Lett.* **82**, 4288-4291 (1999).
- 279 Wen, Z., Li, C., Wu, D., Li, A. & Ming, N. Ferroelectric-field-effect-enhanced electroresistance in metal/ferroelectric/semiconductor tunnel junctions. *Nat. Mater.* **12**, 617-621 (2013).
- 280 Yan, Z., Li, Z., Han, Y., Qiao, Z. & Xu, X. Giant tunneling magnetoresistance and electroresistance in α -In₂Se₃-based van der Waals multiferroic tunnel junctions. *Phys. Rev. B* **105**, 075423 (2022).
- 281 Pi, L. *et al.* Broadband convolutional processing using band-alignment-tunable heterostructures. *Nat. Electron.* **5**, 248-254 (2022).
- 282 Lu, Y. *et al.* Artificial Multiferroics and Enhanced Magnetoelectric Effect in van der Waals Heterostructures. *ACS Appl. Mater. Interfaces* **12**, 6243-6249 (2020).
- 283 Su, Y. *et al.* Van der Waals Multiferroic Tunnel Junctions. *Nano Lett.* **21**, 175-181 (2021).
- 284 Wang, J., Chen, A., Li, P. & Zhang, S. Magnetoelectric Memory Based on Ferromagnetic/Ferroelectric Multiferroic Heterostructure. *Materials* **14**, 4623 (2021).
- 285 Zhu, Y., Cui, Q., Liang, J., Ga, Y. & Yang, H. Ferroelectricity controlled chiral spin textures and anomalous valley Hall effect in the Janus magnet-based multiferroic heterostructure. *2D Mater.* **9**, 045030 (2022).

- 286 Bhuiyan, M. A. *et al.* Photoquantum hall effect and light-induced charge transfer at the interface of graphene/InSe heterostructures. *Adv. Funct. Mater.* **29**, 1805491 (2019).
- 287 Li, T. *et al.* Continuous Mott transition in semiconductor moiré superlattices. *Nature* **597**, 350-354 (2021).